Master's thesis

NTNU
Norwegian University of Science and Technology

Eline Nybråten

# Factors Governing Pressure Behavior Under $CO_2$ Injection in a Faulted Basin-Scale Model

## A study of parameters and their relations when applying a pressure management approach to pressure compartments of the Smeaheia Storage Prospect

Master's thesis in Petroleum Geoscience and Engineering
Supervisor: Philip Ringrose
June 2022

NTNU
Kunnskap for en bedre verden

Eline Nybråten

# Factors Governing Pressure Behavior Under $CO_2$ Injection in a Faulted Basin-Scale Model

A study of parameters and their relations when applying a pressure management approach to pressure compartments of the Smeaheia Storage Prospect

Master's thesis in Petroleum Geoscience and Engineering
Supervisor: Philip Ringrose
June 2022

Norwegian University of Science and Technology

NTNU
Norwegian University of
Science and Technology

# Preface

This Thesis is written at the Department of Geoscience and Petroleum at the Norwegian University of Science and Technology (NTNU), spring 2022.

The project I have been working on is lead by the Center for Geophysical Forecasting (CGF). I would like to thank them for data, as well as great input and discussions a long the way. A special thanks to Andrea Callioli Santi, Tobias Dyngeland and Tian Guo.

A great thank you to my supervisor Philip Ringrose. I am truly grateful for your encouragement, exchange of knowledge and important questions. The field is dependent on motivated professionals like you.

Finally, I would like to thank my dear friends and parents for great support throughout the five years of my studies. Wouldn't have made it without you.

I hope my work can contribute to engagement and future development of an important topic.

Trondheim, 11.06.2022

Eline Nybråten

(intentionally left blank)

# Abstract

Large-scale deployment of carbon capture and storage will be an important effort to mitigate the concentration of greenhouse gases in the atmosphere. Geological formations offer great resources to $CO_2$ storage, where pressure management under injection is a key issue. A pressure management approach is put together by combining a simple box volume approach with a basin geo-pressure approach. The result is a complex equation of many unknown, uncertain parameters. The approach is applied to the Smeaheia storage prospect, a faulted region offshore the west coast of Norway. Review of fault seal analysis and fault interpretation in Petrel is carried out as to construct three contrasting scenarios of fault compartments in the prospect area. As the pressure management approach is applied to the compartments, several factors are found to influence the pressure behavior. Factors affecting the volumetric constraints from the box volume approach are found less important when injecting into the compartments, being compressibility, total pore volume, and pressure change. Factors directly affecting the compartment pressure through the injectivity equation of the basin geo-pressure approach are found more controlling, being initial pressure, maximum well pressure, the injectivity index, and the scaling parameter A. The parameter distributions and their relationships are contemplated uncertain, and an introductory application of unsupervised machine learning is meant to present opportunity of further developing a deeper analysis.

(intentionally left blank)

# Sammendrag

Fullskala $CO_2$-fangst og lagringsprosjekter vil kunne bidra som et effektivt klimatiltak ved å redusere konsentrasjonen av drivhusgasser i atmosfæren. Geologiske formasjoner med egnede lagringsbetingelser har enorme lagringspotensialer. En sentral utfordring er imidlertid regulering og kontroll av poretrykk. Trykkregulering under $CO_2$ injeksjon blir justert med en enkel volumbegrensning kombinert med en likning for injisert volum over tid. Sluttproduktet blir en komplisert trykkreguleringsmetode basert på et antall ukjente parametere. Metoden er videre anvendt på prospektet Smeaheia, et strukturelt forkastet område som er lokalisert utenfor vestkysten av Norge. Klassifisering og tolkning av forkastninger er utført i Petrel, hvor tre separate senarioer for forkastningsblokkene er satt sammen. Senarioene er evaluert ved hjelp av overnevnt metode, der trykket i forkastningsblokkene påvirkes av en rekke faktorer. Faktorene som påvirker volumbegrensningene viser seg å være mindre sentrale. Dette gjelder kompressibilitet, totalt porevolum og trykkendring. Faktorene som direkte påvirker injektivitetslikningen viser seg å være mer sentrale. Dette er faktorer som initialtrykk, maksimalt trykk, injektivitetsindeks og skaleringsparameteren A. Parameterfordelinger og forholdene mellom disse er ansett meget usikre. Derfor presenteres også en introduksjon av uovervåket maskinlæring utført på data fra trykkreguleringen på Smeaheia. Resultatene herfra vil gi en pekepinn til nødvendig videreutvikling og en mer avansert analyse.

# Table of Contents

# List of Figures

# 1 Introduction

## 1.1 Motivation & Study Objective

In February of 2022 the IPCC published the second part of the Sixth Assessment Report (IPCC, 2022), stating that climate change is already causing destruction to both humanity and nature, posing a threat to our livelihood. It was further stated that the effects of climate change on nature is more extensive and severe than expected, and that adaption is crucial as the window of opportunity for climate action is rapidly closing. Climate change and global warming are directly linked to the concentration of greenhouse gases in the atmosphere, and $CO_2$ has been identified as the main contributor (Cao et al., 2020).

Subsurface storage in the sedimentary basins offer one of the most promising solutions to effectively reduce the concentration of emitted $CO_2$ in the atmosphere, through large-scale $CO_2$ storage. As for large-scale $CO_2$ storage to be efficient, global deployment in both existing and emerging energy systems are needed (Ringrose & Meckel, 2019). Subsurface storage in geological formations is often associated with rift basins, where displacement geometry and bounding fault systems present many challenges for effectively utilizing the resources. Pressure management is a key issue, where many unknown and uncertain geological factors play in.

For this thesis a pressure management approach is put together and evaluated, aiming to approach the problem of basin pressure optimization under $CO_2$ injection. The faulted Smeaheia prospect region is used for the study, where the approach is applied. An assessment of a bounding fault system is carried out, where different pressure compartment scenarios are put together and evaluated.

This project is a team effort, where a team has been working on the same topic of pressure management at Smeaheia. This thesis will develop a more geophysical aspect with focus on choice and evaluation of geological parameters and variables when approaching pressure optimization of the basin-scale model. Compartment selection through fault seal analysis and interpretation in Petrel has been one of the main focuses to this work, with a further focus on evaluating parameters and distributions for these compartments.

The main objective of this thesis is selecting valid parameter distributions and understanding how they influence the pressure management approach that is evaluated.

# 2 $CO_2$ Storage - Theoretical background

## 2.1 Why CCS?

When assessing geological carbon dioxide ($CO_2$) storage in the subsurface, it is important to have a principal understanding of how the earths climate is hazardously effected by the increasing concentration of $CO_2$. Engaging in global efforts such as carbon capture and storage (CCS) is much needed to reduce the concentration of emitted $CO_2$ in the atmosphere.

Since pre-industrial times industrialization and urbanization has lead to increasing concentrations of greenhouse gases (GHG) in the atmosphere (Qader et al., 2021). The GHGs are known to trap in long-wave radiation from the sun, which increases the earth's average temperature. We know that rising average temperatures leads to an irreversible impact on climate (Mikhaylov et al., 2020), further having serious effects such as extreme weather, sea level rise, disrupted ecosystems, and now the threatening of human health (IPCC, 2022). It is known that the stability of the climate is directly linked to the proportion of GHGs in the atmosphere, and $CO_2$ has been identified as the main contributor to climate change and global warming (Cao et al., 2020).

$CO_2$ is the most abundant GHG, and the rising concentration is directly linked to the burning of fossil fuels (Qader et al., 2021). The concentration of $CO_2$ has reportedly risen to 48% above its pre-industrial level (European Comission, n.d.). Emissions will need to be significantly reduced; however, today fossil fuels cover more than 80% of the world's primary energy consumption (BP, 2020). With several sectors dependent on non-renewable energy sources in the years to come, as well as industries such as steel, chemical and cement emitting significant amounts of $CO_2$ (Miri et al., 2018), a transition period with significant sequestration will be needed.

Knowing the impact of $CO_2$ and GHG emissions, we see that global efforts such as CCS is much needed in the energy transition. It will contribute in reducing the human impact on climate change by mitigating the concentration of $CO_2$ in the atmosphere. Although CCS can be considered to be mature, it will require a rapid and significant up-scaling to meet the two-degree target scenario set in the Paris Agreement (Ringrose et al., 2021).

## 2.2 Technical Background

Carbon capture and storage can simply be described as capturing $CO_2$ from the atmosphere and storing it by sequestrating it long term. One can further distinguish between three main steps of this process, being the capturing, transport and storage of the $CO_2$ (Ringrose, 2020). In terms of CCS, this project will further assess the storage of $CO_2$.

There are numerous ways to sequestrate $CO_2$ from the atmosphere, such as storage in the ocean, soil, plants and geological structures . Today, storage in geological formations is the most promising option to ensure the large-scale, long-term storage that is crucially needed (Smit et al., 2014). Large accumulations of siliciclastic sediments are formed within rifted basins, and form important storage resources. Formations such as saline aquifers and depleted oil and gas fields can store significant amounts of $CO_2$ (Ringrose, 2020), and substantial technology and knowledge is already well-established through decades of both hydrocarbon production and $CO_2$-enhanced oil recovery (EOR). Supercritical $CO_2$ has already been transported long distances and injected into geological formations for around 45 years through EOR (Smit et al., 2014), although in much smaller amounts than what will have to be considered to affect the concentration of emitted $CO_2$ in the atmosphere.

Depleted oil and gas fields is considered one of the most practical options to store $CO_2$ (Z. Li et al., 2006). In addition to generally having optimal geological characteristics, the depletion ensures suitable pressure regimes in terms of low reservoir pressure. As a further matter, depleted oil and gas fields usually have been thoroughly characterized and have extensive data and equipment available, which can further be applied in a $CO_2$ storage project (Cooper, 2009).

However, it is much needed to find alternative geological formations to store $CO_2$ in addition to depleted oil and gas fields. According to the Global CCS Institute (n.d.) the deployment of carbon storage will progressively require utilization of deep saline aquifers, as these formations have a much larger capacity as well as a wider geographical distribution compared to e.g. depleted oil and gas fields.

A rather favourable aspect to subsurface $CO_2$ storage is its many geological similarities to hydrocarbon accumulation and production. As mentioned, much knowledge and experience from the hydrocarbon industry can be directly converted to $CO_2$ storage, where especially geological characteristics of hydrocarbon accumulation can be considered. Before looking further into these geological characteristics in Section 2.3, some basic concepts of subsurface $CO_2$ storage should be addressed.

When storing $CO_2$ in the subsurface one of the most fundamental concepts to consider is the storage depth. Depth is an important aspect to storage security (Ringrose, 2020), as well as the efficiency of the $CO_2$ storage. Both transport and storage of $CO_2$ is done in a super-critical fluid state (Ladislav et al., 2016). The super-critical state is a fluid phase where temperature and pressure is raised above it's critical values, and the distinction between the liquid and gas phase disappears (Sihvonen et al., 1999). One can consider this state as fluid having the density of a liquid and the viscosity of a gas. The super-critical phase of $CO_2$ enhance storage efficiency as the high density of the fluid leads to a higher mass stored per volume, as well as gaseous viscosity is ideal for e.g injection and the spreading of the $CO_2$ plume in the rock formation. The state of the fluid is dependent on pressure and temperature, and although factors such as the local geothermal gradient play in (Silver, 2021), one can say that the depth of the storage is of underlying importance. A widely accepted principal to follow is that storage cites are typically at a depth of 800m and deeper (Ringrose, 2020), conditioning pressure and temperatures resulting in a super-critical phase of the $CO_2$.

## 2.3 Geological Characteristics

Other basic aspects of subsurface $CO_2$ storage is capacity, injectivity and containment (Cooper, 2009). The capacity is frequently determined by the storage resource volume, which is directly dependent on the porosity of the formation rock. The injectivity refers to the rate at which the injection is happening, and this is further dependent on the permeability of the formation rock. Lastly, one should mention containment. This considers the ability of the storage complex to confine the injected $CO_2$, and is a very important aspect in terms of migration and leakage.

The optimal conditions and mechanisms associated with safe, effective $CO_2$ storage are well aligned with the geological characteristics that are known to have stored hydrocarbons underground for million of years. The Global CCS Institute (n.d.) highlights certain geological characteristics that are essential for safe, effective subsurface $CO_2$ storage:

- Sufficient rock pore volume in the geological formation, providing capacity to store the $CO_2$
- Sufficient rock permeability, allowing the injected $CO_2$ to spread in the formation.
- A seal. The reservoir needs a sealing cap rock, preventing the $CO_2$ from migrating from the storage formation.

The $CO_2$ is stored in the pore space of the reservoir rock, and naturally higher porosity condition higher storage capacity. Other factors such as density of the $CO_2$, structures and storage efficiencies also affect the capacity (Cooper, 2009).

As $CO_2$ is injected into a reservoir formation, the fluid is as mentioned in a super-critical phase. The density of the fluid is with this lower than of the typical formation fluid , and by considering physics and elementary laws we know that buoyancy will lead the $CO_2$ plume to migrate upwards (Smit et al., 2014). High rock permeability condition a better injectivity and flow of the $CO_2$ plume through the reservoir rock.

Another important aspect is the containment of the injected $CO_2$. A sealing cap rock will be essential to trap the fluid in the reservoir formation. This cap rock is typically relatively impermeable, e.g a shale, functioning as a barrier above the higher permeability reservoir. As the $CO_2$ plume spreads throughout the reservoir, trapping mechanisms are essential to contain the fluid in the reservoir rock, and are further discussed in Section 2.3.1.

A principle that differs the process of storing $CO_2$ in the subsurface from the experience we have with hydrocarbon industry is the project timescales. A typical $CO_2$ storage project ranges in the 100-year-timescale (Wu et al., 2021), which further play up the importance of containment and long term seal integrity.

### 2.3.1 Trapping Mechanisms

One can consider a series of trapping mechanisms that work both together and separately to contain the injected $CO_2$ in the reservoir rock (CCP, 2015), being:

- Structural and Stratigraphic trapping
- Residual trapping
- Solubility trapping
- Mineral trapping

During the initial phase of a project we mainly rely on structural and stratigraphic trapping (Smit et al., 2014), see Figure 2. These trapping mechanisms are the same as the structural and stratigraphic trapping we know from hydrocarbon accumulation (Kaszuba et al., 2003). Stratigraphic trapping

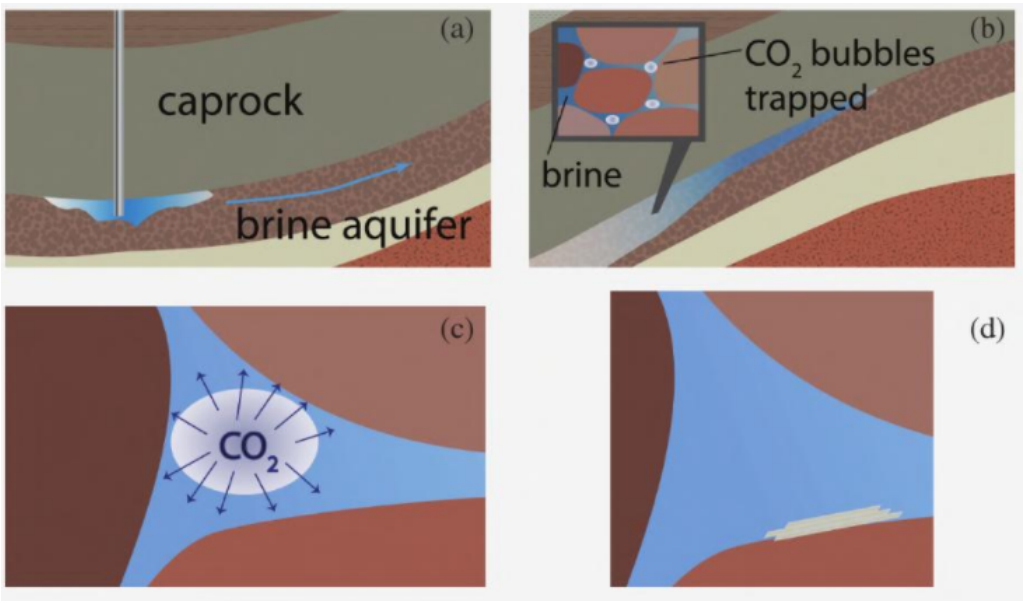


Figure 1: $CO_2$ Trapping Mechanisms. (a) Stratigraphic trapping - The injected $CO_2$ is trapped in the formation rock by the low permeability cap rock. (b) Residual trapping - Bubbles of $CO_2$ is trapped in the pore space of the formation rock as the aquifer brine imbibes it with capillary forces. (c) Solubility trapping - $CO_2$ is dissolved in the aquifer brine, where gravitational differences distributes the dissolved $CO_2$ throughout the formation. (d) Mineral trapping - Permanent storage occurs as the dissolved $CO_2$ produces protons and carbonic acid that in reaction with the formation brine and/or rock creates solids, such as carbonate minerals (e.g. Limestone).
From Smit et al. (2014)

consider changes in rock types, unconformities and variety in sedimentary features. Properties of reservoir rocks vary as they are affected by numerous spatial-varying factors (Aladejare & Wang, 2016), which can contribute to trapping and retention of injected $CO_2$. Structural trapping is trapping confined by geological structures such as anticlines and sealing faults. The sealing fault structures can create isolated pressure compartments. As the geological setting of Smeaheia is presented in Section 3 as well as the pressure optimization problem is addressed in Section 4 one can see that it is predominantly this structural trapping that is assessed and further evaluated for this study. However, it is essential to have an understanding of how the different trapping mechanisms work together to contain the injected $CO_2$ as well as increase the storage security. The structural and stratigraphic trapping mechanisms are the most dominant mechanisms for the initial part of the project timescale (CCP, 2015). The stratigraphic trapping can be considered the trapping of the fluid under the low permeability cap rock, as seen in Figure 1 (a). The injected $CO_2$ displaces the brine in the pore-space, creating a plume of injected $CO_2$. As the plume migrates upwards the sealing cap rock over the reservoir formation traps the $CO_2$ in the formation rock.

Residual trapping, also known as capillary trapping occurs as the injected $CO_2$ migrates upwards in the formation rock. Bubbles of $CO_2$ are trapped in the pore space of the rock as the brine imbibes it with capillary forces (Krevor et al., 2015), as seen in Figure 1 (b).

Solubility trapping, also known as dissolution trapping takes place as the $CO_2$ dissolves in the brine (Figure 1 (c)). The dissolution increases the density of the brine, leading to fingering as a result of gravitational instabilities in the formation (Soltanian et al., 2017). The fingering distributes the dissolved $CO_2$, storing it throughout the formation. This process is the most important geochemical reaction to $CO_2$ storage projects (Ringrose, 2020), as it assist stabilization of long term storage.

Mineral trapping, also known as mineralization occurs as solid minerals formed by protons and carbonic acid created by the dissolved $CO_2$ reacts with the brine and/or formation rock (Iglauer, 2011), as seen in Figure 1 (d). This trapping mechanism may take thousands of years, and it increasingly becomes very difficult for the $CO_2$ to escape. This trapping mechanism is also refereed to as permanent storage (Liu & Maroto-Valer, 2014).

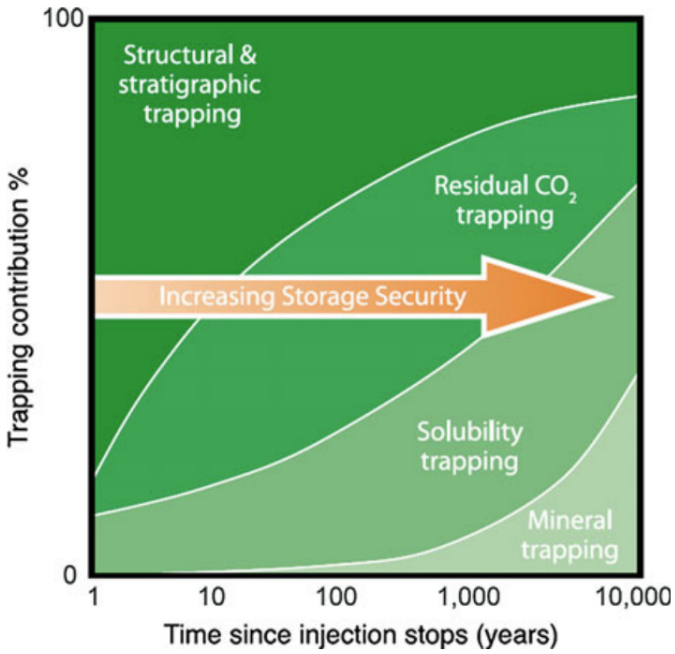


Figure 2: Trapping mechanism contribution as a function of time. In the initial phase structural and stratigraphic trapping is dominant, whereas mineral trapping may take thousands of years. However, the storage security increases with time as the trapping mechanisms work together. From Ringrose (2020)

As mentioned, the trapping mechanisms work together to contain the injected $CO_2$ in the reservoir rock. The mechanisms have their own timescales, e.g. the mineral trapping taking thousand of years (Smit et al., 2014), whereas the structural and stratigraphic trapping being dominant the first decades of a project. One can further consider a principle that the trapping mechanisms work together to increase the storage security as a function of time (Ringrose, 2020). Figure 2 shows this principle, where the trapping contribution of the different trapping mechanisms are presented as a function of time. As one can see, the total trapping contribution is highly dependent on the structural and stratigraphic trapping of the initial phase of the project. One can further establish that the more $CO_2$ is trapped through structural and stratigraphic trapping in the initial phase, the more residual, solubility, and mineral trapping can occur as a result.

As structural trapping through sealing fault structures is the focus of this study, fault structures and their sealing capacity will be further assessed.

## 2.4 Fault structures

Faults are planar fractures through a rock volume, with structures that together make up a fault zone (Silver, 2021). The fault zone comprises of 3 main architectural components, being the fault core, the damage zone, and protolith (Caine et al., 1996), as presented in Figure 3. Further, one can consider the fault core as the lithologic and structural part of the fault zone. This is the part of the fault zone where most the strain is accommodated (Silver, 2021), and often involve slip surfaces, brecciated zones, cataclasites, geochemically altered zones, and clay-rich gouge zones (Caine et al., 1996). The fault core is separated from the damage zone, which is a part of the rock unit that has experienced less deformation that the fault core, but still more deformed than the surrounding rock. In this zone one would typically find smaller faults, fractures, veins and folds (Silver, 2021). The protolith is the outer part of the rock unit, where there are no fault-related permeability structures. The fluid flow is here as of for the surrounding rock.

As mentioned, the fault zone often comprises gouge, cataclasite and other fault rocks. One typically

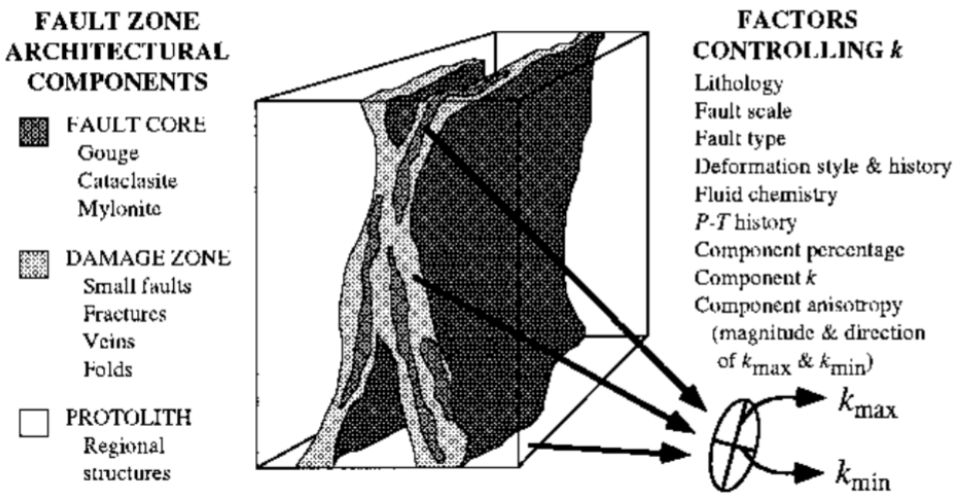


Figure 3: Architectural fault zone model showing the fault core, damage zone, and protolith. From Caine et al. (1996)

see upper levels of the crust producing cataclasis, involving brittle fragmentation and both dilatancy and sliding of the frictional grain boundaries (John, 2018). Gouge is the very fine-grained output of the faulting, where the grains are typically clay-sized. The gouge is a result of crushing and displacement of the reservoir sandstones, shale caprock, and other host rock material (Silver, 2021). This gouge may contain clay, and one often refer to clay-rich gouge. The fault gouge has a significant impact on fault properties such as permeability and capillary entry pressures (Yielding et al., 1997), and is therefore an interesting topic as fault seals are evaluated for $CO_2$ storage assessment and pressure management. Both the permeability and frictional strength of the fault gouge decreases with clay content (Kettermann et al., 2020).

## 2.5 Fault seals

Fault zones are a widespread occurrence, and fault sealing behavior is of high significance to many disciplines within geoscience (Pei et al., 2015). Moreover, the sealing of faults is of great importance when assessing $CO_2$ storage capacity and pressure predictions (Wu et al., 2021). One can further consider two types of fault seals, being membrane seals, such as the clay-rich gouge affecting the permeability as mentioned in Section 2.4, and fault juxtaposition seals (Pei et al., 2015). The two types of fault seals are displayed in Figure 4. A juxtaposition seal occurs as different stratigraphic intervals are juxtapositioned across the fault (Pei et al., 2015), such as the reservoir formation and a lower-permeability top seal unit in Figure 4. The second type of fault seal is the membrane seal, and considers the sealing capacity of the fault membrane. The dotted line displayed in Figure 4 shows how a membrane sealing fault potentially could trap fluid.

The fault seal capacity in siliciclastic rocks are mostly dependent on one factor, being the fault rock permeability. In cases without considerable amounts of cement, such as the Smeaheia faults, the permeability is primarily dependent on the amount of fine-grained material in the fault rock (Wu et al., 2021).

As mentioned, e.g. gouge with clay-sized grains may impact the permeability significantly. One can further assess fault seal capacity by considering the amount of fine-grained material in the fault rock. One should then consider two factors, being:

- Mechanical Damage
- Kinematic Mixing

Mechanical damage processes refer to the mechanical processes happening in relation the faulting,

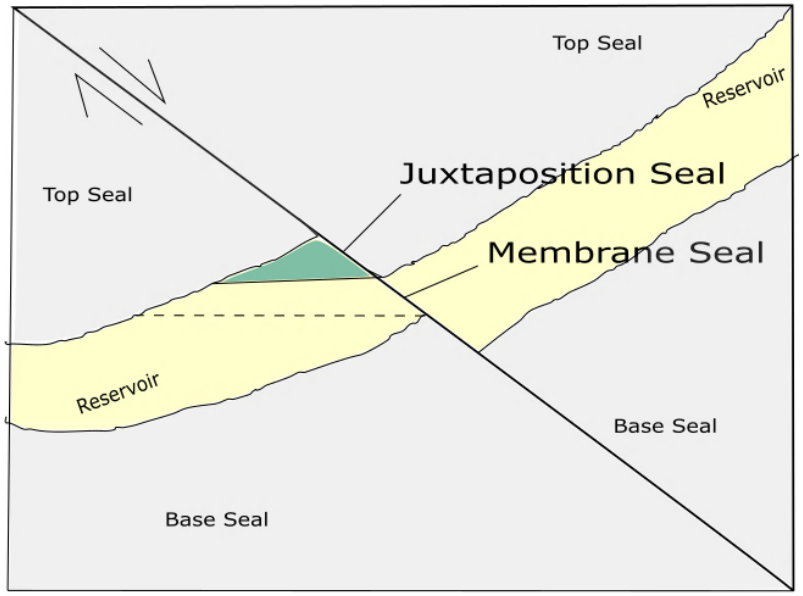


Figure 4: Cross section of a structure trap, displaying a membrane seal and a juxtaposition seal. The juxtaposition seal is trapping fluid (green). The dotted line represents potentially trapped fluid by a sealing membrane fault seal.

such as shearing, gliding, compaction, and breakage of the host rock (Wu et al., 2021). The kinematic mixing consider the mixing of different lithologies of the host rocks during fault slips (Wu et al., 2021). In the following Sections 2.5.1 and 2.5.2 some fault rock algorithms to assess the fault rock seals are briefly presented.

### 2.5.1 Shale Gouge Ratio

Shale gouge ratio (SGR) (Yielding et al., 1997) is a predictive measure of the shale/clay content in the fault zones dominated by shale and sandstone. The SGR can simply be calculated by the equation

$$SGR = \frac{\sum Shale\ thickness}{Fault\ throw} \cdot 100\% \tag{1}$$

where the SGR is calculated for a point on the fault, by considering the shale bed thickness of the sequence that has slipped past this point on the fault (Wu et al., 2021). Simply, the more shaly the rock wall is, the greater the proportion of shale in the fault zone will be.

### 2.5.2 Shale Smear Factor

The shale smear factor (SSF) (Lindsay et al., 1993) is used to calculate the potential effect of shale smear. Lindsay et al. (1993) defined the factor as

$$SSF = \frac{\sum Fault\ throw}{Shale\ layer\ thickness} \tag{2}$$

which gives the ratio of fault throw to shale layer thickness. Take note that the SSF (Equation 2) considers the sealing of only the shale beds, whereas SGR (Equation 1) considers the sealing of a rock sequence with regards to its shale/clay content.

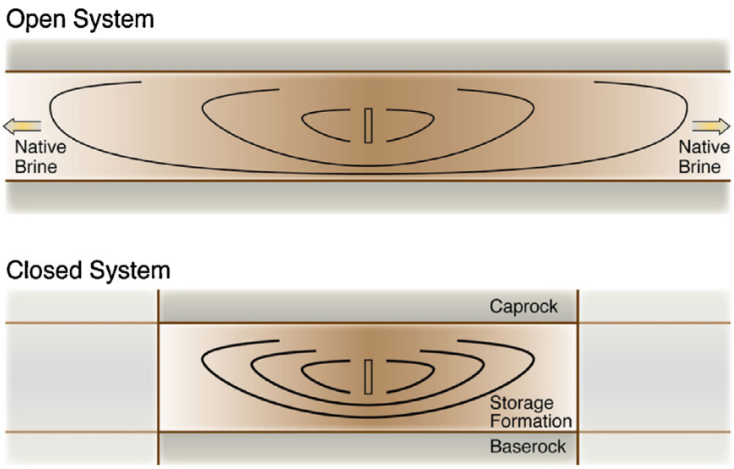


Figure 5: Open and closed storage systems. For the open system the native brine is displaced by the injected $CO_2$. The closed system experiences a pressure build-up as the displaced brine cannot migrate through the sealing closure. From Birkholzer et al. (2015)

## 2.6 Open, Closed and Semi-closed Systems

As fault seals are presented in Section 2.5 one can further distinguish between open, closed and semi-closed storage systems when assessing $CO_2$ storage in saline aquifers.

For an open system, the native brine can easily be displaced by the injected $CO_2$ by escaping laterally, as for instance the example from Figure 1 (a). As storage capacity is described in Section 2.3 as mainly related to the effective rock pore volume, this current practice mainly involves open systems. For closed and semi-closed systems the pressure build-up under injection can have a limiting effect on the storage capacity of the system, as the geomechanical aspects related over-pressure needs to be accounted for (Zhou et al., 2008).

For closed systems, one can consider separate pressure compartments divided in by e.g sealing faults, creating three-way closure. These closed systems will have no pressure communication with each other, and a significant pressure buildup can be produced as $CO_2$ is injected and the native brine cannot migrate through the closed system boundaries (Birkholzer et al., 2015).

However, this scenario of perfectly sealed, closed-off pressure compartments can from a geological point of view be questioned if even exists. Most often, one cannot conclude on perfectly sealing faults, leading to the pressure build-up dissipating potentially through both the fault seals and over- and underlying seals (Zhou et al., 2008). This is the case where we consider the saline aquifer as a semi-closed system, and is perhaps the more true approach to zones of much heterogeneity and faulting. One should further evaluate fault seals with methods such as discussed in Section 2.5 to evaluate what closures are truly sealing. This is a complicated assessment, holding great uncertainty (Rahman et al., 2021). Figure 5 displays a simple illustration of an open and closed system in saline aquifers.

# 3 The Smeaheia Storage Prospect

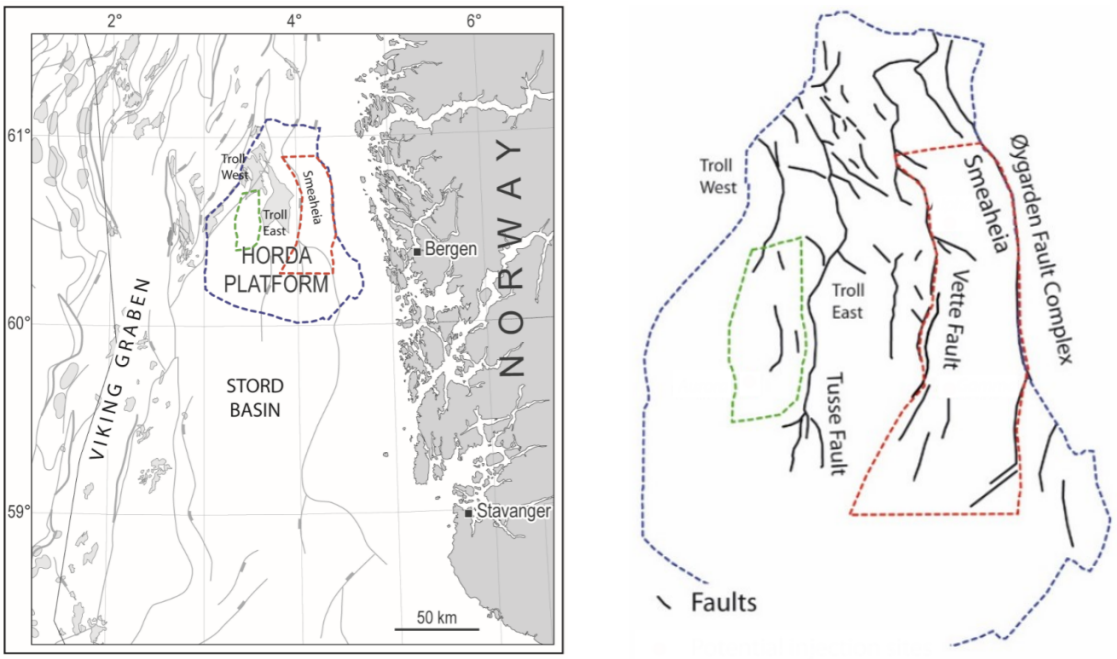


(a) Location of the Horda Platform in the Stord Basin.

(b) The Smeaheia prospect and Troll field in the Horda platform.

Figure 6: (a) shows the location of the Horda platform in the Stord basin. In (b) the Horda platform is presented showing the main faults, being the Tusse fault, Vette fault, and the Øygarden fault complex. The Troll field is located west of the Vette fault and the Smeaheia prospect is located between the Vette fault and the Øygarden fault complex.
From Lothe et al. (2019)

The prospective storage site of interest is the Smeaheia storage prospect. The Smeaheia site is located on the Horda platform in the Stord basin, in the northern part of the north sea (Mulrooney et al., 2020). The prospect is based in sandstone formations belonging to the Viking group, referred to as the Sognefjord delta aquifer (Brobakken, 2018).

Smeaheia was first proposed a potential storage site in 2014, under the name 'Troll Kystnær' (Braaten et al., n.d.). The site was considered as initial storage site for the Northern Lights project, but it was further concluded that the site has too much uncertainty. However, the Smeaheia remains relevant in terms of possibilities for additional storing related the above-mentioned project (Wu et al., 2021).

The study area is located around 20-35 km offshore western Norway (Lothe et al., 2019), and around 20 km east of the producing Troll gas field. It is highly likely that the Troll field production will impact the pressure development under the thought $CO_2$ injection, and to which degree is impacted by several factors. However, the convenient depth of the formations can likely ensure a supercritical phase for the injected $CO_2$, as the pressure and temperature will be above the critical point (Brobakken, 2018).

As seen in Figure 6 (b) Smeaheia is a fault block bounded by two north-south striking faults, the Vette fault in west and the Øygarden fault in east. Further, the geological setting and faults will be assessed.

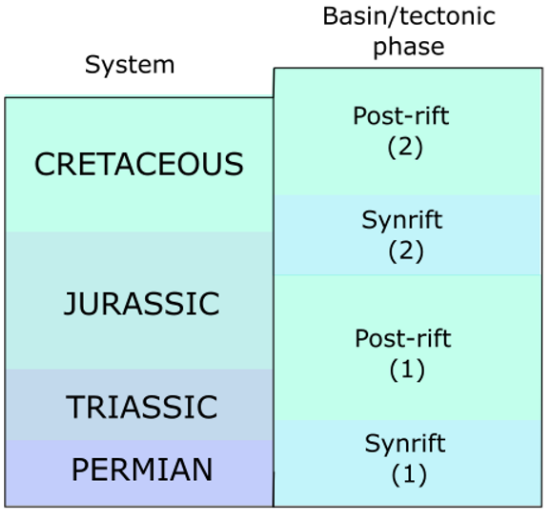


Figure 7: Occurrence of tectonic events in relation to the geological timescale for the North Sea.

## 3.1 Geological Setting

*The content in this subsection is from my Specialization Project:*
*Developing an approach for optimizing pressure management in fault compartments under $CO_2$ injection in saline aquifers - A preliminary application to the Smeaheia Storage Prospect.*
*Author: Eline Nybråten. December, 2021*

The Horda platform can be described as a structural high, extending over a 300 km long and 100 km wide area (Mulrooney et al., 2020). The platform has gone through a series of tectonic events, where one further can consider two main extensional events. The first event was an W-E directed extension (Mulrooney et al., 2020), occurring in the late Permian - early Triassic, presented as Synrift (1) in Figure 7. The second event was in the late Jurassic – early Cretaceous, presented as Synrift (2) in Figure 7.

Synrift (1) is likely a result of the break-up of the Pangean supercontinent (Wu et al., 2021), affecting the North Sea basin as a whole. In the second tectonic phase, marked Post-rift (1), the Horda basin is somewhat stable, and the Statsfjord, Dublin, Brent and the Viking group are deposited during the early to middle Jurassic (Harris, 2019). These are mostly fluvio-deltaic and shallow marine sediments (Wu et al., 2021). In the late Jurassic to early Cretaceous the basin experiences rifting again (Synrift (2)), likely caused by an Early Jurassic rise and Late Jurassic deflation in addition to far field stress from rifting in the Northern Atlantic (Ravnås & Steel, 1997). This synrift results in pre-existing faults being reactivated and creating half-graben structures throughout the basin. These faults are characterized as large-scale N-S striking faults (Mulrooney et al., 2020), as the Vette-, Tusse-, and Øygarden faults (Figure 6 (b)). These are first-order faults, and are basement involved (Silver, 2021).

In addition to the reactivation, smaller second-order NW-SE striking faults were activated. These faults are typically in the 2-10 km scale (Mulrooney et al., 2020). The Draupne Fm is deposited during the early phase of this second synrift, consisting of deep-marine mudstone deposits. This formation can be considered the primary sealing unit of the considered prospect. After this second synrift the basin experiences another post-rift described as a thermal subsidence phase (Wu et al., 2021) which lasted out the Cretaceous and into the Cenozoic period. A simple representation of the occurrence of the mentioned tectonic events in relation to the geological timescale is illustrated in Figure 7.

The study area of interest is within the Sognefjord, Fensfjord and Krossfjord formations in Smeaheia. The formations are located at a depth range of 1200-1700 meters (Paasch et al., 2017). The Krossfjord and Fensfjord formations were deposited during the Upper middle Jurassic, and the Sognefjord formation in the upper Jurassic. The Sognefjord formation consists of well-sorted, medium to

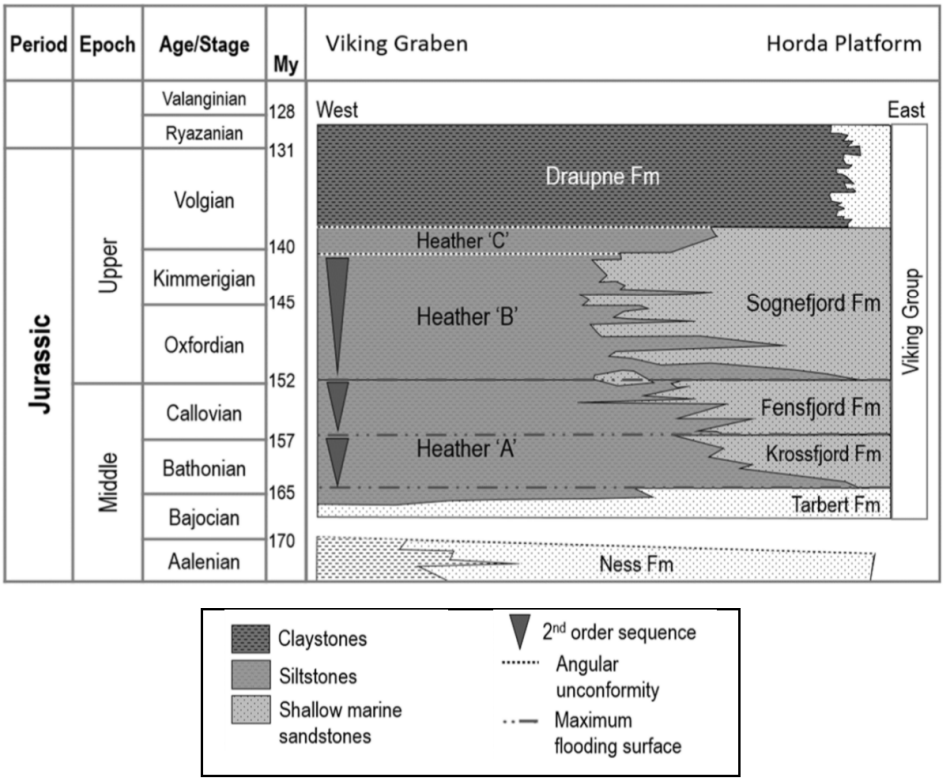


Figure 8: Chronostratigraphic framework for the Horda Platform and Viking Graben showing the Sognefjord, Fensfjord, and the Krossfjord formation. The three target formations interfinger the low-permeability Heather formation in west. From Holgate et al. (2013)

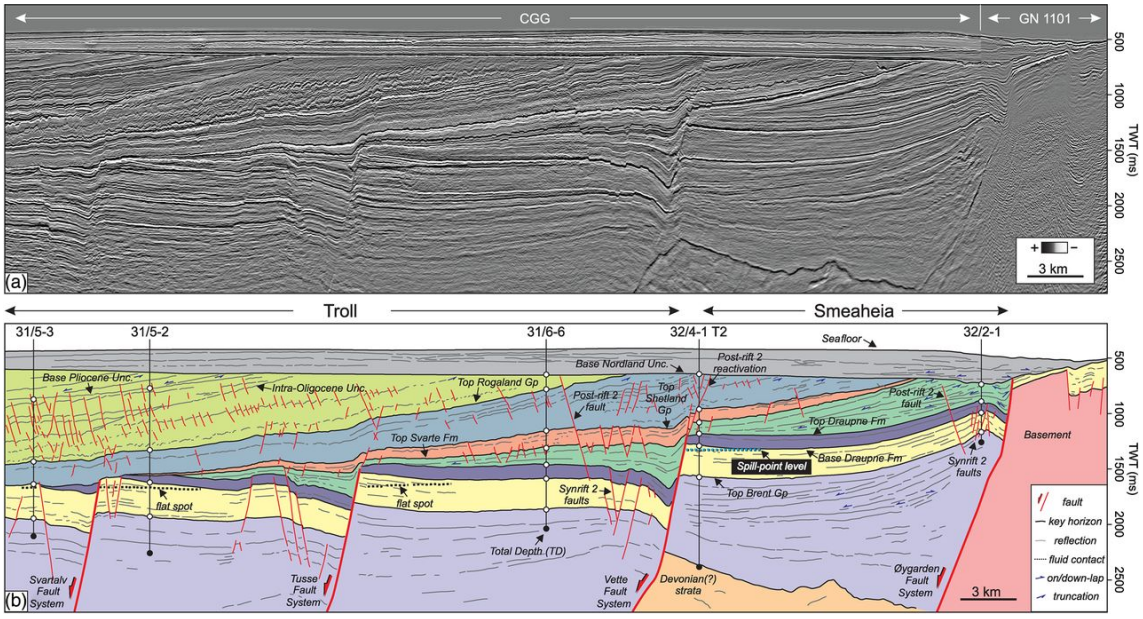


Figure 9: (a) Uninterpreted seismic profile of the Troll and Smeaheia area. The seismic data is from the North Viking Graben surveys, GN1101 and CGG. (b) Interpreted profile of based on well controls and the seismic profile. The profile cuts through the wells 31/6-6, 32/4-1 T2, and 32/2-1. These well locations can be seen in Figure 10. The Smeaheia fault block is bounded by the Vette fault system in west and the Øygarden fault system in east. These are first-order, basement involved faults. From Wu et al. (2021)

coarse-grained sands and sandstones. The formation was deposited by a subaqueous delta system from the Norwegian mainland (Patruno et al., 2015), and is of Oxfordian to Volgian age (Figure 8). The Troll field reservoir is based in this formation, which in the Troll area has a thickness of around 100 -170 meters (Lothe et al., 2019). The Fensfjord and Krossfjord formation consists of shoreline and shelf deposited sandstones, and the two formations add up to a thickness of around 195 meters in the Troll field (Lothe et al., 2019). These surfaces are relatively uniform in thickness, indicating little tectonic influence (Holgate et al., 2013). The Draupne formation consists of claystone, and has a thickness of around 100m in the Smeaheia area (Rahman et al., 2021). The organic-rich formation works as a sealing cap rock, overlaying the target formations. The chronostratigraphic framework is seen in Figure 8. In addition to the mentioned target formations, which is the further focus of this study, there are other potential storage units in Smeaheia, including the sandstones of the Hegre, Statfjord, Dunlin and Brent groups (Wu et al., 2021).

Lothe et al. (2019) states permeability values for the target sands in the Troll field in the order of 1-20 Darcy, and a porositiy range within 19-34%. Such high porosities and permeabilities condition a comparatively high storage capacity, and can improve spreading of the $CO_2$ plume in the reservoir.

## 3.2 The Fault System & Data

The tectonic events described in Section 3.1 let to a complex fault system in the Horda Platform. Figure 9 shows an uninterpreted seismic profile (a) and followingly an interpreted profile based on well data and seismics through the Troll and Smeaheia field (b), where one can see the faults cutting through the formations. The Smeaheia fault block has a similar stratigraphy and faulting patterns as the Troll fault block, although it has experienced slightly more erosion and uplift than Troll (Figure 9) (Wu et al., 2021).

Figure 10 shows a fault map based on the base level of the Draupne Fm. The map shows both the larger, N-S trending first order faults, as well as the smaller NW-SW trending faults as presented in Section 3.1. The fault map in Figure 10 is rather equivalent to the Equinor 2019 simulation grid that was used as the basis for selection of pressure compartments for this study, presented in Section 6.1. The simulation grid is officially shared with NTNU Center of Geophysical Forcasting (CGF). Horizons and faults (Appendix A ) are from the Smeaheia Dataset from the $CO_2$ datashare ('SMEAHEIA dataset', n.d.), where depths are converted by CGF.

The compartmentalization is based on the concept that the faults are to some degree sealing, creating three-way closure. To which degree the faults are sealing depend on a series of properties, and will affect the reservoir pressure predictions. These properties have complicated, uncertain parameters (Rahman et al., 2021) requiring further fault seal analysis.

## 3.3 Fault Seal Analysis

As the fault system of Smeaheia is presented in Section 3.2 we see that this is a zone of much faulting, where one likely cannot consider an open system under the thought $CO_2$ injection. An either closed or semi-closed system (as described in Section 2.6) should be considered. Predicting storage capacity and reservoir pressure behavior is then highly based on the fault seals and their degree of both across-fault and along-fault pressure communication (Wu et al., 2021). As discussed in Section 2.4, the fault seal capacity is mostly dependent on the permeability, which is again highly dependent on the amount of fine grained material in the fault rock. In addition to the membrane fault sealing, the fault juxtapositioning is highly relevant.

Fault seal analysis of the Smeaheia area has been assessed in a series of studies such as Wu et al. (2021), Mulrooney et al. (2020), Michie et al. (2021), and this subsection will summarize some key findings in terms of fault seal capacity.

When assessing the fault seals, it is favourable to distinguish between the larger, first order N-S trending fault seals, and the smaller NW-SE trending second-order fault seals, that were presented in Section 3.1, see Figure 10.

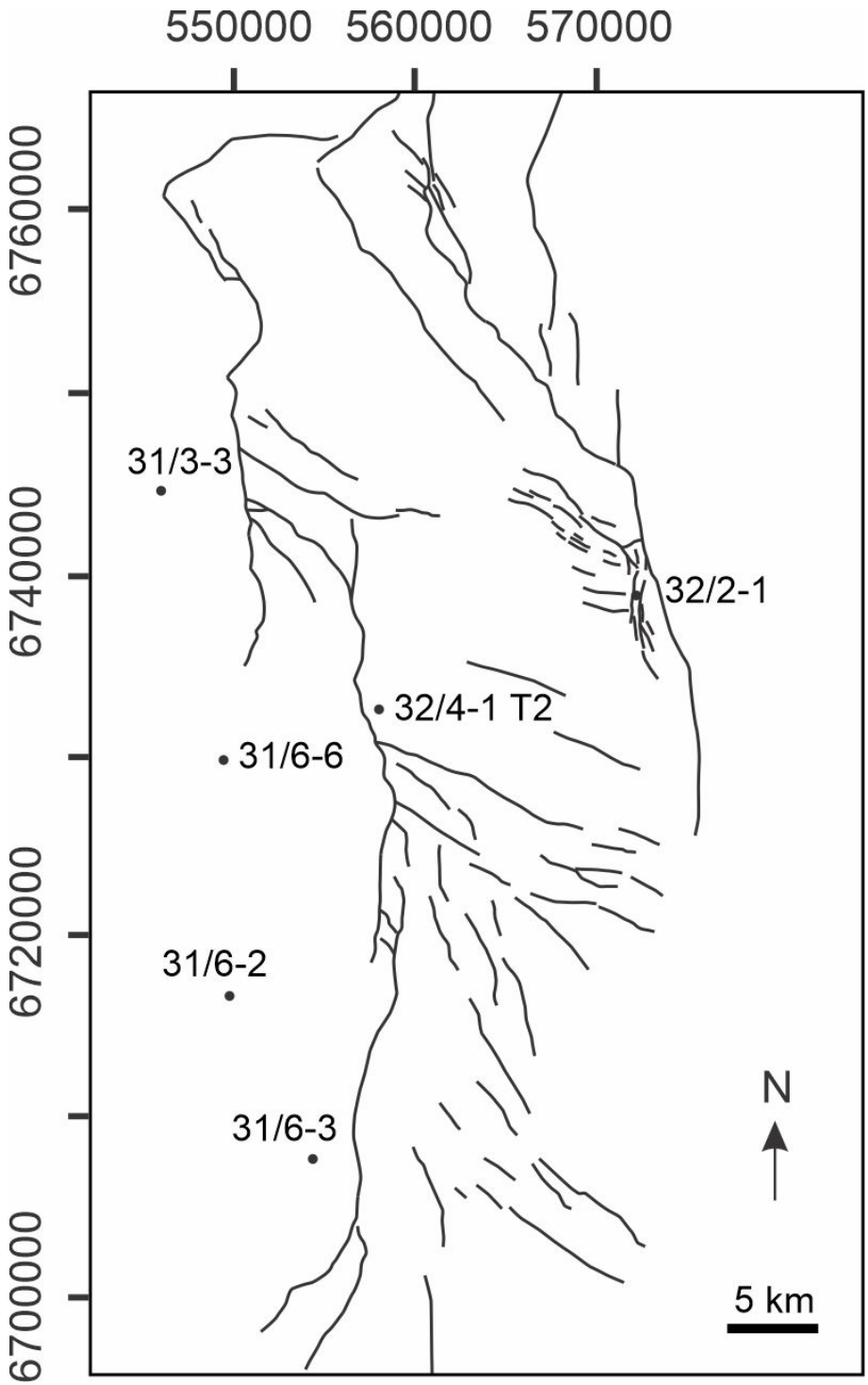


Figure 10: Fault map of the Smeaheia storage prospect based of the base of the Draupne Fm. The map is received from Long Wu.

### 3.3.1 The First-Order Faults

The first-order faults are the two basement involved faults bounding the fault block, the Vette fault and the Øygarden fault (Mulrooney et al., 2020), as seen in Figure 9 (b).

The evaluated studies conclude on good sealing possibilities along the Vette fault, as the storage formations are juxtapositioned up against the Cromer Knoll Group (Mulrooney et al., 2020). Additionally, Wu et al. (2021) studied the membrane seal by considering the SGR and SSF of wells 32/4-1 T2, 32/2-1, 31/3-3, 31/6-6, 31/6-2, and 31/6-3 (See well locations in Figure 10) , anticipating high SGR values (20-40%) for faults of throw larger than 150m, such as the first-order faults. However, the Øygarden fault complex is expected to have high along-fault and across-fault flow risks.

### 3.3.2 The Second-Order Faults

The smaller, NW-SE trending faults are referred to as the second-order faults. The fault are thin-skinned and have throws ranging at approximately 15-90 m (Mulrooney et al., 2020). The evaluation studies conclude on not so prominent sealing for this fault population. The Wu et al. (2021) study shows low SGR values at less than 15-20% for the faults with throws from 20-50m.

# 4 Optimization of Pressure - The Approach

As a conclusion to the brief summary of fault seal analysis in Section 3.3 we will further consider the Smeaheia prospect as a region of closed and semi-closed systems when approaching pressure optimization under $CO_2$ injection. Using simplified fault extensions and some artificial boundaries fault compartments are created, where one as a start will consider each compartment as a closed off system. A further though is to inject $CO_2$ into each compartment separately, with one well per compartment. Pressure analysis and valid pressure predictions are crucial for these systems, as the pressure will likely be what limits the storage capacity.

The pressure analysis approach to be evaluated in this thesis was put together and assessed in my earlier Specialization project (not published). The approach is aimed to optimize basin pressure under though $CO_2$ injection in multiple rock compartments, and was meant to point the way to the fuller analysis presented in this study. The following sections will present how the approach was put together combining a simple box volume approach with a basin geo-pressure approach from Ringrose and Meckel (2019). The result is a complicated equation based on a series of parameters as seen in Figure 13.

*The content in the following subsections are from my Specialization Project:*
*Developing an approach for optimizing pressure management in fault compartments under $CO_2$ injection in saline aquifers - A preliminary application to the Smeaheia Storage Prospect.*
*Author: Eline Nybråten. December, 2021*

## 4.1 The Box Volume Approach

A pressure-volume relationship in porous reservoir rocks can be studied by considering the compressibility of the reservoir rock (Ceia et al., 2019). Reservoir rock is compressible as the pore pressure decreases, and the compressibility can further be measured by quantifying the relationship between the pressure exerted and the change in pore volume (C. Li et al., 2004).

The box volume approach is based on the bulk rock compressibility equation. This equation can be derived from the formula for bulk modulus, which describes how resistant a box volume will be to compression. The box volume is for our case the total pore volume of a rock compartment, and the compressibility would be the compressibility of the reservoir rock. The bulk modulus volume formula is given as

$$K = -V\frac{\Delta P}{\Delta V} \tag{3}$$

where $K$ is the bulk modulus in pascal, V the volume in $m^3$, $\Delta P$ the pressure change in Pascal, and $\Delta V$ the change in volume in $m^3$. Knowing the relationship between compressibility $C_b$ and bulk modulus K which is $C_b = 1/K$, one gets the following compressibility equation:

$$C_b = -\frac{1}{V_b} * \frac{\Delta V_b}{\Delta P} \tag{4}$$

The equation simply shows the relationship between compressibility, rock volume, pressure change and volumetric change. This implies that by assuming the reservoir compressibility and knowing its volume and the change in pressure, the volumetric change the box will experience can be found. In the case where this pressure change is considered a result of injecting $CO_2$ into the box volume, the volumetric change of the box can be found for a box with known size and compressibility. This volumetric change can further be used to estimate mass of injected $CO_2$ into a box volume by considering the density of $CO_2$ at a selected box depth.

It is important to take note that rock systems are a lot more complex than what these simplified assumptions would imply, and important aspects such as the compressibility of the fluid is ignored. The equation considers isothermal conditions (Satter & Iqbal, 2016).

Another crucial assumption that is important to have in mind is the assumption of a perfectly defined, sealed geometric box, which one from a geological point of view should question if even exist. However, this physics driven approach presents a relationship between box size and compressibility that can be quite interesting to assess further.

## 4.2 The Basin Geo-pressure Approach

Another approach for $CO_2$ storage assessment is the basin geo-pressure approach. The approach is based on the concern that the injection pressure cannot exceed a certain rock mechanical pressure limit in the formation.

Although geological traps such as structural and stratigraphic trapping is essential for a $CO_2$ storage site to attain a sufficient storage capacity, it is said to be the reservoir pressure that ultimately limits the injection and total storage capacity at the Gt-scale (Ringrose & Meckel, 2019). With the pressure limiting the storage capacity, pressure-functions per well can together with the initial pressure of the compartment be used to estimate the storage capacity through a generic basin pressure approach.

The basin geo-pressure approach is based on the integration of the injectivity equation over the storage project lifetime. This is derived from considering the injectivity index of an injection well, given by

$$I_{CO_2} = \frac{q}{p_{fbhp} - p_{res}} \tag{5}$$

where $I_{CO_2}$ is the injectivity index in $m^3$/day/bar, $q$ the flow rate in $m^3$/day , $p_{fbhp}$ the flowing bottom hole pressure in bars, and $p_{res}$ the reservoir pressure (far-field), also in bars. Take note that this assumes an incompressible injection fluid. It should aslo be emapsized that Equation 5 considers a constant injectivity, which can be considered a great challenge to maintain in deep saline aquifers of moderate premeability and natural heterogenicities (Miri et al., 2018). Writing Equation 5 as a function of well flow rate $q$, and integrating over the injection well lifetime in the interval $i$ to $f$, one gets the generalized equation

$$V_{injected} = I_c[\int_i^f (p_{well} - p_{res})dt] + F_b \tag{6}$$

where a rate for injected volume $V_{injected}$ is given as a function of the injectivity index $I_c$, the well- and reservoir pressure integrated over time, as well as an additional flux term $F_b$ which represent the boundary condition flux. Note that $I_c$ is actually a constant equivalent to the mean of the injectivity index ($I_{CO_2}$), however referred to as the injectivity index throughout the project.

Experience and knowledge about pressure propagation in porous media leads to a term for the reservoir pressure as a function of the initial pressure, the dimensionless pressure function $p_D(t_D)$, as well as a scaling parameter A related to the reservoir characteristics:

$$p_{res}(t) = p_{init} - A * p_D(t_D) \tag{7}$$

This function illustrates how the reservoir pressure experiences a decay over time. The reservoir pressure is at t=0 (before injection) equal to the initial pressure. $p_D(t_D)$ is further given as a function of dimensionless time:

$$p_D(t_D) = \frac{1}{2} * \ln \frac{4t_D}{\gamma} \tag{8}$$

Combining Equation 7 with the derived equation for the total injected volume in Equation 6 we get the following equation for the storage rate $V_{project}$ given in $m^3/day$ :

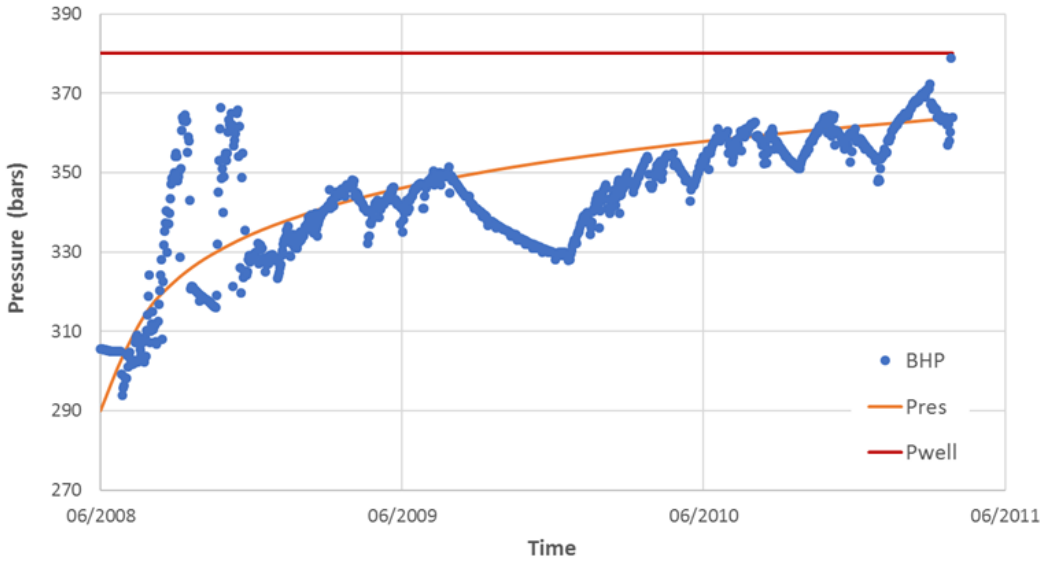


Figure 11: Known pressure history (BHP) of the Snøhvit $CO_2$ injection project matched up against the application of Equation 9, where the reservoir pressure $P_{res}$ under a 3-year injection is calculated with set parameters. From Ringrose and Meckel (2019) (Its associated Appendix)

$$V_{project} = I_c[p_{well} - p_{init} + \int_i^f A * p_D(t_D)dt] + F_b \tag{9}$$

Equation 9 is basis of the basin geo-pressure approach. Note that both injectivity and injection pressure are assumed constant, which should be considered a simplification. For more complex operations one can consider variable gradients through numerical reservoir simulations.

A simple illustration of the utilization of the equation is presented in Figure 11. Known pressure history (BHP) of the Snøhvit $CO_2$ injection project is matched up against the application of Equation 9, where the reservoir pressure $P_{res}$ under a 3-year injection is calculated with set parameters. The initial pressure is set to 290 bar and maximum well pressure at 380 bar. A = 34, $I_c = 40\ m^3/day/bar$ , and $F_b = 0$. By utilizing the equation with the assumed parameters, one can calculate the total storage mass through the total injected volume. One can see that the equation generates a pressure rise that is similar to the pressure history of the injection.

To utilize the basin geo-pressure approach for pressure calculations, one would need adequate estimates for maximum well pressure ($p_{well}$) and initial pressure ($p_{init}$) . The basin geo-pressure approach is often based on similarities and known trends within stratigraphic and tectonic history, emphasising the subsurface fluid pressure profiles of the fracture- and hydrostatic pressure of sedimentary basins. One could use pressure depth functions based on trends of e.g. the Norwegian North Sea to establish estimates of the above-mentioned pressures for a specific depth, by further expecting the initial pressure of saline aquifers to be equivalent to the hydrostatic pressure (Ringrose, 2020) and the maximum well pressure equivalent to 90% of the fracture pressure of the rock. Typical pressure-depth functions for the Norwegian North Sea is presented in Figure 12, and is a useful tool for applying the basin geo-pressure approach at a screening stage.

Bohloli et al. (2017) further emphasises three main approaches for determining the fracture pressure, being (1) theoretical methods, (2) use of a well test database, and lastly (3) analysis of injection data during injection. As the various well-test procedures and analysis during drilling are infeasible, a theoretical approach based on formation conditions and material parameters will be further assessed to determine fracture pressures in this study, presented together with calculations in Section 6.

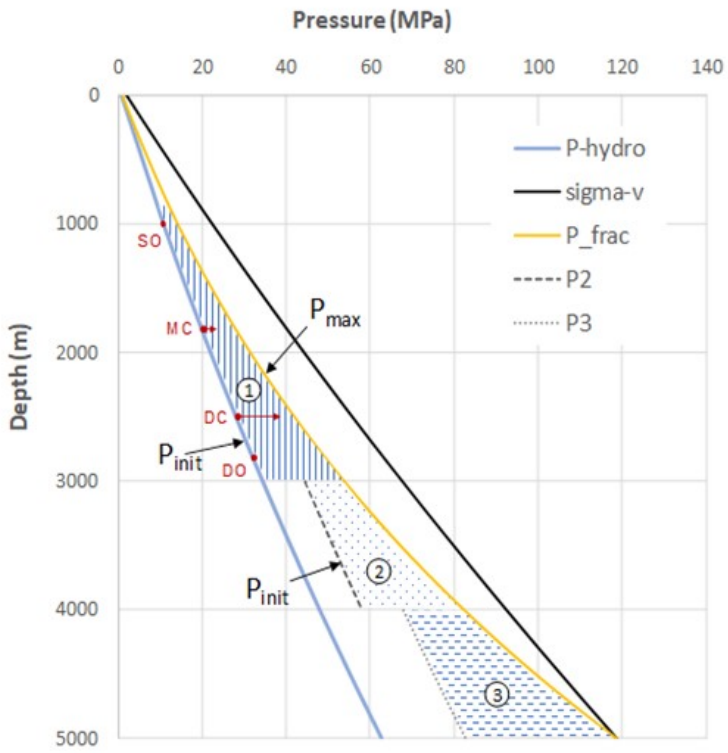


Figure 12: Pressure-depth function based on pressure and stress in the Norwegian North Sea. $P_{hydro}$ illustrates the hydrostatic pressure gradient, sigma-v the vertical stress, and $P_{frac}$ the fracture pressure. Areas (1),(2), and (3) represents a normally pressured region (shallow), and two deeper, more pressurized regions respectively. From Ringrose and Meckel (2019)

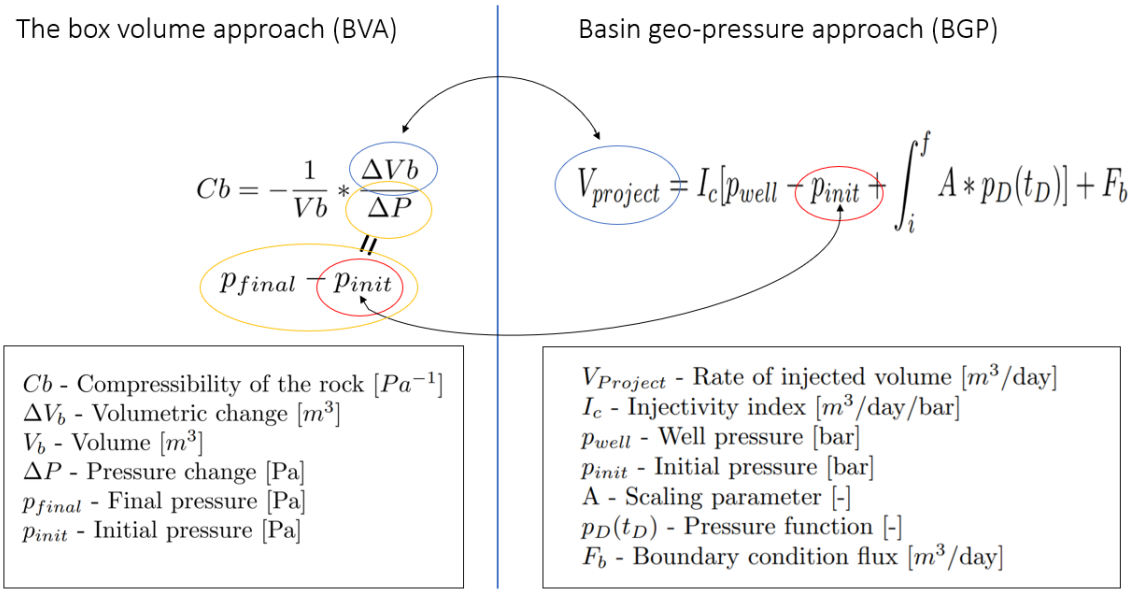


Figure 13: Simple representation of how the two approaches are connected, in addition to the parameters involved, with corresponding units.

## 4.3 Combining the Approaches

The two approaches presented in Sections 4.1 and 4.2 can as mentioned be combined. By relating the change in volume $\Delta V$ from the box volume approach (BVA) to the $V_{injected}$ from the basin geo-pressure approach (BGP) as well as the pressure change $\Delta P$ from BVA to the pressures used for BGP one can further get a complex, interesting equation based on a series of parameters.

Take note that the volumetric unit from the BVA is in $m^3$ whereas the value from BGP is given as a rate, in $m^3$/day. Additionally, the pressure change units for BVA is in Pa, whilst bar for BGP. Take also into consideration that the $\Delta P$ from BVA considers the pressure change $p_{final} - p_{init}$, which is not the same as $p_{well} - p_{init}$ from Equation 9 from BGP.

Figure 13 visualizes how the two approaches are connected, and which parameters are involved. As to our specific case of $CO_2$ injection into the compartments, one can consider the total injected volume of $CO_2$ and resulting pressure rise as the end values of interest.

The approach put together in this section will further be applied to the Smeaheia prospect in Section 6. A significant amount of connected fault blocks are evaluated, where sampling of uncertain parameters can create large clouds of data that vary with time. The impact of the parameters and uncertainty of the data can be studied by numerical analysis approaches such as e.g. clustering algorithms and principal component analysis. Therefore, a short machine learning introduction is included in the following section.

# 5 Machine Learning for Geoscience Applications

## 5.1 How Machine Learning Works

The field of machine learning (ML) has entered most scientific domains in recent years (Carleo et al., 2019). ML refers to a computing branch where instead of being explicitly programmed by humans, programs adaptively learn and form from the data itself (Cutler & Dickenson, 2020). As the algorithms adaptively learn from experience, performance can be improved by intaking information from data directly without relying on a model of predetermined data ('Machine Learning with MATLAB', n.d.). The algorithms find natural patterns and trends in the data, further adapting to build a model that can make predictions and solutions for complex cases with high uncertainties present.

With its broad range of tools and algorithms ML encompasses great potential to geoscience as the field has entered an era of vast amounts of data, and this also includes the deployment of large-scale $CO_2$ storage. Optimizing pressure management under $CO_2$ injection in multiple rock compartments poses complex cases of many parameters, where machine learning is a relevant approach.

There are dozens of machine learning algorithms, all taking different approaches to recognise patterns and learn from the data ('Machine Learning with MATLAB', n.d.). One can further categorize by defining three types of approaches, being supervised, unsupervised and reinforcement learning (Carleo et al., 2019).

### 5.1.1 Supervised Learning

Supervised learning builds models based on known inputs and outputs (Cutler & Dickenson, 2020). To get a simple understanding of the concept, one can consider a data set with input variables and output variables. The input variables, often referred to as the training set (Carleo et al., 2019), is denoted $X$, whereas the output variables, often referred to as the response or dependent variables (James et al., 2013), are denoted with $Y$. Our example data set would then be $n$ number of input variables $X = (X_1, X_2, ..., X_n)$ with corresponding responses to each variable $Y = (Y_1, Y_2, ..., Y_n)$. A general form of this relationship can then be expressed by the following equation:

$$Y = f(X) + \epsilon \tag{10}$$

where $f$ represents a function describing the systematic information that the input variables $X$ provides the responses $Y$ (James et al., 2013). $\epsilon$ is an error term. Take note that the function $f$ in many cases would involve more than one input variable, and that Equation 10 is a rather general form. Having known responses to the sample data, classification or regression techniques can be used to generate predictive models for new data by constructing a function $f$ from the training set ('Machine Learning with MATLAB', n.d.). This method is convenient for cases with sample data for the output one is trying to predict.

### 5.1.2 Unsupervised Learning

Unsupervised learning will learn patterns and build structure from input data without any corresponding output. The most common technique for this type of problem is clustering analysis, which analyzes data to find groupings and hidden patterns ('Machine Learning with MATLAB', n.d.). One can through such algorithms find relationships between the data, and generate models able to develop an internal representation of the data. As mentioned in relation to Equation 10, function $f$ often include more that one input variable. If one as an example considers a data set of observations with two variables $X_1$ and $X_2$ with no associated responses, it is further interesting to cluster groups based on these variables. Clustering the data into such groups could identify differences in the groups with respect to the variables (James et al., 2013). Figure 14 presents a

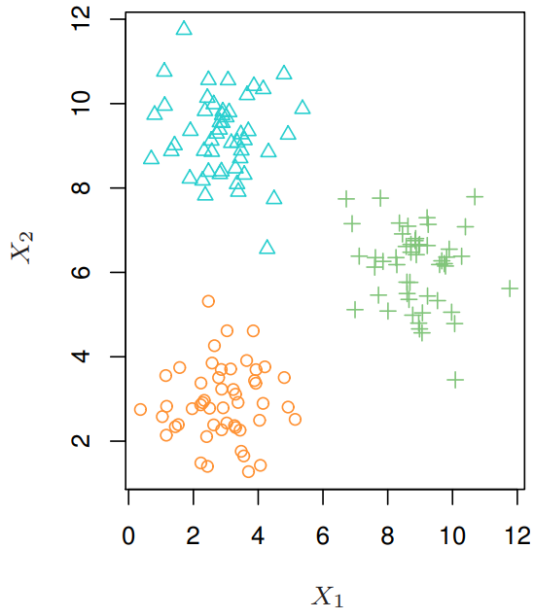


Figure 14: A simple example of clustering of 150 observations based on measurements on two variables, $X_1$ and $X_2$. The clustered data is separated into three groups based on the observed variables. From James et al. (2013)

simple case of clustering. The data is clustered into three, somewhat well-separated groups based on observations from variables $X_1$ and $X_2$. Take note that this grouping, represented with differing colors and symbols is initially unknown, and finding this particular grouping is the goal of the approach.

Reinforcement learning is a third machine learning technique, where an artificial agent learns to find a solution (Buşoniu et al., 2010). Most ML problems fall within either unsupervised or supervised learning (James et al., 2013), and reinforcement learning is therefore not further evaluated for this study.

## 5.2 Subsurface Machine Learning

As discussed in 5.1.2, unsupervised learning works with unlabeled data, and is based solely on the input variables. In contrast, supervised learning works with both input and output to create a fitting model for further input.

A relevant example in regards to this study could be to consider a simple but uncertain parameter as to get into the understanding of machine learning relevance. In subsurface geoscience there is usually little to no ground truth available, and knowing the exact state of a system is often a challenge (Karpatne et al., 2018). Rock porosity is a classic example. One cannot measure rock porosity in a well bore directly, but make a system for rock porosity prediction based on for instance rock density. By considering the initial image of Figure 15, one can see a cross section of two rock units. If one could measure both porosity and density for every possible unit, which theoretically speaking would be possible by running every unit of rock sample through the lab, there would be no need for modeling. This would give us a perfect relationship between density and porosity with no error. However, in a realistic situation one would only have a limited set of samples, e.g. from well tests from a set of wells, as for example in the middle image of Figure 15. One could with this training data (a) where both porosity and density values are known build a model based on physics (Pyrcz, 2019). Figure 15 (b) shows the training data plotted (yellow points) and a model built to fit this data. This model can further be used to predict the porosity of rock units without running them through the lab.

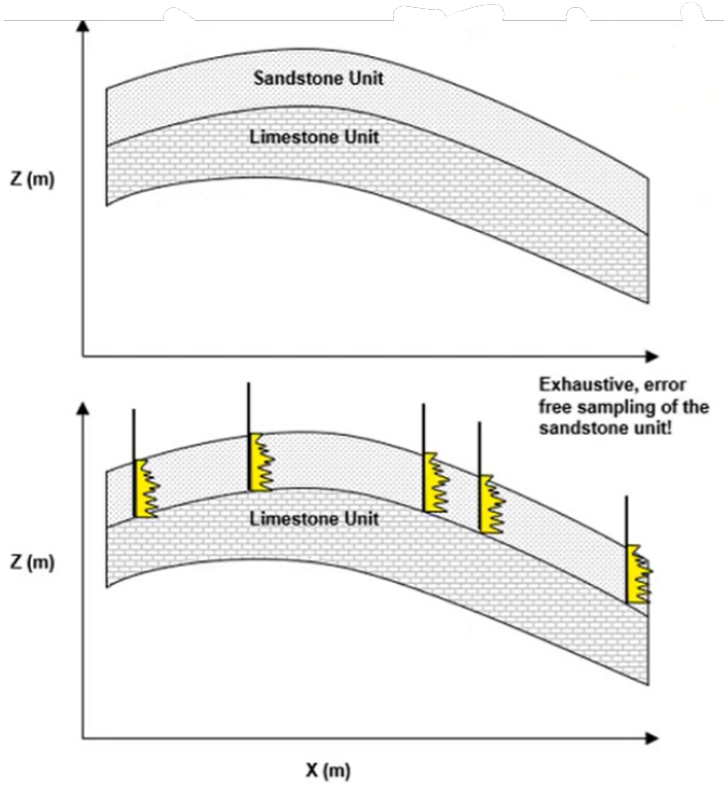


(a) Cross section of two subsurface rock units with a limited set of wells.

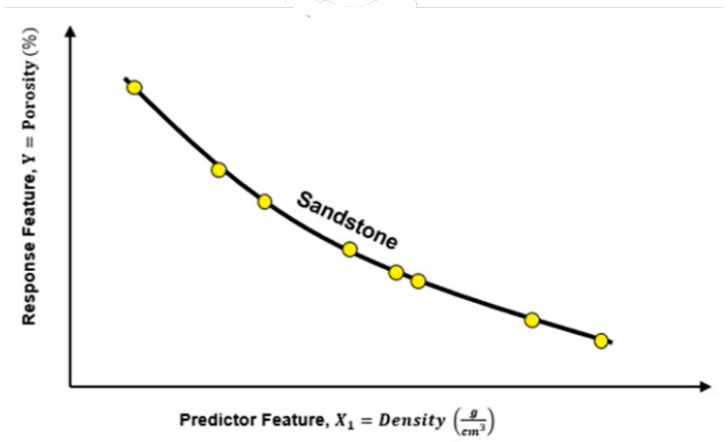


(b) Fitted model showing density-porosity relationship based on training data, being the wells with known density and porosity.

Figure 15: From Pyrcz (2020)

In relevance to subsurface machine learning one will often be working with much more complex, unlabeled data, where the goal is to understand the system (Pyrcz, 2019). As this project assesses optimization of pressure functions in multiple rock compartments, one could argue that the approach put together in Section 4.3 already presents a fitting model to apply to the input. However, one should note that most the parameters to this approach would in a realistic case be unknown, or at best case uncertain, such as in the rock porosity example discussed above. In addition there are likely uncertain and unrevealed relationships between parameters. This calls for unsupervised learning approaches as to understand the system.

Some of the most common unsupervised learning techniques are principal component analysis and the mentioned clustering. Principal component analysis is a tool used for data visualization and data pre-processing before other techniques are applied (James et al., 2013). This study will present a introductory application of principal component analysis, and this method is further presented in the section to follow.

## 5.3 Principal Component Analysis

Principal component analysis (PCA) is an unsupervised learning algorithm used to extract important information from data, expressing the information with a set of orthogonal variables refereed to as principal components (Abdi & Williams, 2010). PCA analyses data tables of several dependent variables (observations), which are generally inter-correlated. Principal components are computed, obtained as linear combinations of the original variables. The objective is to find a low-dimensional representation of the data table that contains as much of the variation as possible.

Understanding the details and mathematics behind PCA require knowledge of linear algebra (Kassambara, 2017). This section will not go into detail of how the analysis is carried out mathematically, however aim to provide the basics for when a PCA algorithm is applied to a data-set.

A first step is to find and select principle components. The first principle component should have the largest possible variance. This results in the larges inertia for the component, which will explain the most of the inertia from the data table. The second principal component should be orthogonal to the first component, and have the largest possible inertia as well. Further components are computed likewise (Abdi & Williams, 2010).

The principal components are found through singular value decomposition of the data table of observations. The amount of variation retained by each principle component is measured by the eigenvalues (Kassambara, 2017). Hence, the eigenvalue of the first principal component is the largest, and smaller for the subsequent components. One can therefore consider the principal component by its eigenvalues, which is equal to the components sum of squared factor scores. The squared factor scores are the values of the new variables for the observations (Abdi & Williams, 2010). One can interpret these factors geometrically, as projections of the original observations onto the principal components.

To determine the ideal number of principal components one can examine the eigenvalues. There is no definite solution as to how many principal components are enough, and further how much of the variation should be explained. Naturally the variation should be as high as possible, with a practical number of principal components (typically 2 or 3 dimensions). One way to determine the number of principal components is through a Scree plot (Kassambara, 2017), which explains the proportion of variance explained for each principal component. Adding up the variance of the principal components one can select a reasonable number of components and corresponding variance sum for the analysis.

In this study the analysis is done based on 2 principle components. A rule of thumb is to only use principle components of eigenvalues greater than 1. The new data can then be presented projected onto the new feature subspace.

A next step is to interpret the principle components in terms of the original variables, as to understand the results. This can be done by considering the eigenvectors, where the magnitude of the absolute value represents the components dependency on the original variables (Kassambara,

2017). A matrix of eigenvectors of the principle components can be extracted, and one can from this gather the components dependency on the original variables, by an either positive or negative association. One should typically utilize specialized knowledge as to determine at what level the correlations shown by the eigenvalues are important.

PCA can today easily be applied to data by available packages, where one can easily extract and visualize results by simple scripts. For this project a PCA Python algorithm by Raschka (2015) was utilized.

## 5.4 Sensitivity Analysis

The approach put together in Section 4.3 has many characteristics that would be interesting to explore. Relationships between the variables are nonlinear and challenging to understand directly. One can then study the sensitivity of input variables on output through sensitivity analysis.

Saltelli et al. (2004) defines sensitivity analysis as the study of how uncertainty in the output of a model can be appointed to different sources of independent uncertainty in the model input. A general way to classify input for this purpose is everything that can drive variation in the output of our model (Saltelli et al., 2008). A sensitivity analysis will further assess the sensitivity of these input variables on the output. Such a study can be used to determine which input parameters contribute more to the output behaviour, and ascertain interaction effects of the model (Iooss & Lemaıtre, 2015).

One of the simplest approaches of sensitivity analysis is a local approach. This is a deterministic approach that looks at the derivative of input parameters with respect to the output parameters at a specific point. The approach allows for a large number of input parameters. However, a local method calls for several limitations, such as local variations and assumptions within e.g. linearity and normality (Iooss & Lemaıtre, 2015). As the derivative will only be representative at its base point, an exploration of the rest of the input parameter space will be missing for for non-linear systems (Saltelli et al., 2008).

Rather than a local approach, one can consider a global approach, known as global sensitivity analysis. This type of approach considers the whole range of input parameters instead of just a specific point. The objectives of such an approach can include finding the most influential inputs of the model, and likewise identify the less influential inputs. By identifying the less- or non-influential inputs one can fix these parameters at nominal values, being useful for further analysis. One can further map output behavior by setting the focus to a specific domain of the inputs (Iooss & Lemaıtre, 2015).

### 5.4.1 Tornado plots

One approach as to assess the sensitivity of input variation on output is through a tornado plot. Tornado plots are typically constructed by varying input parameters at a percentage above and below a mean value of each parameter (Mudford & Kuch, 2003). The result is a diagram displaying the variation that each input parameter will have on the output, further giving good characterization of output drivers, as well as parameters having lower, perhaps negligible impact on the output. Tornado plots can be an important tool in comparing the relative importance of variables (Tian, 2013).

A mean output value is found by setting all input parameters to a mean of their distributions. As each parameter is set to their mean values, one input parameter is varied at the time, where one can find the variance on the output. Tornado plots are generally easy to apply and understand. The factor of highest impact will appear at the top of the plot, the second highest impact beneath that, and so forth. However, the approach is based on the fundamental assumption of independence between the input parameters. This is likely not the case for most realistic projects, and the sensitivity analysis might be incorrect as important correlations and dependencies of the input parameters are ignored (Mudford & Kuch, 2003).

# 6 Problem Definition

As the pressure management approach is put together, the next step is applying it to the basin-scale model. The approach is applied to the faulted Smeaheia storage prospect, and the main objective is to study parameter distributions and their influence on the pressure management approach.

The approach is first applied to data of set parameters, where deterministic calculations are carried out. Following this a more realistic perspective is introduced, where parameters and their connections are considered more uncertain. This perspective calls for data analysis as to understand the complex controls playing in.

## 6.1 Compartmentalization

The first step of applying the pressure management approach put together in Section 4 to the Smeaheia prospect is to divide the area into pressure compartments. This is done by considering the faults in the area as sealing boundaries ($F_b = 0$), creating three-way closures. The review of fault seal analysis done in Section 3.3 is the basis of the compartmentalization, together with simplified fault extensions and artificial boundaries as to create three contrasting scenarios.

The compartmentalization is done in Petrel 2021, where fault polygons with true geometries are generated. Equinors latest grid of 2019 is used, and the fault polygons are manually marked based on the faults presented in Appendix A. Take note that although the fault polygons are based on true faults and analysis of their fault seals, some artificial polygons are built in and extended in order to complete the scenarios. Four different scenarios are presented, ranging gradually from one big open system to a maximum connectivity case of 72 smaller, closed compartments.

Scenario A would be an open system, a case of no sealing faults or boundaries. This specific case is not evaluated for this study, however presented as a possibility. The second scenario, Scenario B consists of 6 fault polygons, B1-B6, and are presented in Appendix B. These fault polygons are based on the major faults of the area, however as for all the compartment scenarios, the boundaries are somewhat artificial and exaggerated to complete the three-way closures. The third scenario is referred to as Scenario C, and is further 12 fault polygons, C1-C12, as seen in Appendix C. These fault polygons are based on Scenario B, with some additional boundaries based on smaller faults. The last scenario is Scenario D, with 24 fault polygons, D1-D24. This scenario is again based on the polygons of Scenario C, with additional smaller faults included. Scenario D is presented in Appendix D.

As scenario D is based of the polygons of Scenario C, and Scenario C of the polygons of Scenario B a hierarchy is created as the polygons are sliced into several smaller fault polygons for each scenario. This hierarchy is presented in Figure 16 and can further be used when assessing the fault seal between the connected compartments by comparing the different scenarios.

The fault polygons presented above are assumed the same throughout the three target formations, although the formations are considered ass three separate layers within the compartment grids. This implies that e.g. Scenario B consisting of 6 fault polygons, in total contain 18 pressure compartments, 6 compartments in each target formation. This results in Scenario C containing 36 pressure compartments and Scenario D containing 72 pressure compartments.

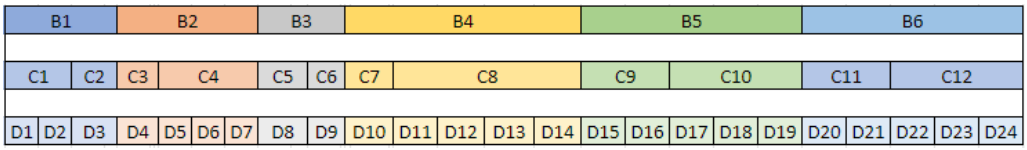


Figure 16: Hierarchy of the fault polygon compartment scenarios. Scenario B considers the prospect area by 6 compartments, branching out to complex scenarios of more, smaller compartments. Scenario C considers 12 compartments, and Scenario D considers 24 compartments.

## 6.2 Collecting Data - Set Parameters

The pressure management approach (Figure 13) is based on a series of parameters. When applying the approach to a fault compartment the input parameters of interest are

- $V_b$ - Total available pore volume
- $I_c$ - Injectivity Index
- $P_{well}$ - Maximum well pressure
- $P_{init}$ - Initial pressure
- $A$ - Scaling parameter
- $C_b$ - Compressibility
- $F_b$ - Flux boundary condition
- $\Delta P$ - Pressure change

and followingly the output parameters of interest are volume of stored $CO_2$ and actual compartment pressure, both as functions of time.

As mentioned, applying the pressure management approach to the created compartments poses complex equations of much uncertainty, as many of the above-mentioned parameters are unknown, or at best case uncertain. Sections 7.1 - 7.4 will focus on cases and calculations based on set parameters for each compartment, where both stochastic driven, math/physics driven and geoscience driven approaches are considered to select and determine the parameters for the calculations. In the following subsections these set parameters are selected specifically for the compartments of the prospect area. However, complex, more realistic cases with distributions of variable parameters are presented later in the study, in Section 7.5 and 7.6.

### 6.2.1 Pressure and Volume

Prior to applying the pressure management approach to the compartments, data was gathered from Petrel (provided data and dataset presented in Section 3.2). Each fault compartment has a generated area size ($m^2$) from the fault polygons from Section 6.1. Formation horizons were used to create thickness maps for the three target formations (Sognefjord, Fensfjord and Krossfjord Fm.) and the thickness of each compartment is found by slicing the thickness maps with the fault polygons. The thicknesses of the Scenario B compartments are presented in Appendix E - G, Scenario C in Appendix H - J, and Scenario D in Appendix K - M. From these maps an average thickness (m) and average depth (m) (from the middle of each compartment) was found. Uncertainty related to thickness and depths are overseen. The porosity was set to 30% and used throughout the initial calculations. However, this is a variable that will vary throughout the compartments, especially for the three formation layers. The total pore volume $V_b$ is found as a function of area size, thickness depth and porosity of each compartment.

The mean depth is further used to find the hydrostatic pressure (P-hydro) for each compartment, utilizing the basic hydrostatic pressure equation

$$P = \rho g h \tag{11}$$

where the specific compartment depths are utilized, together with a brine density of $\rho = 1041$ $kg/m^3$, gathered from the Appendix of Ringrose and Meckel (2019). The fracture pressure ($P_{frac}$) is found by first calculating the vertical stress from equation (Zhang, 2019)

$$\sigma_V = \rho_w g h_w + g \int_{Z_w}^{Z} \rho_b(z) dz \tag{12}$$

where $\rho_b(z)$ represents the formation bulk density as a function of depth. Brine density is denoted $\rho_w$, and $Z_w$ as the water depth. As the vertical stress is calculated for each compartment, the fracture pressure is found by considering equation (Bohloli et al., 2017)

$$P_{F_{max}} = \frac{2v}{1-v}(\sigma_V - P) + P \tag{13}$$

representing the upper bound of the fracture pressure by assuming isotropic horizontal stresses, and neglecting tensile strength and thermal stresses. Estimates of $\sigma_V$ and P are found from Equations (11) and (12) respectively, where $v$ is the Poisson's ratio calculated for each compartment.

The expected initial- and maximum well pressure (bar) used for the basin geo-pressure equation is found for each compartment through these calculations, as the initial pressure $P_{init}$ is set equal to the hydrostatic pressure and the maximum well pressure $P_{well}$ is set to 90% of the fracture pressure for each compartment.

Another pressure parameter necessary for the pressure management calculations is the maximum pressure change $\Delta P$, for the box volume approach equation. This parameter represents the maximum over pressure of a compartment, and would also realistically vary from case to case. A set parameter was chosen by considering real cases and true data of injection pressure change, and 5 MPa was selected for initial calculations. Some additional values are tested further is Section 7.3.

### 6.2.2 Scaling Parameter A and Compressibility

The next step to fulfill the list of input parameters of the approach is to find a function for the scaling parameter A. By considering the pressure management approach of Figure 13 on base cases of known parameters one can conceptualize a relationship between the scaling parameter A and the area size of a box compartment, in which can be used when applying the approach to the fault compartments put together in Section 6.1.

To find this relationship five base cases were put together, representing five different box compartment sizes, shown in Figure 17. According to Bachu (2015) typical compressibilities of reservoir rocks lie in the range of $3 - 70 * 10^{-10}\ Pa^{-1}$. The basin-geo pressure approach is applied to the base cases by choosing an injection timescale of 25 years, and setting equal values for porosity, pressure limits, boundary condition flux (=0) and injectivity for the constructed base cases. Simplistic, linear functions for the relationship between the scaling parameter A and compartment area size is constructed for compressibilities $1 - 5 * 10^{-9} Pa^{-1}$, as presented depicted Figure 18. The scaling parameter A decreases with increasing area size of a box. For the initial calculations the compressibility of $3 * 10^{-9} Pa^{-1}$ is selected, as this is an average value.

| Box dimensions | | | | | |
|---|---|---|---|---|---|
| | X | Y | Z | Poro | Vb |
| **Enormous aquifer (XXL)** | 20000 | 10000 | 100 | 0,3 | 6000000000 |
| **Larger aquifer (XL)** | 10000 | 16000 | 100 | 0,3 | 4800000000 |
| **Large aquifer (L)** | 10000 | 12000 | 100 | 0,3 | 3600000000 |
| **Medium aquifer (M)** | 8000 | 10000 | 100 | 0,3 | 2400000000 |
| **Small aquifer (S)** | 1000 | 40000 | 100 | 0,3 | 1200000000 |

Figure 17: Box dimensions for five base cases used for conceptualizing a simplistic relationship between A and box area size. The boxes have three dimensions X,Y,Z, and a porosity of 30%.

Take note that this simplistic approach assumes a linear relationship between A and area size, which might not be the case. This linear approach will at some point pose a concern regarding negative A values as the area size of the compartments increases (see Figure 18). This is further discussed is Section 8.1.

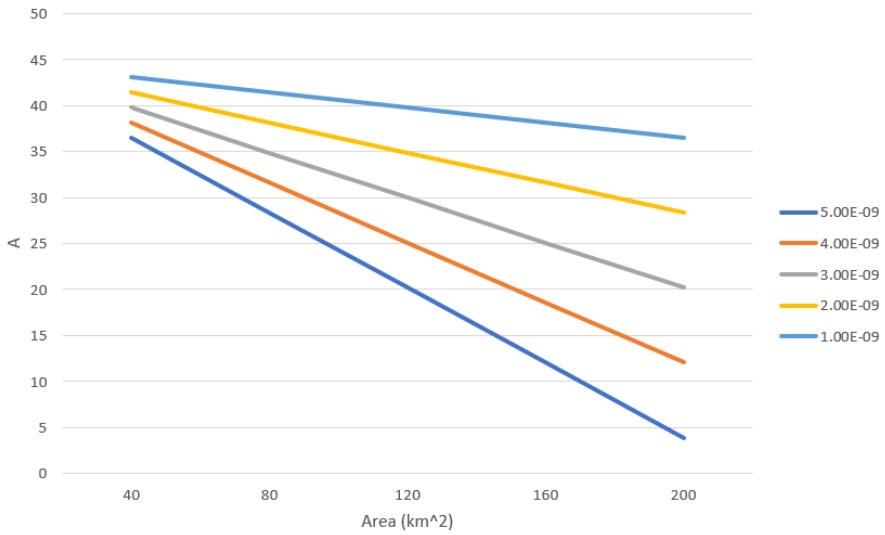


Figure 18: Relationship between the scaling parameter A and the area size of a box compartment. The graphs show five different compressibilities, $1 - 5 * 10^{-9} Pa^{-1}$.

### 6.2.3 Injectivity index, Boundary condition flux and Density

The injectivity index $I_c$ and boundary condition flux $F_b$ should also be determined for initial calculations.

For the concentration of $CO_2$ to be mitigated significant injection rates in the order of 10 Mt $CO_2$/year will be necessary for large-scale projects of $CO_2$ storage (Miri et al., 2018). However, Ringrose and Meckel (2019) states that realistic average rates for offshore cases lay at 0.7 Mt/year/well as of now. For initial calculations an injectivity index of 40 $m^3/day/bar$ was assumed. This range was later found a little low in comparison to real cases in the North Sea. Therefore higher, presumably more realistic ranges are tested for the variable distribution parameters, to be presented in Section 6.3.

The last factor to consider is the boundary condition flux $F_b$. Naturally this is an important factor to consider when assessing the pressure behavior of the fault compartments. A three-way sealed compartment with no communication with its connected compartments will have a no-flow boundary condition, $F_b = 0$. Pressure dissipation from a compartment would further result in a positive flux value, whereas influx into a compartment would give a negative flux value. As stated by Ringrose and Meckel (2019) (Appendix) the boundary condition flux can generally be considered a small factor compared to the injectivity term (Equation 9), which poses the question of weather one to a certain degree can oversee such a factor if the injection rate is high enough, even if faults are not truly sealing. However, it is further stated that for cases of no boundary limitations the $F_b$ can become significantly dominant. This concludes that the boundary condition flux is in fact an important factor to the pressure behavior. One should further study such a factor through fault seal analysis, as briefly presented in Section 3.3. This brief analysis is used to carry out the compartmentalization of Section 6.1 such that it can be reasonable to set the boundary condition flux $F_b = 0$ for the compartment calculations. Take note that this is a much simplified assumption, as a majority of the faults were found not to be prominent seals.

Additionally, the density of the $CO_2$ should be evaluated for storage mass calculations. The pressure management approach calculates the volumetric change that each compartment experiences. To calculate how much $CO_2$ these volumetric changes correspond to, the density is assumed to be constant at 790 $kg/m^3$ for the initial calculations.

### 6.2.4 Selected Parameters for initial calculations

A summary of the parameters that are selected above and used for the initial calculations are presented below.

- $\rho = 790\ kg/m^3$
- $I_c = 40\ m^3/day/bar$
- $C_b = 3 * 10^{-9}\ Pa^{-1}$
- $F_b = 0\ m^3/day$
- $\Delta P = 5\ Mpa$

## 6.3 Collecting Data - Distributions for Variable Parameters

As the parameters in Section 6.2.4 are used for initial calculations to evaluate deterministic results and compare the scenarios with the pressure management approach, it is further interesting to select distributions for variable parameters as to take account for uncertainty and inconsistency in characteristics.

One should further consider a selection of distributions for parameters such as porosity, compressibility, density, the injectivity index, and pressure change.

Porosity was set to 30% for all compartments for initial calculations. This is a great simplification as such a reservoir property is expected to vary both laterally and within the the three target formations. Based on wellbore- and core analysis data of wells 32/4-1 and 31/3-3 gathered from NPD's factpages ('FINAL WELL REPORT 32/4-1' (1996), 'FINAL WELL REPORT 31/3-3' (1985)) in addition to stated porosity values found in articles such as Fawad et al. (2021), Bøe et al. (2002) and Brobakken (2018), ranges were put together for average porosity of the three formations. The ranges should be considered a "range of average", rather than any porosity that could occur. The ranges considers a variation in the depth domain, i.e between the three formations, and to an extent laterally as each formation considers a range of expected porosity. The porosity ranges selected for the three formations came to:

- Sognefjord : 27-32 %
- Fensfjord : 26-28 %
- Krossfjord : 21-25 %

The next parameter to assess is the compressibility, which was set to $3 * 10^{-9} Pa^{-1}$ for initial calculations. The compressibility distribution was set narrowed from the Bachu (2015) range, to $3 - 7 * 10^{-9} Pa^{-1}$. Take note that the range in compressibility changes the scaling parameter A accordingly, such as illustrated in Figure 18.

The $CO_2$ density was set to 790 $kg/m^3$ for initial calculations. However, this is a variable expected to vary with depth and temperature. The Nist online database (Linstrom & Mallard, 2015) was used to find a relationship between density and initial pressure of the compartments, and an average value was set for each formation layer. This is naturally a value that could be calculated specifically for each compartment, but as the depth and temperature also would vary within each compartment, an average was found for each layer. The calculated average density came to:

- Sognefjord : 697 $kg/m^3$
- Fensfjord : 677 $kg/m^3$
- Krossfjord : 675 $kg/m^3$

As mentioned, the injectivity index selected for initial calculations was found to be low when comparing to real data. Typical numbers from known $CO_2$ injection sites were used to set a new range. The Sleipner storage project has an average injectivity index of around 1500 t/d/bar, whereas the Snøhvit field has an injectivity index of around 35 t/d/bar. As one could expect these two referances as more of an upper and lower bound of a realistic range for our Smeaheia case. The following values were selected, converted to $m^3/day/bar$ by the density values selected above:

- Sognefjord : 1000 t/d/bar $\rightarrow$ 1500 $m^3/day/bar$
- Fensfjord : 500 t/d/bar $\rightarrow$ 725 $m^3/day/bar$
- Krossfjord : 50 t/d/bar $\rightarrow$ 75 $m^3/day/bar$

Lastly the pressure change $\Delta P$ is selected based on real data. The Snøhvit $CO_2$ storage site has taken excess pressure to around 7 MPa (Pawar et al., 2015), and this will be set as an upper case. As this is a considerably high excess pressure, a middle case is set to 5 MPa, which is the value mostly used throughout the calculations. For a lower bound case one can consider a typical threshold for shallower formations, which often have $\Delta P$ less that 1 MPa. One could here use the Slepiner storage site (Cavanagh & Haszeldine, 2014) as a rough reference, and set the excess pressure to 1 MPa .

The above-mentioned parameter distributions are used for the results found in Section 7.5, 7.6, and 7.7.

## 6.4 Scripts

As parameters and calculations are set the approach can be applied to the fault compartments. A script was put together in Python, calculating the equation of Figure 13 as a function of time for a selected compartment, reading from a spreadsheet with the compartment data from Petrel. The script calculates the reservoir pressure under injection, over a selected injection period (50 years used for all calculations presented). If any of the working constraints or the maximum well pressure of a compartment is reached, the injection is stopped and the pressure of the compartment start decaying towards the initial pressure. Resultingly, the total storage volume and mass of injected $CO_2$ is calculated for each compartment.

A sample of the script is presented in Appendix N. This script can be considered the initial foundation to all code used for the results of this study. However, there are several extended versions to this initial script, which is meant as a general demonstration as to how the scripts apply the pressure analysis approach to the compartments.

## 6.5 Data analysis

In this chapter two types of parameter cases have been selected. The set parameters of Section 6.2 will be used for initial calculations on the compartments as to present and assess how the approach works on compartments of different characteristics and properties. Interesting relationships between parameters and several characteristic behaviors could be found from this work, as well as a good pointer towards understanding the system.

Nonetheless, when considering a real case of applying the approach, things are more complex. Most input parameters are uncertain, and many of the characteristic behavior and relationships found (such as the relationship between scaling parameter A and area size conceptualized in Section 6.2.2) should be considered simplified assumptions that in reality would be a lot more complex. Additionally it should be mentioned that there are likely also connections and relationships between parameters that are overseen and hard to detect at this stage, as for instance the porosity connection to compressibility and injection index connection to density to name a few.

When applying the pressure management approach to the cases of set parameters and established connections, one could consider this as a fitted model which will produce output (compartment pressure and total stored $CO_2$ mass) from new, sampled input (input parameters to the equation Figure 13). However, the uncertainty around the parameters and their relationships lead the way to a different type of approach. The fitted model of Figure 13 is too uncertain to consider on new input data. As mentioned in relation to subsurface machine learning in Section 5.2, a better fitted model can be found for the data by considering groupings and hidden patterns of the data.

With the distributions selected in Section 6.3 one can create clouds of data that can further be interesting for data analysis as to explore characteristics and controls of the system. Additionally, the distributions are used for a basic sensitivity analysis of total stored $CO_2$ mass as output.

One could state that most scientific domains often have data sets of more than 3 variables. The approach put together in Section 4.3 consider many inter-correlated variables, such as porosity, compressibility, permeability, injectivity, flux and pressures. When applying this approach to the numerous compartments put together, all these variables are considered for each and every compartment. It could be very difficult to visualize and further analyse data of such a multi-dimensional hyperspace. Principal component analysis will therefore be carried out, as a initiation of introducing machine learning to this very complex problem.

# 7 Results

## 7.1 Some Example Calculation with Set Parameters

As set parameters and calculations were presented in Section 6.2, a natural first step is a simple review of how the pressure analysis approach is applied to the compartments. The script presented in Appendix N is tested on some selected compartment as to get an understanding of concepts.

Four compartments are considered for this initial review, being B2, C3, B5, and C4 (See Appendix B and C) in the Sognefjord Fm. These compartments are chosen specifically as they have quite different properties and characteristics, giving four quite different pressure behavior scenarios. Figure 19 show the pressure function obtained from the mentioned script based on the pressure analysis approach (Figure 13), and the results are summarized in the table of Figure 20.

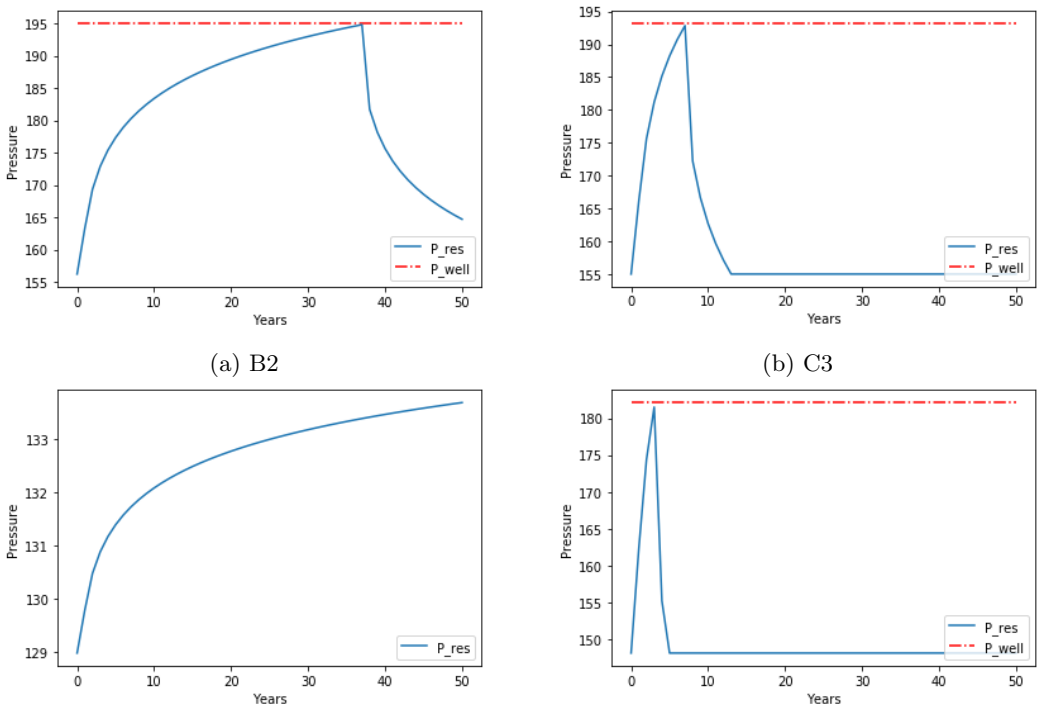


(a) B2

(b) C3

(c) B5

(d) C4

Figure 19: Compartment pressure over 50 years for four selected compartments. The compartment pressure $P_{res}$ show a pressure increase in the compartments as $CO_2$ is injected from year 0. Injection stops if the compartment pressure reaches the final pressure (maximum well pressure), and the pressure then decays towards the initial pressure. $P_{well}$ indicates the maximum well pressure.

| | Mean depth (m) | P_init (bar) | P_well (bar) | Total pore volume (m^3) | A | Total storage mass (million tonnes) |
|---|---|---|---|---|---|---|
| B2 | 1529 | 156 | 195 | 7285958970 | 17,5 | 3,97 |
| C3 | 1518 | 155 | 193 | 4663100400 | 27,4 | 1,27 |
| B5 | 1262 | 129 | 153 | 16924470075 | 2 | 12,08 |
| C4 | 1449 | 148 | 182 | 2551332575 | 35,1 | 0,72 |

Figure 20: Table with the results from the calculations, where the pressure analysis approach is applied to the four compartments.

Figure 19 presents plots of compartment pressure over a time period of 50 years. One can start of by considering (a), being compartment B2. The pressure at year 0 is equal to the initial pressure of the compartment ($P_{init}$ = 156 bar), calculated as presented in Section 6.2.1. As injection is started, the pressure increases following the pressure function of Figure 13. The maximum well pressure, also calculated in Section 6.2.1, indicates the maximum pressure of the compartment, and the injection is stopped after this pressure is reached, here at $P_{well}$ = 195 bar, reached in year 37. At this point, the pressure starts decaying, where the decay function mirrors the increase function towards the initial pressure. The pressure does not reach the initial pressure within the time period of 50 years. Within the 37 years of injection, a total storage mass of 3,97 million tonnes of $CO_2$ is stored in the compartment. A summary of the initial values and results calculated are presented in the table of Figure 20.

Plot (b) of Figure 19 presents compartment C3. The initial pressure of this compartment is at 155 bar, and the maximum well pressure at 193 bar, which is reached after few years of injection. In these years 1,27 million tonnes of $CO_2$ is stored in the compartment. One can see that the initial pressure is reached in year 12 and the pressure stabilizes.

Figure 19 (c) show compartment B5, which is a quite unique case. One can here see a case where the maximum well pressure of 153 bar is not reached. This means that the injection goes on for all 50 years, and yet does not reach the maximum pressure. This results in a total storage mass of 12,08 million tonnes of $CO_2$.

The last compartment presented in Figure 19 is C4, plot (d). This case displays the pressure behavior for a comparatively small compartment (see total pore volumes Figure 20), where the pressure increases and reaches the well pressure of 182 bar rapidly. The pressure decreases equally as rapid towards the initial pressure which is reached again already after 5 years of the injection start. The injection results in a total storage of 0,718 million tonnes of $CO_2$.

The results presented above are further discussed in Section 8.1.

## 7.2 The Compressibility Limit

When assessing the pressure management approach (Figure 13) one should separately evaluate the two approaches that this complex equation is composed of, being the left side of the equation (The box volume approach, Section 4.1) and the right side of the equation (The basin geo-pressure approach, Section 4.2).

If we focus on the left side of the equation, the box volume approach, this is a equation representing the relationship between the rock compressibility, rock volume, rock volumetric change and pressure change (See Equation 4). This simple box model can limit the allowable injection volume of a compartment, and should further work as a constraint on the injectivity equation (Equation 9). Take note that the box volume approach does not have a time dimension, and is a final, limiting value for the volumetric change of a box volume. The total injected volume can then be found through the injectivity equation integrated over the project lifetime, however the injection should stop if the total injection volume reaches the final, limiting volume change from the compressibility equation.

The script put together was used to test different compressibilities in addition to the set compressibility of $3 * 10^{-9}$, looking into at what point the different compartments reaches the constraint from the compressibility. An upper, middle and (extremely) low case of compressibilities were tested on the Sognefjord Fm., at $7 * 10^{-9}$, $3 * 10^{-9}$ and $5 * 10^{-12}$ $Pa^{-1}$ respectively.

The results show that the upper compressibility case of $7 * 10^{-9}$ $Pa^{-1}$ does not affect any of the compartments, as the volumetric constraint is larger than the total volume of $CO_2$ that is stored in each compartment within the injection period of 50 years. The middle compressibility case of $3 * 10^{-9}$ $Pa^{-1}$ is a little lower, and arguably the most realistic reservoir compressibility. This case restricts only one compartment over the 50 years of injection (concerning all three formations), being the smallest compartment of all scenarios, D7 (See Appendix D). As a reference, this compartment is about ten times as small as the second smallest compartment. For this

compressibility case the constraint of volumetric change is at 290 000 $m^3$ and the compartment reaches the constraint in the first year of injection.

As to experiment, an extreme low compressibility case is also assessed, as to see how low the compressibility should be for the compressibility to be the limiting factor of a storage project such as Smeaheia. This low compressibility case of $5 * 10^{-12}\ Pa^{-1}$ works as a limiting factor on all compartments within short time. For instance one can consider the largest compartment B5, which reaches the compressibility constraint of 430 000 $m^3$ in the second year of injection. The results are further discussed in Section 8.2.

## 7.3 The $\Delta P$ limit

As the compressibility is considered a constraining factor on the injectivity equation, one should further also consider the possibility of the pressure change, $\Delta P$ of the same equation (Equation 4) constructing a constraint on the storage capacity of the compartments.

For initial calculations and testing of the compressibility limit $\Delta P$ was set to 5 MPa as a guideline maximum pressure. But when will $\Delta P$ be a limiting factor? The $\Delta P$ distribution range selected in Section 6.3 was tested on the Sognefjord Fm, by setting the compressibility back as a set parameter of $3 * 10^{-9}\ Pa^{-1}$.

The three cases give similar results. All three cases constrain only D7, the very smallest compartment. The lower bound case of $\Delta P\ = 1MPa$ naturally sets the lowest bound of constraints on the compartments. As an example, we can consider the second smallest compartment, D6. The lower bound pressure case sets a constraint on D6 at 550 000 $m^3$. However, this compartment reaches the maximum well pressure already in the first year of injection, and only experiences a volumetric change of 210 000 $m^3$ until this. With this, the pressure limits from $\Delta P$ does not constrain other compartments than D7 for the three tested cases. The results are further discussed in Section 8.3.

## 7.4 Storage capacity

The pressure approach can further be used to consider the storage capacity of the three scenarios. As mentioned, the thought is to inject $CO_2$ separately into each compartment, with one well per compartment, which further imply applying the pressure approach of Figure 13 to each single compartment.

By utilizing the script put together on the compartment data, a storage capacity was found for each compartment, in terms of how big of an injected volume each compartment could allow. One can with this add up all compartments of each scenario to consider each scenario as a whole. As to compare the scenarios, the results are presented in total pore volume $km^3$, where the objective can be considered to maximise the total pore volume of a scenario, meaning a higher mass of $CO_2$ can be stored.

The results in this section is presented in volume [$km^3$], which might not seem the most relevant unit when assessing $CO_2$ storage. However, maximising available pore volume is equivalent to maximising mass of $CO_2$ that can be stored. Conversions to mass are done on the total pore volumes calculated of each scenario, presented in Figure 27.

The scenarios are compared by considering the hierarchy of the compartments, as presented in Figure 16. As to present this in a simple way, separate tables (Figures 21 - 26 ) are presented, focusing on smaller, selected areas. Take note that volumes are presented per formation layer, as one consider sealed boundaries between the Sognefjord, Fensfjord and Krossfjord formations. The available pore volume of a compartment in each formation is presented, as well as the total sum of the three formations. For instance, compartment B1 is presented in Figure 21, considering the study area as one big compartment. By considering the hierarchy, one sees that Scenario C in the same area consists of two compartments, being C1 and C2, and Scenario D consisting of 3 compartments in this area, being D1, D2, and, D3. The results are shown in Figures 21 - 26 for

each of the three scenarios. A short summary of the results are presented below, before further evaluated and discussed in Section 8.4.

Figure 21 shows the case of B1, being evaluated as one big (B), two smaller (C), or three even smaller (D) compartments. The results (total available pore volume) shows that scenario D consisting of three compartments can store the most $CO_2$, in fact over twice as much as for scenario B, being only one big compartment.

Figure 22 show somewhat different results from the B1 case. The one big (B) compartment is the option that will bring out the largest total storage volume. However, one sees that scenario D consisting of 4 small compartments will bring out a larger total storage volume than scenario C being two compartments.

Figure 23 show that scenarios C and D store the most, in fact the same, as the compartment scenarios are identical. They both consider two smaller compartments, and the result is that they can store around twice as much as one bigger compartment (B) would.

Figure 24 show that Scenario D of 5 compartments accommodate a significantly larger storage volume than Scenario C of 2 compartments and Scenario B of one big compartment.

Figure 25 can be considered a special case, and as one can see Scenario B brings out the largest total pore volume, being almost twice as large as for scenarios C and D. One can also note that Scenario C of 2 compartments store more than Scenario D of 5 compartments. Recall that the case of B5 was a special case in terms of the selected scaling parameter A, as seen in Section 7.1.

Figure 26 also shows a somewhat special case. Scenario B is also here the better scenario, and the second best is Scenario D of 5 compartments. The scenario of the smallest total pore volume available is Scenario C.

A summation of the results from each study area is presented in Figure 27. Two different tables are presented, one of the entire study area, and one without the B5 area, being the compartments presented in Figure 25. The reason for this will be further discussed in Section 8.4.

The left side table of Figure 27 show that Scenario B (see Appendix B) will bring out the largest total pore volume (0,117 $km^3$) , and followingly store the highest mass of $CO_2$ (92,6 Mt). The right table sums up the total storage volumes, excluding the B5 area of each scenario. This results in Scenario D (Appendix D) bringing out the largest total pore volume (0,066 $km^3$), and storing the highest mass of $CO_2$ (52,01 Mt). The results are discussed in Section 8.4.

**Total storage Volume (km^3)**

| | B1 | | |
|---|---|---|---|
| Sognefjord Fm. | 0,0004249 | | |
| Fensfjord Fm. | 0,0005409 | | |
| Krossfjord Fm. | 0,0007331 | | |
| Total | **0,0016988** | | |
| | **C1** | | **C2** |
| Sognefjord Fm. | 0,0004086 | | 0,0002172 |
| Fensfjord Fm. | 0,0005188 | | 0,0002579 |
| Krossfjord Fm. | 0,0006609 | | 0,0003423 |
| Total | **0,0024057** | | |
| | **D1** | **D2** | **D3** |
| Sognefjord Fm. | 0,0004609 | 0,0003120 | 0,0002172 |
| Fensfjord Fm. | 0,0006100 | 0,0004022 | 0,0002579 |
| Krossfjord Fm. | 0,0007658 | 0,0005152 | 0,0003423 |
| Total | **0,0038835** | | |

Figure 21: Total storage volume ($km^3$) of the three scenarios at the B1 area.

| Total storage Volume (km^3) | | | | |
|---|---|---|---|---|
| | B2 | | | |
| Sognefjord Fm. | 0,0050247 | | | |
| Fensfjord Fm. | 0,0083194 | | | |
| Krossfjord Fm. | 0,0121279 | | | |
| Total | **0,0254719** | | | |
| | C3 | | C4 | |
| Sognefjord Fm. | 0,0016069 | | 0,0009095 | |
| Fensfjord Fm. | 0,0021335 | | 0,0011567 | |
| Krossfjord Fm. | 0,0026927 | | 0,0015104 | |
| Total | **0,0100098** | | | |
| | D4 | D5 | D6 | D7 |
| Sognefjord Fm. | 0,0016069 | 0,0010439 | 0,0002166 | 0,0001257 |
| Fensfjord Fm. | 0,0021335 | 0,0014075 | 0,0002870 | 0,0001397 |
| Krossfjord Fm. | 0,0026927 | 0,0020049 | 0,0004196 | 0,0001295 |
| Total | **0,0122075** | | | |

Figure 22: Total storage volume ($km^3$) of the three scenarios at the B2 area.

| Total storage Volume (km^3) | | |
|---|---|---|
| | B3 | |
| Sognefjord Fm. | 0,0007689 | |
| Fensfjord Fm. | 0,0010340 | |
| Krossfjord Fm. | 0,0015116 | |
| Total | **0,0033145** | |
| | C5 | C6 |
| Sognefjord Fm. | 0,0007642 | 0,0008102 |
| Fensfjord Fm. | 0,0010539 | 0,0010425 |
| Krossfjord Fm. | 0,0015998 | 0,0015385 |
| Total | **0,0068091** | |
| | D8 | D9 |
| Sognefjord Fm. | 0,0007642 | 0,0008102 |
| Fensfjord Fm. | 0,0010539 | 0,0010425 |
| Krossfjord Fm. | 0,0015998 | 0,0015385 |
| Total | **0,0068091** | |

Figure 23: Total storage volume ($km^3$) of the three scenarios at the B3 area.

| Total storage Volume (km^3) | | | | | |
|---|---|---|---|---|---|
| | B4 | | | | |
| Sognefjord Fm. | 0,0012159 | | | | |
| Fensfjord Fm. | 0,0016849 | | | | |
| Krossfjord Fm. | 0,0027772 | | | | |
| Total | **0,0056779** | | | | |
| | C7 | C8 | | | |
| Sognefjord Fm. | 0,0007864 | 0,0012014 | | | |
| Fensfjord Fm. | 0,0010256 | 0,0016546 | | | |
| Krossfjord Fm. | 0,0014342 | 0,0026507 | | | |
| Total | **0,0087529** | | | | |
| | D10 | D11 | D12 | D13 | D14 |
| Sognefjord Fm. | 0,0007864 | 0,0008561 | 0,0010281 | 0,0016436 | 0,0014225 |
| Fensfjord Fm. | 0,0010256 | 0,0010884 | 0,0014036 | 0,0024844 | 0,0021677 |
| Krossfjord Fm. | 0,0014342 | 0,0016513 | 0,0021608 | 0,0041719 | 0,0036007 |
| Total | **0,0269252** | | | | |

Figure 24: Total storage volume ($km^3$) of the three scenarios at the B4 area

| Total storage Volume (km^3) | | | | | |
|---|---|---|---|---|---|
| | B5 | | | | |
| Sognefjord Fm. | 0,0152854 | | | | |
| Fensfjord Fm. | 0,0199288 | | | | |
| Krossfjord Fm. | 0,0252661 | | | | |
| Total | **0,0604803** | | | | |
| | C9 | | C10 | | |
| Sognefjord Fm. | 0,0017578 | | 0,0021765 | | |
| Fensfjord Fm. | 0,0046095 | | 0,0035094 | | |
| Krossfjord Fm. | 0,0093239 | | 0,0072159 | | |
| Total | **0,0285930** | | | | |
| | D15 | D16 | D17 | D18 | D19 |
| Sognefjord Fm. | 0,0030546 | 0,0002809 | 0,0006751 | 0,0006629 | 0,0008608 |
| Fensfjord Fm. | 0,0032285 | 0,0004274 | 0,0010196 | 0,0008901 | 0,0010471 |
| Krossfjord Fm. | 0,0102869 | 0,0005983 | 0,0016769 | 0,0012926 | 0,0014863 |
| Total | **0,0274879** | | | | |

Figure 25: Total storage volume ($km^3$) of the three scenarios at the B5 area

| Total storage Volume (km^3) | | | | | |
|---|---|---|---|---|---|
| | B6 | | | | |
| Sognefjord Fm. | 0,0027547 | | | | |
| Fensfjord Fm. | 0,0056031 | | | | |
| Krossfjord Fm. | 0,0122157 | | | | |
| Total | **0,0205735** | | | | |
| | C11 | | C12 | | |
| Sognefjord Fm. | 0,0009125 | | 0,0008915 | | |
| Fensfjord Fm. | 0,0013683 | | 0,0014926 | | |
| Krossfjord Fm. | 0,0021686 | | 0,0025519 | | |
| Total | **0,0093854** | | | | |
| | D20 | D21 | D22 | D23 | D24 |
| Sognefjord Fm. | 0,0006894 | 0,0009402 | 0,0005899 | 0,0005355 | 0,0006000 |
| Fensfjord Fm. | 0,0010404 | 0,0013162 | 0,0008862 | 0,0007805 | 0,0008611 |
| Krossfjord Fm. | 0,0016525 | 0,0021970 | 0,0013705 | 0,0011914 | 0,0013615 |
| Total | **0,0160122** | | | | |

Figure 26: Total storage volume ($km^3$) of the three scenarios at the B6 area

**Sum Compartments**

| Total Storage Volume (km^3) | Total Storage Mass (Mt) |
|---|---|
| B | |
| 0,1172170 | 92,60146518 |
| C | |
| 0,0659559 | 52,10514544 |
| D | |
| 0,0933254 | 73,72708661 |

**Sum Compartments without B5 area**

| Total Storage Volume (km^3) | Total Storage Mass (Mt) |
|---|---|
| B | |
| 0,0567367 | 44,82201434 |
| C | |
| 0,0373629 | 29,5166649 |
| D | |
| 0,0658375 | 52,01164247 |

Figure 27: Sum of the total storage volume and mass for the three scenarios. The table to the left sums up volumes from all compartments. The right table subtracts the B5 area, being the compartments presented in Figure 25.

## 7.5 Sensitivity

As to assess the sensitivity of variation in parameter distributions a sensitivity analysis was carried out. The sensitivity of output parameters was evaluated through tornado plots, where a high and low value was set for each parameter, as the upper and lower bound of the parameter distributions from Section 6.3. The results shows how the variety in parameters variate the total storage mass possible to store in a compartment. Three compartments of different sizes and characteristics were selected to be presented in this section; one large compartment (B2) that reaches the compressibility constraint with its middle values, a medium sized compartment (B4) that reaches very close to the compressibility constraint with its middle values, and a small compartment (D6) where the compressibility limit is not reached.

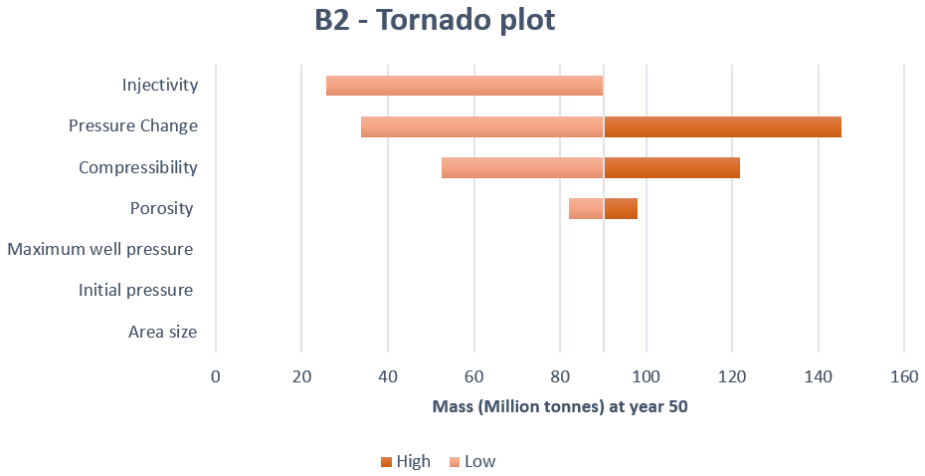


Figure 28: Tornado plot for compartment B2. This is a comparatively large compartment. The low bound injectivity index is an overwhelming driver, whereas the high bound injectivity has a negligible impact. Factors such as pressure change, compressibility, and porosity also affect the total storage mass significantly. Maximum well pressure, initial pressure and area size has little to no impact on the output.

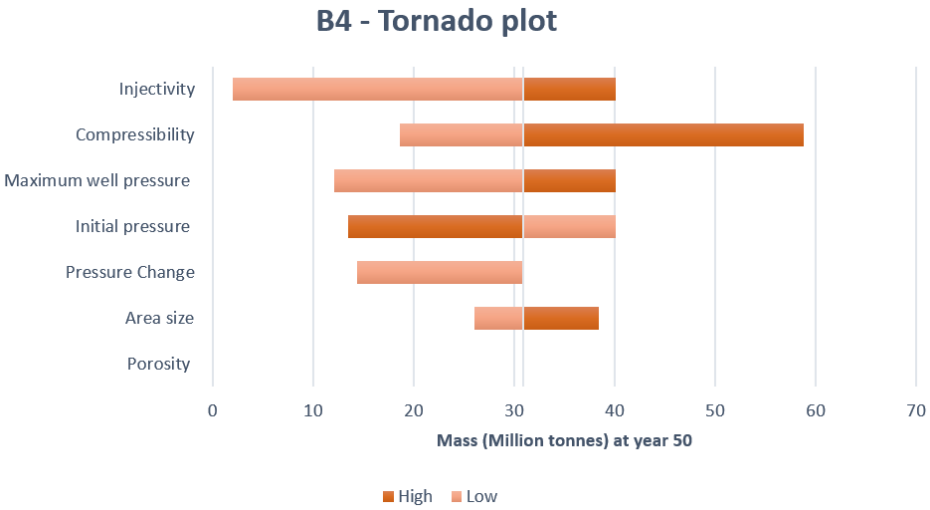


Figure 29: Tornado plot for compartment B4. This is a medium sized compartment. Injectivity is a overwhelming driver for this compartment. Additionally, the compressibility, maximum well pressure, initial pressure, pressure change, and area size all affect the total storage mass. Porosity has little to no impact on the output.

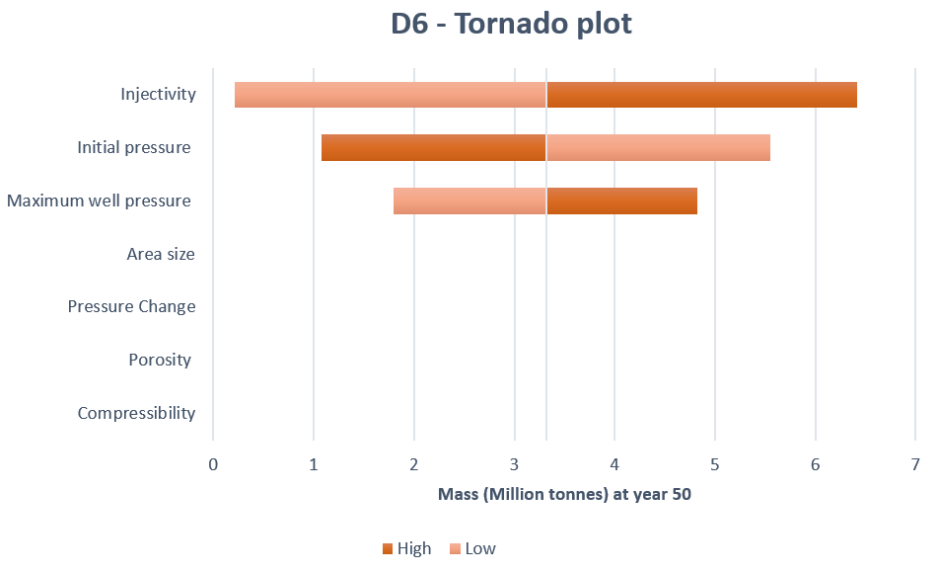


Figure 30: Tornado plot for compartment D6. This is a rather small compartment. The injectivity index has the greatest impact, followed by the initial pressure and maximum well pressure. The remaining parameters have little to no impact on the output.

Ranges for Tornado Plots

| | Low Bound | High Bound | Middle Value |
|---|---|---|---|
| **B2 - year 50** | | | |
| Porosity | 0.27 | 0.32 | 0.295 |
| Compressibility (Pa^-1) | 0.000000003 | 0.000000007 | 0.000000005 |
| Pressure Change (Pa) | 1000000 | 5000000 | 3000000 |
| Injectivity (m^3/day/bar) | 50 | 1500 | 775 |
| Maximum well pressure (bar) | 184.12 | 205.78 | 194.95 |
| Initial pressure (bar) | 146.21 | 166.21 | 156.21 |
| Area size (m^2) | 220.28 | 224.73 | 222.50 |
| | | | |
| **B4 - year 50** | | | |
| Porosity | 0.27 | 0.32 | 0.295 |
| Compressibility (Pa^-1) | 0.000000003 | 0.000000007 | 0.000000005 |
| Pressure Change (Pa) | 1000000 | 5000000 | 3000000 |
| Injectivity (m^3/day/bar) | 50 | 1500 | 775 |
| Maximum well pressure (bar) | 179.41 | 200.50 | 189.96 |
| Initial pressure (bar) | 143.06 | 163.06 | 153.06 |
| Area size (m^2) | 106.19 | 108.33 | 107.26 |
| | | | |
| **D6 - year 50** | | | |
| Porosity | 0.27 | 0.32 | 0.295 |
| Compressibility (Pa^-1) | 0.000000003 | 0.000000007 | 0.000000005 |
| Pressure Change (Pa) | 1000000 | 5000000 | 3000000 |
| Injectivity (m^3/day/bar) | 50 | 1500 | 775 |
| Maximum well pressure (bar) | 115.14 | 128.69 | 121.91 |
| Initial pressure (bar) | 97.08 | 117.08 | 107.08 |
| Area size (m^2) | 2.84 | 3.47 | 3.15 |

Figure 31: Table of the parameter distributions utilized for the Tornado Plots. Each input parameter has a middle value, found as an average between an upper and lower bound of the distributions.

Figure 28 displays compartment B2 in the Sognefjord Fm. As has been seen this is a comparatively large compartment, and results show a middle value of 90.06 Mt stored $CO_2$ at year 50. Take not that this section displays rather large numbers compared to earlier results, as new parameters are selected for this and following sections (in Section 6.3). Especially the injectivity index will result in higher total storage masses. The middle value of each parameter (Figure 31) is applied, and this middle output mass is indicated with the 'centering line' in the tornado plots. One can further see that the low bound injectivity index is the variable of the highest impact. The high bound injectivity index has no impact on the mass. The second most overwhelming driver is the pressure change $\Delta P$, followed by the compressibility and lastly porosity. For all three parameters one can see that the higher bound value results in the higher storage mass, and the lower bound value results in a lower total storage mass. Maximum well pressure, initial pressure and area size are of negligible impact on the total storage mass of compartment B2.

The next tornado plot is presented in Figure 29, displaying compartment B4. The middle values for this compartment shows 30,93 Mt of stored $CO_2$. One can observe that the plot looks quite different from the tornado plot of compartment B2. The injectivity index is yet the overwhelming driver. The second overwhelming driver is the compressibility, followed by maximum well pressure and initial pressure. For the initial pressure the results are flipped. Following this comes the pressure change and area size, while the porosity is of no impact on the total storage mass.

The last compartment to be assessed in terms of sensitivity is compartment D6, depicted in Figure 30. This is the second smallest of all compartments, and the total storage mass from the middle values show 3,315 Mt of $CO_2$. One can see that the injectivity index is still an overwhelming factor. The factor of the second highest impact on this smaller compartment is the initial pressure, where the lower bound result in the higher storage mass. Following this is the maximum well pressure, where a higher pressure results in a higher storage mass. All other parameters are negligible for this compartment.

The three compartments show three quite different tornado plots. The selected middle value, with the upper and lower bounds for the three compartments are presented in Figure 31. Several of the parameter distributions are selected in Section 6.3, such as porosity, compressibility, pressure change, and injectivity index. The maximum well pressure range is found by setting the low bound to 85% of the fracture pressure and the high bound to 95% of the fracture pressure of the compartment rock. The initial pressure is ranged with 10 bar, and the area size is ranged with 10% to account for uncertainties. The tornado plots show some clear similarities, but also differences in which parameters result in the highest impact on the total storage mass of the compartments. The results are further discussed is Section 8.5.

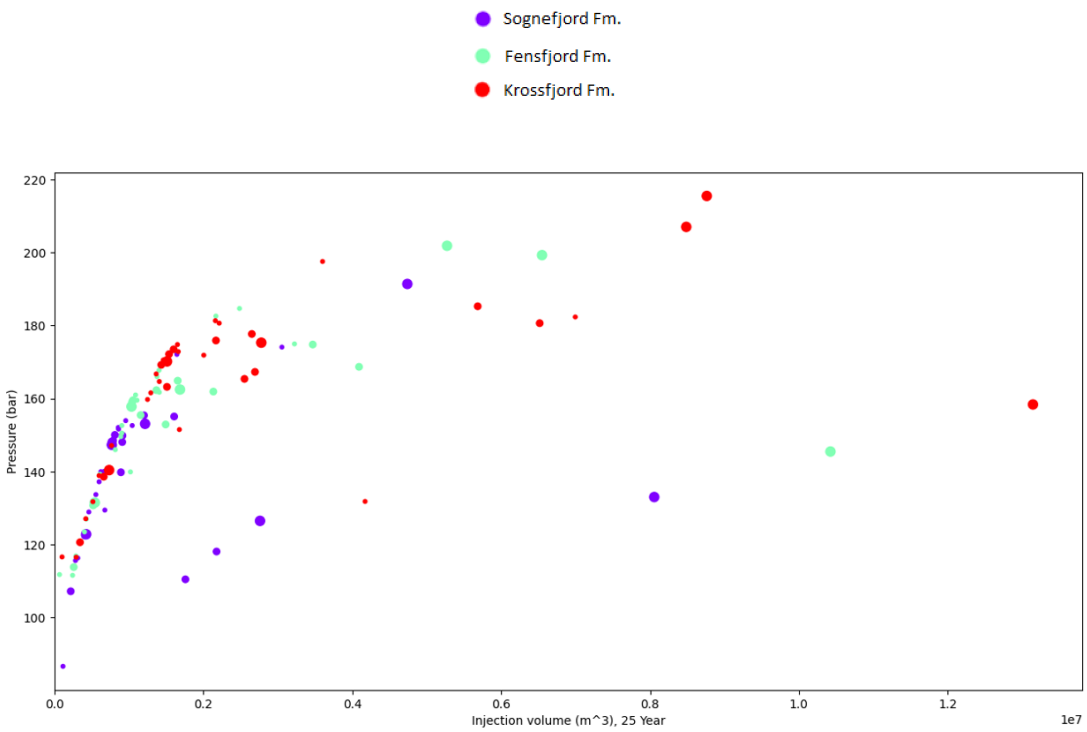


Figure 32: Compartment pressure versus total stored volume for all compartments at 25 years of injection with set parameters. The point size illustrates the scenario, and the color illustrates formation of the compartment.

## 7.6 Distributions and Sampling

### 7.6.1 Data with Set Parameters

As the reservoir pressure, total storage volume and masses are calculated with set parameters for all compartment in Section 7.4, a large number of outcomes are constructed. It is further interesting to analyse these clouds of data.

Figure 32 plots compartment pressure versus injected volume for all compartments after 25 years of injection. The point color illustrates the formation that the compartment is placed in, being either the Sognefjord, Fensfjord or Krossfjord Fm. The size of the point illustrates the scenario, where the bigger points are Scenario B, medium points Scenario C, and the smallest points Scenario D. The plot illustrates a log-linear relationship between the compartment pressure and the injected volume. As to further illustrate results, a log-linear model was applied to the data. For instance, Figure 33 illustrates the same data as Figure 32, with a log-linear model applied (see x-axis).

Figure 34 show similar data, being at year 50 of injection. Some compartments experience an increase in pressure and injected volume within the 25 year gap between the two plots, while some compartments are decreasing in pressure towards their initial pressure, where there is no change in injection volume. Most compartments stay more or less the same from year 25 to 50.

### 7.6.2 Data with Parameter Distributions and Uncertainty

As initial calculations of set parameters are presented, one can further consider ranging input parameters and distributions, as found in Section 6.3. Figures 35 and 36 show cases where the distributions are applied to the compartments, plotting pressure versus total injected $CO_2$ mass for year 25 and 50 respectively. The results presented are further evaluated in Section 8.6.

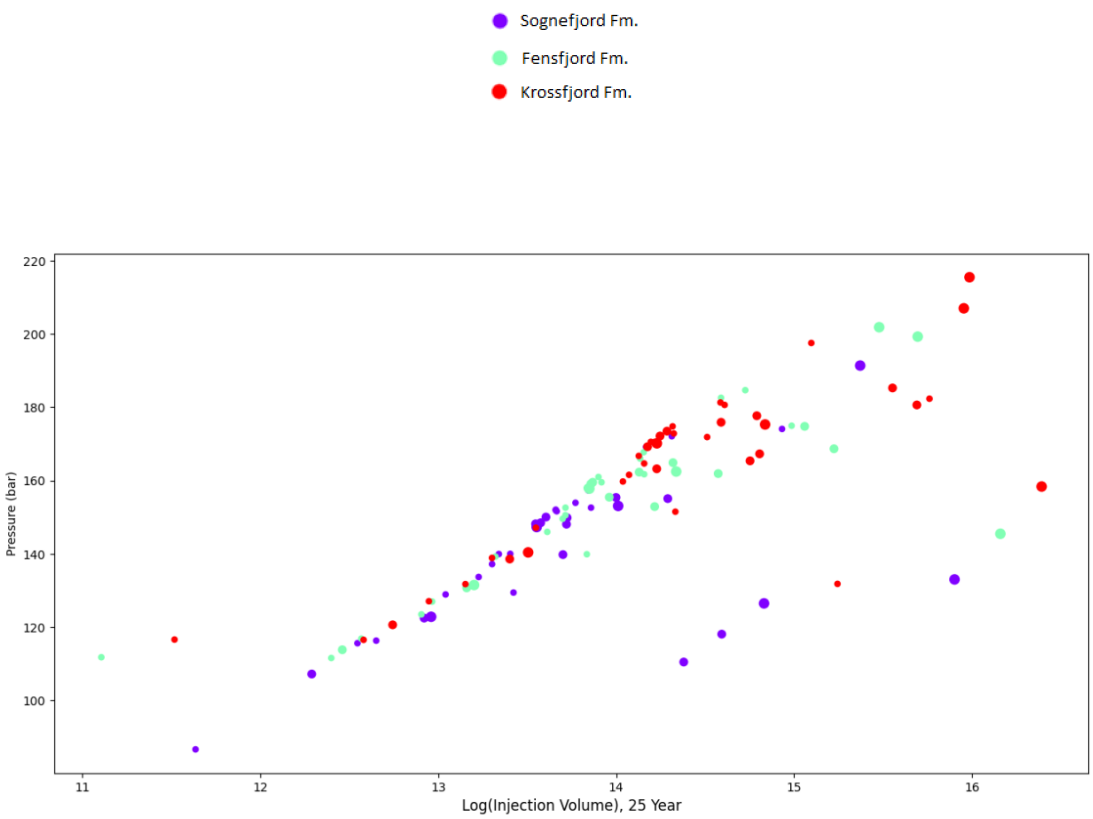


Figure 33: Compartment pressure versus total stored volume for all compartments at 25 years of injection with set parameters. The point size illustrates the scenario, and the color illustrates formation of the compartment. The x-axis is logarithmic.

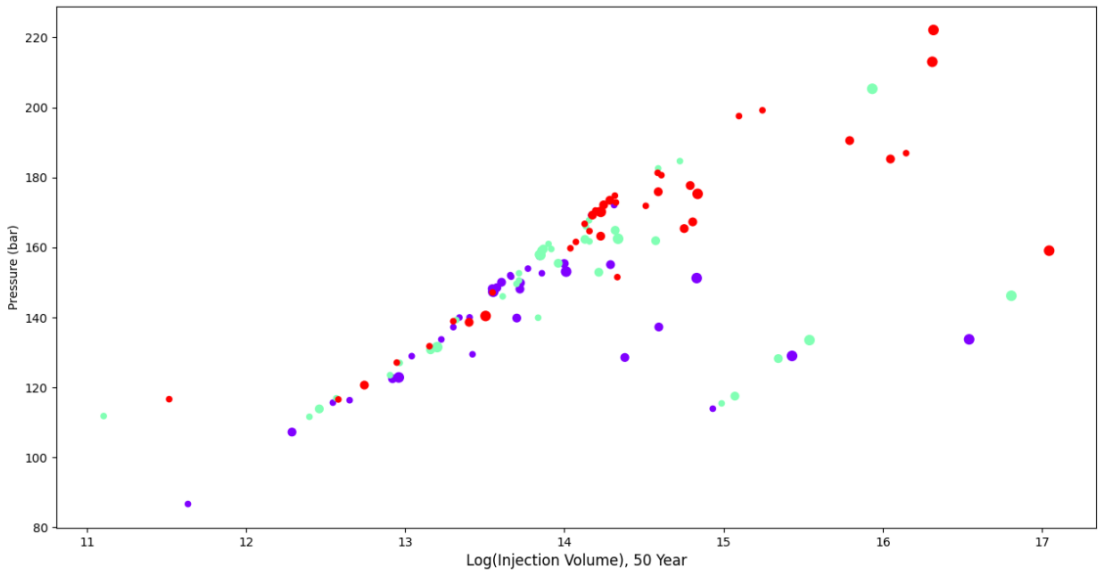


Figure 34: Compartment pressure versus total stored volume for all compartments at 50 years of injection with set parameters. The point size illustrates the scenario, and the color illustrates formation of the compartment. The x-axis is logarithmic.

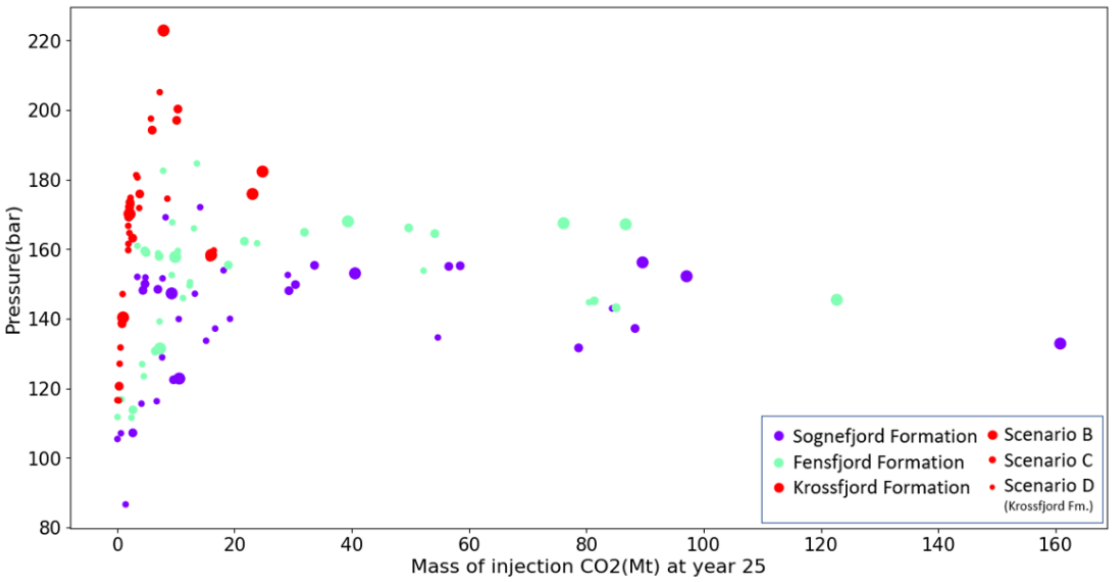


Figure 35: Compartment pressure versus total stored $CO_2$ mass for all compartments at 25 years of injection with parameter distributions. The point size illustrates the scenario, and the color illustrates the formation the compartment is placed in.

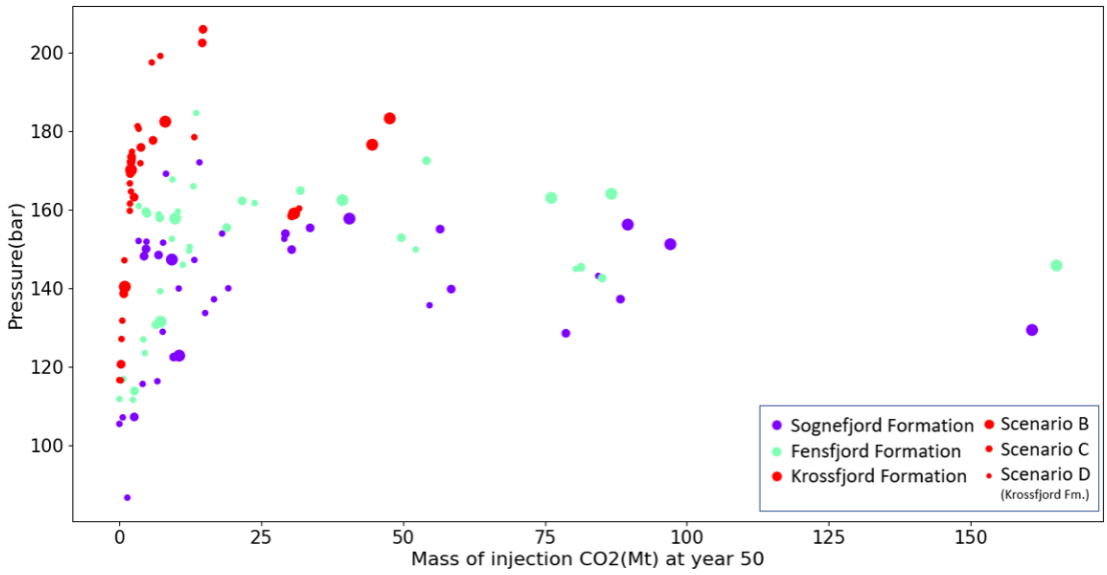


Figure 36: Compartment pressure versus total stored $CO_2$ mass for all compartments at 50 years of injection with parameter distributions. The point size illustrates the scenario, and the color illustrates the formation the compartment is placed in.

## 7.7 Principal Component Analysis

A large number of outcomes was produced from applying parameter distributions to the compartments, and a cloud of data was constructed. As Figure 35 and 36 presents the data plotted as compartment pressure versus total injected mass, one can further analyse the data through multivariate statistical techniques, such as principal component analysis as to consider more of the many variables related each compartment.

The data previously constructed is retained in data tables. The input and output parameters from applying the approach are gathered for each compartment of each formation, adding up to 126 compartments.

Principal component analysis was carried out on the data, and some initial results are included in this section.

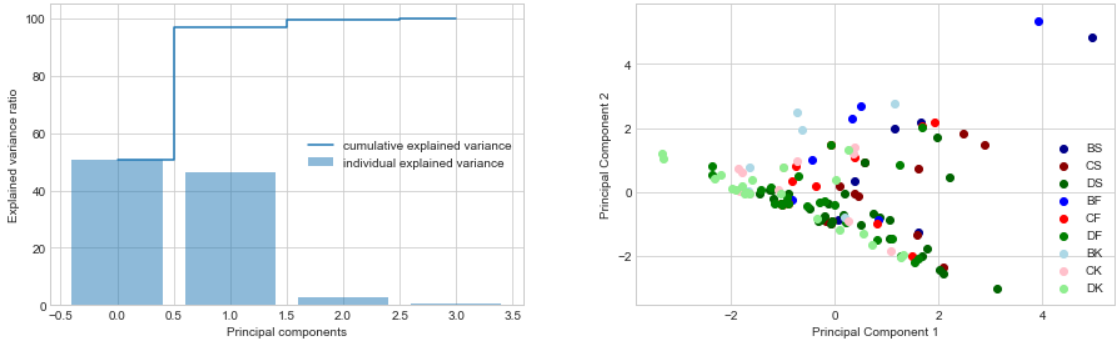


(a) (b)

Figure 37: (a) Scree plot depicting the variance proportion for each of the four principal components. The blue line presents the cumulative proportion of explained variance by the components. (b) Final graph, based on principal component 1 and 2. Labels B, C,and D represents the scenario of the compartment, and S, F, and K represents the formation Sognefjord, Fensfjord and Krossfjord respectively. The original parameters considered are total storage volume, initial pressure, maximum well pressure, and total injected volume.

The first example case study four parameters, being total storage volume, initial pressure, maximum well pressure, and total injected volume for each compartment. This information is further expressed through a set of new orthogonal variables, principle components.

A PCA extracts four factors with the following eigenvalues:

$$\text{Eigenvalues Case 1} = \begin{bmatrix} 1.84903706 & 2.02233707 & 0.10230161 & 0.02632426 \end{bmatrix}$$

The first two components are $> 1$, and will be selected as principal component 1 and 2. The explained variance plot (scree plot) of Figure 37 (a) shows that around 50 % of the variance can be explained by the first principal component alone. The second principal component also bears information, at around 45 % of the total inertia. Together, the two principal components contain almost all variance, at $> 95\%$. The third and fourth principal component can safely be dropped without too much information being lost. Both the principal components have eigenvalues $> 1$.

The samples are further projected onto the new feature subspace using the two principal components. The result is illustrated in Figure 37 (b). The next step is the interpretation of the PCA. Recall from Section 5.3 that the importance of the components are reflected by its inertia. One can from this gather that principal component 1 is the most important, however component 2 is also important as it has a high variance. One can study the eigenvectors of the components as to interpret the results.

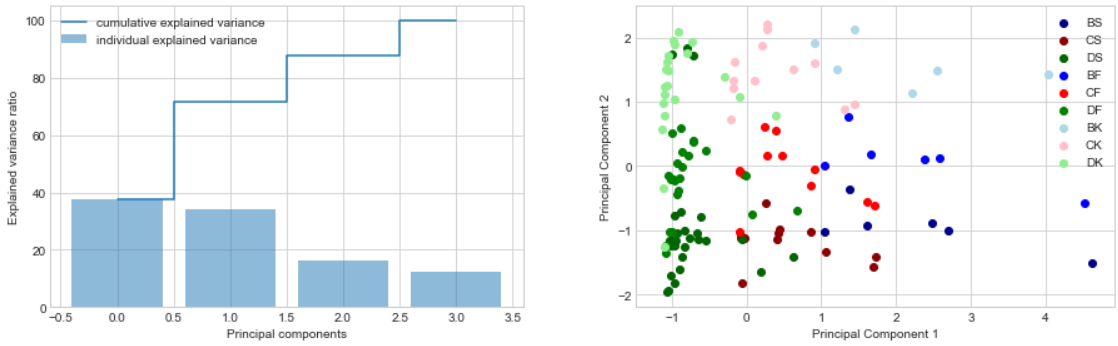


(a) (b)

Figure 38: (a) Scree plot depicting the variance proportion for each of the four principal components. The blue line presents the cumulative proportion of explained variance by the components. (b) Final graph, based on principal component 1 and 2. Labels B, C,and D represents the scenario of the compartment, and S, F, and K represents the formation Sognefjord, Fensfjord and Krossfjord respectively. The original parameters considered are total storage volume/injected volume ratio, difference between initial pressure and maximum well pressure, total injected volume, and injectivity index.

$$\text{Eigenvectors Case 1} = \begin{bmatrix} 0.62071423 & -0.34283937 & 0.69596296 & -0.11318384 \\ 0.37943902 & 0.59615358 & -0.1569431 & -0.68992449 \\ 0.35992051 & 0.60760962 & 0.09246588 & 0.70193863 \\ 0.5841208 & -0.39733189 & -0.69458944 & 0.13592563 \end{bmatrix}$$

The matrix above reveals that the first principle component (second column) is highly dependent on the initial pressure and maximum well pressure. The second principal component (first column) seems to be heavily dependent on total storage volume and total injected volume of the compartment.

The second case study four different parameters, being the ratio between total volume and total injected volume, pressure difference between the initial pressure and maximum well pressure, the total storage volume, and the injectivity index of each compartment. The eigenvalues show that the third and fourth factor have values $> 1$:

$$\text{Eigenvalues Case 2} = \begin{bmatrix} 0.642224 & 0.49019753 & 1.36616608 & 1.5014124 \end{bmatrix}$$

The explained variance plot is presented in Figure 38 (a), showing a lower variance of the two first principle components compared to Case 1. The two components will cover a variance of around 70%. In Figure 38 (b) the samples are projected onto the new feature space using the principal components. The eigenvalues are presented below:

$$\text{Eigenvectors Case 2} = \begin{bmatrix} 0.69031554 & -0.15629801 & 0.70528703 & 0.04006987 \\ 0.709719 & -0.04215316 & -0.70300804 & -0.01737093 \\ 0.08760637 & 0.69944123 & 0.02899161 & 0.70870768 \\ -0.10994784 & -0.69611493 & -0.0866567 & 0.70414919 \end{bmatrix}$$

This Matrix shows that the first principle component (fourth column) is positively associated with the total volume and injectivity. The second principal component (third column) is positively associated with the volume ratio and negatively associated with the pressure difference.

A third case is presented, in Figure 39. This case is quite similar to the second case, however the injectivity index parameter is switched out for the initial pressure. One can see that this gives a higher variance for the first principal component, and an overall higher inertia, at almost 80% (Figure 39 (a)). The eigenvalues reveal that the first and fourth factors have values $> 1$:

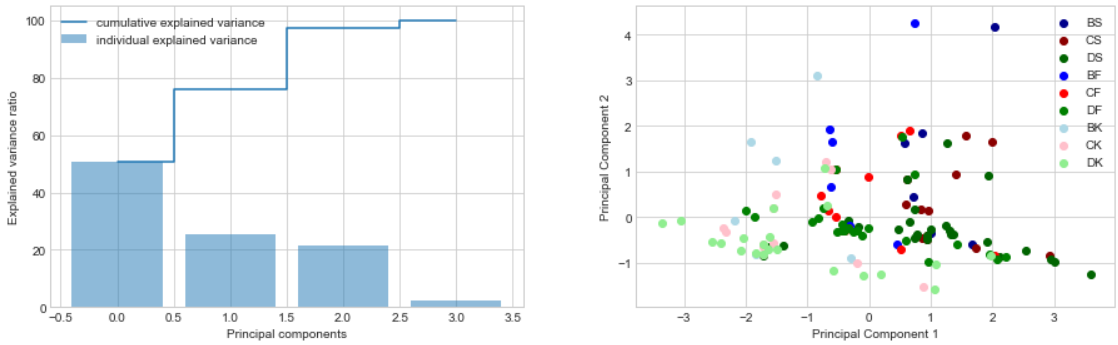


(a) (b)

Figure 39: (a) Scree plot depicting the variance proportion for each of the four principal components. The blue line presents the cumulative proportion of explained variance by the components. (b) Final graph, based on principal component 1 and 2. Labels B, C,and D represents the scenario of the compartment, and S, F, and K represents the formation Sognefjord, Fensfjord and Krossfjord respectively. The original parameters considered are total storage volume/injected volume ratio, difference between initial pressure and maximum well pressure, total injected volume, and initial pressure.

$$\text{Eigenvalues Case 3} = \begin{bmatrix} 2.02102205 & 0.09844641 & 0.86034029 & 1.02019125 \end{bmatrix}$$

By studying the matrix of eigenvectors one can further see that the first principal component (first column) is strongly, negatively dependent on pressure difference and the initial pressure of the compartment, whereas the second principal component (fourth column) seems to be strongly, negatively dependent on the total injection volume of the compartment. The result is presented in Figure 39 (b)

$$\text{Eigenvectors Case 3} = \begin{bmatrix} 0.35021325 & -0.15841081 & -0.86575085 & -0.32051858 \\ -0.67939373 & -0.72141768 & -0.12340893 & -0.05244919 \\ 0.02469155 & -0.01674183 & 0.35848839 & -0.9330574 \\ -0.64433311 & 0.67393045 & -0.3266983 & -0.15466353 \end{bmatrix}$$

The results of the three cases are discussed in Section 8.7.

# 8 Discussion

## 8.1 Some Example Calculations with Set Parameters

The first set of results (Section 7.1) illustrated some example calculations with set parameters as to get a simple review and understanding of concepts.

We can start of by comparing the two cases of B2 (a) and C3 (b) of Figure 19. What is interesting about these compartment is that one can see by the scenario hierarchy (Figure 16) that C3 is a branch of B2, meaning that it is in the same area. However, C3 is smaller, and only a part of the larger B2 compartment area. Both compartments located in the same area and formation layer imply they have very similar mean depths and consequently initial- and maximum well pressure. One can further question why these values are not identical. From Figure 20 one can see that C3 has both initial- and maximum well pressure around 1-2 bars lower than of B2. The reason for this is the small difference in mean depths, which are calculated from the thickness maps, which will give a small variety as the area of the compartments are not the same (Appendix E VS. H).

However, the pressure values are similar enough that the two compartments can be compared as to assess what differences happens in terms of the pressure behavior for different sized compartments with similar initial pressure conditions. One finding is that the larger compartment, B2 stores around three times as much $CO_2$ as C3 (mass), in spite of B2 not even being twice the size of C3. Another finding is that the pressure increase of the two compartments look quite different, even with similar initial and maximum pressure. One should then pose the question as to what is the reason for this.

Turning to the Basin geo-pressure approach (Equation 9), the solution can be found. This equation is the basis of the pressure calculations, and show how the pressure and total stored volume changes with time. The two compartments will have similar input values for initial- and well pressure, as well as equal values for the injectivity index and boundary condition flux. This leaves the term of the characteristic pressure function, which consists of a dimensionless pressure function (Equation 8) and the scaling parameter A. A is a parameter that affects the rate of the pressure increase, and likewise the decrease. This further implies that A determines how fast the function climb is. It was found that A is correlated to compartment area size (Section 6.2.2) and one can gather from the findings that A will climb faster for smaller compartments. This is perfectly consistent with with the two cases of B2 (a) and C3 (b) of Figure 19, where the smaller compartment C3 experiences a faster function climb than B2, as the value of A is larger (see table Figure 20).

One can further back up this finding by considering the case of C4. This is the smallest of the four presented compartments, and one can see that as it is a smaller compartment A is larger. The large A results in a rapid pressure increase and decrease. This compartment reaches the maximum well pressure rather fast, and within the injection period 0,72 million tonnes of $CO_2$ is stored. Compared to the other compartments, this is a low mass. However, one should consider that this is a much smaller compartment, and perhaps having many of these rapid injections in small compartments could be of favour. This will be evaluated and discussed further in Section 8.4.

The last case of the four compartments is B5. What is particular about this case is the size of the compartment. B5 is the largest of all compartments put together, and has a total pore volume of 16 924 470 075 $m^3$. As seen in Figure 19, this compartment does not reach the well pressure within the 50 years of injection, in spite of a rather low maximum well pressure at 153 bar. This is a shallow compartment, with a quite low mean depth. Both initial and well pressures are lower than the other presented compartments. The huge compartment area size results in a low value of A, further resulting in a slow pressure rise. The plot of Figure 19 shows how the compartment increases with only around 5 bars over the 50 year long injection period. The results show a total storage mass of 12,08 million tonnes of $CO_2$, however there are some concerns to consider. As mentioned, this compartment is significantly larger than the other compartments, and this posed some complications.

In Section 6.2.2 a function for the scaling parameter A was conceptualized, being dependent on compressibility and area size of the compartment. This is a rather simplistic approach that assumes

a linear relationship between A and area size. Presumably this is not the case. A good verification of this is the compartment of B5. By utilizing the A - area relationship found in Figure 18, large compartments such as B5 will obtain negative values of A. By further assessing the basin geo-pressure equation (Equation 9) one will see that negative values of A would not give valid results, as the storage volume would decrease while injecting. A short conclusion is here that the linear relationship found and used for A and area size is too simplistic, and will not work for the larger compartments. The relationship should be non-linear, and not reach negative values for the scaling parameter A. This is a parameter where one generally knows little, with very few cases of real data. The scaling parameter is a key parameter to the pressure optimization, and will for future development require deeper analysis.

As this study has based calculations and assessment on the above-mentioned, somewhat simplistic relationship, a solution to negative values of A is needed. A should decrease with increasing area size and compressibility, however never be a negative value. One should also take note that A would realistically also be influenced by other factors, such as the local permeability. A simple solution was sorted out, by setting all A values lower than 2 equal to 2. This resulted in the value of A = 2 for compartment B5, and followingly the total storage mass at 12,08 Mt $CO_2$. One should with this note the adjustment, and take it into consideration when assessing the total storage mass results. One could argue that this is too high of a value, and measures should be done to find a more accurate calculation of A.

A last observation to take note of from the results are the total storage masses obtained for the four compartments. The total storage mass ranges from 0,72-12,08 Mt of stored $CO_2$. One can observe that these are not too high amounts, which is simply related to the selected initial conditions, and especially the rather low injectivity index.

### 8.1.1 Conclusion

With the initial calculations presented it was found that the pressure behavior of a compartment is highly dependent on the compartment size, relating to the scaling parameter A. This further points the way to an interesting analysis as to consider optimal compartment sizes for maximizing storage capacity.

It was also found that the linear function conceptualized for the scaling parameter A is too simplistic, and likely does not construct a simple linear relationship with area size and compressibility. A simple solution was found for negative A values, however one should consider uncertainty for its relating results.

The scaling parameter A is a key parameter to the pressure management approach, and future development will require deeper analysis of the parameter.

## 8.2 The Compressibility limit

One can from the approach equations find that the box volume approach constructs a compressibility constraint on the injectivity equation. This is a final, limiting value for volumetric change possible for a fault compartment.

### 8.2.1 The Middle Case

As mentioned, typical reservoir compressibilities lie in the range of $3 - 70 * 10^{-10}\ Pa^{-1}$ and the middle case is selected as the more realistic, averaged alternative of the compressibility cases. This compressibility case restricted only one pressure compartment, the very smallest compartment of D7. This compartment has an area size of 349 208 $m^2$, further giving e.g. the compartment in the Sognefjord Fm. a total pore volume of 8 380 992 $m^3$. As this compartment size is restricted by the compressibility already in the first year of injection, one can argue that this is a problematic size for a fault compartment in terms of $CO_2$ injection. Again, one should take note that this is a very

small compartment (see Appendix D), and more of a special case in terms of the compartments put together for the scenarios. The compartment is small, and reaches the change in pore volume that is restricted by the compressibility of the rock, and should not be injected into after this. In addition to reaching the volume constrain from the compressibility, one can take note that the difference between the initial and well pressure is small, and that with pressure increase the pressure would reach the maximum pressure rather fast, regardless of the volume constraint from the compressibility.

The second smallest compartment does not reach the compressibility constrain, and this compressibility case is allover hardly a limiting factor when injecting into the compartments of scenarios B,C, and D.

### 8.2.2 The Upper Case

The upper compressibility case shows a case of the very upper bound of what one could expect for a real case of reservoir rock. What is interesting, is how this more generous compressibility affects our case for D7, which was the only compartment restricted in the middle case. The total pore volume and pressure change stay constant in the box volume approach equation (Equation 4), and a higher compressibility condition a higher total possible volumetric change (constraint). Followingly, the upper compressibility case does not restrict the injection of D7, as the maximum pressure is reached before the volumetric compressibility constraint is reached. As mentioned, the difference in pressure between the initial pressure and maximum well pressure is small for this compartment, at only 15 bar (for compartment of the Sognefjord Fm.), resulting in the maximum pressure being reached short after injection start. This is in fact a very interesting result. Even if the upper compressibility case is generous, it is realistic, and it shows that the compressibility constraint is not even a limiting factor for very small fault compartments with total pore volumes below 10 000 000 $m^3$.

An interesting aspect to assess when evaluating these different compressibility cases is how this affects the scaling parameter A in the right side of the equation. The relationship between A and area size was addressed in Section 8.1. However, A is also related the compressibility. As seen in Figure 18, different compressibilities give different functions for A, which will again affect the injectivity equation when injecting $CO_2$ into the compartments. However, at this point we are dealing with very small area sizes, and one can further notice that this results in very small changes in A for the different compressibility cases.

A find in this is that a smaller compartment size will both lower the volume constraint from the compressibility and increase the rate of injected volume (through A), conditioning a smaller window of injection before the constraint is reached, working from both sides of the equation. However, this upper compressibility case does not affect any of the scenario compartments and should not be considered a limiting factor.

Going back to our compartment case of D7, the change in compressibility between the upper and middle case changes the value of A from 44,5 to 44,6, which can be considered to not affect the pressure changes in a significant way. The change of the two compressibility cases changes the value of A more significantly for bigger compartments, but never in a way that the volumetric compressibility limit is reached.

### 8.2.3 The (extremely) Low Case

The low compressibility case was put together more as a curiosity as to how the compartments would be affected. Take note that this compressibility value is not a realistic value for a porous reservoir such as Smeaheia. However, the results are interesting. It shows that compressibility can be the limiting factor to the injection as long as it is small enough. This compressibility case limits the volumetric change in all compartments of all scenarios. By studying Equation 4 of the box volume approach, one can draw the simple connection that lower compressibility $C_b$ leads to a smaller volumetric constraint $\Delta V_b$ and naturally selecting a low enough compressibility

will limit any compartment size. As the volume constraint from the compressibility becomes significantly low, one should also consider how the right side of the equation is affected. As seen, a lower compressibility condition a higher value of A. As a comparison the A value of B6 is for this compressibility at 42,4 which is more than twice the A of the same compartment in the upper compressibility case. This further implies that the rate of injection in the right side of the equation becomes significantly higher, and the constraint is reached faster. This low compressibility case results in a storage of only 186 000 $m^3$ into the huge compartment of B6 in the Sognefjord Fm. (See Appendix B, which had a volumetric storage potential of 2 760 000 $m^3$ for the middle case, being almost 15 times as much $CO_2$ (mass).

This low compressibility case show that the compressibility limit is in fact important to acknowledge, and something to have in mind when injecting $CO_2$ into sealed pressure compartments as it can limit the total injection volume of a $CO_2$ storage project significantly, by lowering the possible storage volume of the compartments. A small conclusion to the compressibility limit is put together in the subsection to follow.

### 8.2.4 Conclusion

The box volume approach constructs a constraint on the injectivity equation, which is a maximum value of total stored volume possible in regards to the compressibility of the compartment rock. This compressibility limit is important to acknowledge, but is hardly ever a limiting factor when considering realistic compressibility values, as we see for e.g. the compressibility case of $3 * 10^{-9}$ $Pa^{-1}$. The very smallest compartment can be considered problematic, because of its small volume. However, the injection and total storage capacity is for the very most of compartments restricted by the reservoir pressure as the maximum well pressure of the compartment is reached. The communication and spreading of the injected $CO_2$ in the formation is of much higher importance than the compressibility limit from the box volume approach. Take note that these results and conclusions are related the set, selected parameters used for the assessment. Even if these parameters are carefully selected to resemble realistic cases, One could expect that changing up the parameters could change the evaluation.

## 8.3 The $\Delta P$ limit

It was found in Section 8.2 that the compressibility can constrain the injectivity equation and the total storage volume when injecting into the compartments. When assessing the box volume approach (Equation 4), and perhaps by writing it on the form

$$\Delta V_b = C_b * V_b * \Delta P \tag{14}$$

one can further see that another factor also can set a similar constraint, being the pressure change $\Delta P$.

If we start of by considering the upper case of 7 MPa from the results in Section 7.3, only one compartment was constrained, being the D7 compartment. This $\Delta P$ case could be considered a rather generous excess pressure, and perhaps a little high for our prospect. However, it is the excess pressure of the Snøhvit $CO_2$ storage cite, and should be considered both possible and realistic. As for out middle case, there are similar results, with only D7 being restricted. The lower bound case of 1 MPa will also only restrict D7. If we look at the second smallest compartment D6, the difference between initial and maximum well pressure is rater small, and the maximum pressure is reached long before the constraint from the lower bound of the $\Delta P$ is reached. Take note that this selected $\Delta P$ is rather low, and typical for shallower formations ($<$ 800m). For reference, D7 in the Sognefjord Fm. has a mean depth of 1 023m, and could likely take on a higher excess pressure than the selected lower bound. This implies for all scenario compartments.

As these three, realistic values of excess pressure is tested for the scenarios, one can see that the selected range will not affect the very most of the compartments, as the maximum well pressure is

reached before the volumetric constrain from $\Delta P$ is reached. It is again the D7 that is a concern, and one can again consider this compartment size as problematic in terms of $CO_2$ injection at the rates we are considering.

### 8.3.1 Conclusion

Brief conclusions of Sections 8.2 and 8.3 can certainly be connected to the new equation form of the volumetric constrain (Equation 14). It it concluded that the realistic cases tested for compressibility $C_b$ (e.g. the middle case) and pressure change $\Delta P$ (all three cases) result in no constraints, besides for the very smallest compartment, with a low $V_b$. The D7 compartment has a total pore volume of 8 380 992 $m^3$ and one would have to multiply either $C_b$ or $\Delta P$ by around 10 for the compartment not to be constrained by the volumetric change possible from these values. Multiplying the $C_b$ and $\Delta P$ values that has been considered in these sections by 10 does not construct reasonable, realistic values, and one can followingly say this compartment size in unideal for $CO_2$ storage at the tested rates. The second largest compartment is unproblematic in terms of the constraints from $C_b$ and $\Delta P$, and one should aim at compartment sizes of 10 000 000 $m^3$ and above, to be able to eliminate compressibility and pressure change constraints.

## 8.4 Maximising Pore Volume

A very interesting question to pose next is which of the three scenarios maximises storage capacity at Smeaheia. A classic hypothesis is that one would need 'open' compartments as to maximise the storage volume, yet the conclusion on the compressibility limit of Section 8.2 challenge this hypothesis. Lets take a further look at some results.

As a start, one can consider the case of Figure 21. This is a case where we consider the area of B1 from Appendix B in three different ways, being either one big, two smaller, or three even smaller compartments. As mentioned, a hypothesis would be that bigger, more open compartments would be more ideal. However, the table shows that Scenario D of three smaller compartments brings out the largest injection volume. What is the reason for this? The three scenarios has the exact same total rock volume, and followingly the same total rock pore volume. If one could utilize every inch of the pore volume of the rock, the results would look identical. However, the pressure management approach used for this assessment reveal that there are many factors playing in. Conclusions were drawn that the restriction limits from the $C_b$ and $\Delta P$ on the compartments is hardly ever a limiting factor, and that the total storage capacity of a compartment is mostly restricted by reservoir pressure. An aim should then be to understand the pressure behavior that the equation demonstrates, and how this is different for big and small compartments.

If we consider two compartments in the same area of different sizes, such as for instance B2 and C3, one can expect similar initial and maximum well pressure. What will vary the pressure behavior is then the scaling parameter A, as found in Section 8.1. As discussed, A is a parameter that affects the rate of pressure increase and decrease. This further implies that smaller compartments, of larger A values, will to an extent have a higher relative rate of injected $CO_2$. At the same time, the pressure increases more rapid, and will reach the maximum well pressure faster. As the maximum well pressure is reached, the injection is stopped. One could further imagine an optimum in terms of compartment size, where you would want a relatively high A value, but not to reach the maximum well pressure too rapidly.

By studying the results of Figure 21 - 26 one can see a variety in which scenario maximises the injection volume. The results align with the suggestion that there is some sort of optimum, a perfect combination of parameters which gives the largest injection volume compared to total compartment volume. Figures 21, 23, and 24 show that scenario D of several smaller compartments gives the largest injection volume. Figures 22, 25, and 26 show cases where Scenario B of one large compartment gives the largest injection volume. However, one should reconsider the specific case of Figure 25. As discussed in Section 8.1, B5 was a particular case, where A was originally negative. As the choice of A=2 is highly uncertain and more of a rough prediction, this part was excluded from the results in the right table of Figure 27 as to have less uncertainty related the result.

It is challenging to make a conclusion on either of the tables of Figure 27. It is clear that the hypothesis of larger compartments is not necessarily correct, and that Scenario C seems to be the less ideal scenario, either way. However, the different cases gives significantly different results as to which of scenarios B and D stores the most $CO_2$. As stated, there are many factors and parameters playing in.

### 8.4.1 Conclusion

Evaluation of storage capacity shows it is not necessarily a straight forward answer of either smaller or larger compartments maximising the storage capacity. There is a complex relationship, and many uncertain parameters play in. As to further evaluate, advanced analysis can be done of the data as to extract information and characteristics to find an optimum in terms of maximising the storage capacity for the prospect area.

## 8.5 Sensitivity

For the initial assessment of the sensitivity, each tornado plot from the results of Section 7.5 is considered separately before a brief comparison and conclusion.

The first tornado plot of Figure 28 display compartment B2. This is a comparatively large compartment, which stores a high $CO_2$ mass accordingly. The overwhelming driver for this compartment is the injectivity. The drivers of the output variable reveal that this is a compartment restricted by the left side of the equation of Figure 13, as pressure change, compressibility and porosity show such variety of the output. Increasing these input variables increases the constraint on total volumetric change possible for the compartment (see Equation 14), hence the total storage mass increases. Decreasing these input parameters will naturally lower the constraint on the volumetric change, and less $CO_2$ can be stored in the compartment. Further, one can see that with the left side of the equation limiting the injection, the parameters of the right side of the equation have negligible impact on output. This is excluding the injectivity index, where the low bound is in fact an overwhelming driver on output. The high bound injectivity shows no effect as the restriction is already reached for the middle value, whereas the lower bound results in an output mass that is below the restriction and in consequence bring out a change in the total storage mass output. The reason that the injectivity show such effect on output should be considered in relation to its selected range. One can argue that the selected injectivity range is significantly more extensive than other narrower ranges selected (such as initial pressure, maximum well pressure, and area size), and therefore showing a higher impact on the output. The low bound of the injectivity at 50 $m^3/day/bar$ can easily compare to the value selected for initial calculations, and the tornado plot shows how the difference of the lower and higher bound range the total storage mass from a couple of Mt (as seen in most results from initial calculations) to over 40 Mt of stored $CO_2$ for this compartment. This suggest that the injectivity index is a major contributor to the total storage mass of the compartments, specifically related to its extensive range.

The tornado plot for compartment B4 in Figure 29 show different results in terms of which and to which degree parameters affect the total storage mass of the compartment, despite that the same variances of parameters is applied as for B2. Drawing a comparison between the two compartments, one can here understand that both sides of the equation of Figure 13 are impacting the output. The reason for this would be that the middle value of this compartment, resulting in a total storage of 30,93 Mt of $CO_2$ lands close to the constrain from the left side of the equation, which is at 40,86 Mt. This further results in both sides of the equation impacting the output mass. Ranging the parameters of the right side of the equation (injectivity, maximum well pressure and initial pressure) results in the constraint of 40,86 Mt being reached, whereas factors such as the compressibility can extend this maximum limit of stored mass by increasing the volumetric constrain, and followingly one sees an increased output where almost 60 Mt of $CO_2$ can be stored.

The last tornado plot is for compartment D6, i Figure 30. This is a small compartment, only storing a total mass of 3,315 Mt with the middle values. Drawing a comparison between this compartment and B2, one can see that the drivers of the output is reversed. One can presume this compartment

does not reach the constrain from the left side of the equation, as neither compressibility, pressure change or porosity affect the output. One can in fact expect the compartment to be far from reaching the constraint as neither the low or high bound of these parameters shows an impact. However, the parameters on the right side of the equation impact the output. The reason for this is likely that the small area size gives a large A value, which accelerates the pressure rise, resulting in the compartment reaching its maximum well pressure in the first year of injection. One can here see that the compressibility distribution has no impact in the total storage mass, because the injection is either way stopped after the first year. However, variety in pressure and injectivity (right side of equation) show an impact on the output. These are the factors that can influence the injection period for the compartment, by resulting in a shorter or longer time period for the reservoir pressure to reach the maximum well pressure.

### 8.5.1 Conclusion

A first conclusion to the sensitivity analysis is that the selected parameter distributions have different effects on the different compartments. Defining which parameters variate the total storage mass output the most is no trivial task. The main drivers of large, medium and small compartments are proved to be different, and have varying impacts. However, one can conclude that the factors directly influencing the pressure behavior are generally overwhelming drivers to the compartments. These factors are injectivity, compressibility (because of A), maximum well pressure, and initial pressure (right side of equation). The reason for this is as discussed, connected to the length of the injection period. 'Ideal' bounds affect the pressure behavior in a way that it takes longer for the compartment to reach the maximum well pressure, resulting in a higher mass being stored.

Overall the most overwhelming factor is the injectivity index. The injectivity index range is extensive, however based on real numbers. The sensitivity analysis show how a compartment such as e.g. B2 ranges from a total storage mass of just a couple of Mt to over 40 Mt of stored $CO_2$, all within realistic injectivity indexes.

## 8.6 Distributions and Sampling

The first plots of Section 7.6 presents the cases of set parameters. Plotting all cases by compartment pressure versus injected volume show some clear clustering, such as in Figure 33. As the x-axis (injection volume) is set logarithmic there seems to bee a somewhat linear relationship between the compartment pressure and injected volume (log). One can see some outliers, perhaps another, smaller cluster down right from the main cluster. One can see that these seem to be larger compartments, and it is reasonable that the three points of the larges storage volume and relatively low pressure is compartment B5 of the three formations (three different colored points). In an equivalent way one can see three outlying points to the lower left in the plot, most likely being the very small compartment D7.

Figure 34 presents the pressure and injected volume of the same compartment cases at year 50 of injection. One can see that some compartments experience an increase in pressure and injected volume within the 25 year gap between the two plots, while some compartments are decreasing in pressure (towards their initial pressure). For these compartments there is no change in injection volume. Most compartments stay more or less the same from year 25 to 50, presumably as this is the second half of injection period, where many compartments have stabilized back at their initial pressure.

Further, parameter distributions were applied the compartments in Figure 35 and 36. These plots show the compartment pressure versus total mass of injected $CO_2$. One can here perhaps see more clustering based on the formation layers, where same colors seem to have similar trends. This is not surprising, considering each formation layer has individual distributions. One can see some of the bigger compartments reaching the highest total injection masses, which is expected.

The plots of this section show clear clustering that could further be interesting to analyse. One could sample more points by the input distributions and ranging uncertainty. Machine learning

algorithms could be used to study the data, and patterns in the data clouds could be found.

One aspect to consider before evaluating this data, is that these plots show two dimensions. Figure 35 and 36 plot compartment pressure up against the injected mass. As seen, each compartment holds many additional factors that are interesting in relation to these results. Before analysing this data further, one can include more variables through PCA. With PCA one can reduce the dimensions of the data, as to compare and get a simple result for interpretation. The aim is to group several variables in few dimensions.

## 8.7 Principal Component Analysis

For the PCA analysis three different preliminary results were retained from three cases considering different parameters.

Case 1 tested the original parameters of total storage volume, initial pressure, maximum well pressure, and total injected volume for each compartment. By studying Figure 37 (b) one can firstly see a couple of outliers. This could likely be the big compartment B5, as one can see these two compartments are from Scenario B. By studying (b) one can see that the first principal component shows a high variance (this is confirmed in (a)). Perhaps the darker colors (Sognefjord compartments) are plotted more to the right whereas the deeper compartments more to the left. This aligns well with the eigenvalues of the component, as the first component is strongly dependent on the initial pressure and maximum well pressure. The shallower compartments have lower both initial and maximum pressure values. The component contrasts these pressure variables from total storage volume and total injection volume, which is reasonable considering the three scenarios of different compartment sizes are placed at three different depths (formations). The second principal component seems to be separating the scenarios, hence the total compartment storage volume and injection volume. This aligns with the eigenvectors, showing high, positive association with storage and injection volume.

Case 2 tested the original parameters of total storage volume/injected volume ratio, difference between initial pressure and maximum well pressure, total injection volume, and injectivity index. One can from results in Figure 38 (b) see that the first principal component separates the three scenarios B, C and D, corresponding to compartment size (total injection volume). The second principal component seems to separate the three formations, which is related to the pressure difference (depth). The krossfjord compartments have mostly positive values, the Fensfjord compartments are clustered around 0, and the Sognefjord compartments have values clustered around -1. Recall that the injectivity index is a fixed parameter for each formation layer, and this may have caused the more 'systematic' distribution for this case. One could expect that the more you fix parameters the less advanced the statistical analysis will be, and one should aim for as much freedom of parameters as possible. The eigenvectors of Case 2 compliments and refines the interpretation above. The loadings of the variables suggest that the first principle component is positively associated with total storage volume and injectivity index, separating the compartments mainly by size. One can also see that the injectivity index contributes, as the Krossfjord compartments are drawn back compared to the Fensfjord and Sognefjord compartments. The second principle component is positively associated with the volume ratio, and negatively associated with the pressure difference. This is quite interesting, as it shows how the smaller compartments store more $CO_2$, relatively. It also shows that the pressure difference has a relation to this, which is coherent with what was found in Section 8.1; that a higher pressure difference conditions a longer injection period and a higher total injection volume (affecting the volume ratio positively).

The last case, Case 3, differs from Case 2 as it switches the fixed injectivity index parameter with initial pressure, which can be considered as a connection to the compartment depths as well, however less fixed as it is calculated based on the true mean depth for each single compartment. One can from the results of Figure 39 (b) gather that the first principal component has a high variance (verified in (a)). One can see that the formation layers are somewhat parted, with the Sognefjord compartments (darker points) at higher, positive values of the first principal component, whereas the Fensfjord and Krossfjord compartments are plotted more to the left. The second principal component seems to distinguish the scenarios. The Scenario B compartments (blue)

seem to have higher values of the second principal component, whereas the latter scenarios have lower values. Again, the eigenvectors compliment the findings. The first principal component is negatively associated with pressure difference and initial pressure. This results in positive values for the Sognefjord compartments as these compartments have the lowest pressure difference and initial pressure. The deeper compartments have a higher initial pressure and higher pressure difference resulting in lower and negative values as the association is negative. The second principal component is highly dependent on the total injection volume, as clearly seen by how the three scenarios are plotted differently along this axis.

### 8.7.1 Conclusion

These preliminary results are meant to show the way forward in terms of exploring the parameter space of a complex problem. One can see how fixed parameters such as the injectivty index affected the results. Fixed parameters related compartment size or formation layer would cause a higher correlation between parameters than one perhaps can expect in realistic cases. Parameters are likely correlated, but not as strongly correlated as e.g. setting a specific injectivity index for all compartments of a certain formation layer would imply. Future work should aim to have more freedom of parameters, perhaps by more sampling. One could further make a really advanced analysis of which parameters control which effects of this complex system.

The goal of PCA is to group the variables in fewer dimensions. As multiple variables are defined by a component it implies they are correlated. Before evaluating data clouds such as presented in Section 7.6 one can reduce dimensions through PCA as to better compare and interpret the complex results and correlations trough e.g. clustering.

# 9 Summary & Conclusion

**Summary**

Large-scale $CO_2$ storage will be an important technology to reduce the concentration of emitted $CO_2$ in the atmosphere. Large-scale, subsurface storage in geological formations is one of the most promising options, where pressure management is a key issue.

A pressure management approach was put together and evaluated. First the approach is applied to data of set parameters, where deterministic calculations were carried out. Following this a more realistic perspective is presented, where parameters and their relations are more uncertain. This calls for data analysis of sampled data as to understand more of the complex controls of the pressure management approach.

The prospected storage site evaluated for this study is the faulted storage prospect region of Smeaheia. Thee sandstone formations condition high storage potential, where the structural trapping of faults are expected to create pressure compartments with sealing boundaries. The pressure compartments are further considered closed systems when evaluating the pressure behavior under $CO_2$ injection, where the thought is to inject $CO_2$ into each pressure compartments separately.

Through fault interpretation using simplified fault extensions and artificial boundaries, three contrasting compartment scenarios were put together. Scenario B consists of 6 bigger compartments based on the first-order faults of the area, scenario C of 12 compartments assuming some additional smaller faults, and scenario D representing a highly compartmentalized case of 24 compartments. Each scenario is applied in three stratigraphic levels.

The work with set parameters developed the following findings:

- The pressure behavior of the fault compartments is highly dependent on compartment size.
- Scaling parameter A is in like manner a key parameter to the pressure behavior. The conceptualized linear function for its relationship to compartment area size is oversimplified and raises great uncertainty to results.
- The box volume approach constructs a constraint on the injectivity equation. This is a limiting value for volumetric change possible for a compartment. The constraint is controlled by rock compressibility, pressure change and initial compartment pore volume.
- The tested, realistic values of compressibility and pressure change are mostly not constraining the capacity of the pressure compartments, aside from the very small compartments of area sizes under 10 000 000 $m^2$. This result should be considered specific for the selected injectivity index used for the calculations.
- Trends show that scenarios of more, smaller pressure compartments could be ideal as to maximise total available pore volume and followingly total stored mass of $CO_2$ for the prospect area.

The work with variable parameter distributions developed the following findings:

- The main controls of large, medium, and small compartments are found to be different, and having varying impacts.
- Altogether the factors directly influencing the pressure behavior, being injectivity, compressibility (because of A), maximum well pressure, and initial pressure of the compartments are found to be of highest impact on the total storage mass possible for each compartment.
- PCA shows preliminary results where initial proposals of correlated parameters are found from the components. Fixed parameters affect the results, and can give higher correlations between parameters than what one should realistically expect. An aim should be more freedom of parameters, where an advanced analysis of parameter controls on the complex system can be carried out.

**Conclusion & future work**

This report presents a study of factors governing pressure behavior of fault compartments. A pressure management approach is applied to a faulted basin scale model, by considering multiple fault compartments as closed, non-communicating systems.

Many factors are found to affect the pressure behavior of the compartments, such as the compressibility, compartment size, porosity, injectivity, pressure limits, initial pressure, and the scaling parameter A. Many of the parameters are correlated and have complex relationships. The pressure behavior under injection is closely related to the total storage mass possible to obtain for the compartments, and is therefore a very important aspect to maximising the storage potential.

The main controls of large, medium and small compartments are concluded to be different. Altogether it was found that the factors affecting the volumetric constraints are less important, whereas the factors affecting the injectivity equation are stronger drivers. These are A, the injectivity index, maximum well pressure, and initial pressure of a compartment. Overall the injectivity index was the overwhelming driver. An extensive, but realistic range was assessed and the results presented significant variety in total storage mass.

The parameter distribution and conceptualized relationships are deemed to raise great uncertainty. An aim should be to further develop a deeper analysis as to find parameters and their true relationships. Future work should continue the implementation of machine learning approaches, ultimately exploring the parameter space to find an optimum to maximising the storage potential for closed, and also communicating pressure compartments.

# Bibliography


Abdi, H. & Williams, L. J. (2010). Principal component analysis. *Wiley interdisciplinary reviews: computational statistics*, *2*(4), 433–459.

Aladejare, A. & Wang, Y. (2016). Evaluation of rock property variability. *Georisk*, *11*. https://doi.org/10.1080/17499518.2016.1207784

Bachu, S. (2015). Review of co2 storage efficiency in deep saline aquifers [Special Issue commemorating the 10th year anniversary of the publication of the Intergovernmental Panel on Climate Change Special Report on CO2 Capture and Storage]. *International Journal of Greenhouse Gas Control*, *40*, 188–202. https://doi.org/https://doi.org/10.1016/j.ijggc.2015.01.007

Birkholzer, J. T., Oldenburg, C. M. & Zhou, Q. (2015). Co2 migration and pressure evolution in deep saline aquifers [Special Issue commemorating the 10th year anniversary of the publication of the Intergovernmental Panel on Climate Change Special Report on CO2 Capture and Storage]. *International Journal of Greenhouse Gas Control*, *40*, 203–220. https://doi.org/https://doi.org/10.1016/j.ijggc.2015.03.022

Bøe, R., Magnus, C., Osmundsen, P. & Ringstad, B. (2002). *Co2 point sources and subsurface storage capacities for co2 in auifers in norway*. https://www.ngu.no/en/publikasjon/co2-point-sources-and-subsurface-storage-capacities-co2-auifers-norway

Bohloli, B., Ringrose, P., Grande, L. & Nazarian, B. (2017). Determination of the fracture pressure from co2 injection time-series datasets. *International Journal of Greenhouse Gas Control*, *61*, 85–93. https://doi.org/https://doi.org/10.1016/j.ijggc.2017.03.025

BP. (2020). Statistical review of world energy 2020. https://www.bp.com/content/dam/bp/business-sites/en/global/corporate/pdfs/energy-economics/statistical-review/bp-stats-review-2020-full-report.pdf

Braaten, A., Choi, J., Elenius, M., Mulrooney, M. & Skurtveit, E. (n.d.). *Large-scale co2 storage in smeaheia*. http://www.fme-success.no/doc//Reports/Smeaheia.pdf

Brobakken, I. (2018). *Modeling of CO2 Storage in the Smeaheia Field* (Master's thesis). NTNU. Trondheim.

Buşoniu, L., Babuška, R. & De Schutter, B. (2010). Multi-agent reinforcement learning: An overview. In D. Srinivasan & L. C. Jain (Eds.), *Innovations in multi-agent systems and applications - 1* (pp. 183–221). Springer Berlin Heidelberg. https://doi.org/10.1007/978-3-642-14435-6_7

Caine, J. S., Evans, J. P. & Forster, C. B. (1996). Fault zone architecture and permeability structure. *Geology*, *24*(11), 1025–1028. https://doi.org/10.1130/0091-7613(1996)024⟨1025:FZAAPS⟩2.3.CO;2

Cao, C., Liu, H., Hou, Z., Mehmood, F., Liao, J. & Feng, W. (2020). A review of co2 storage in view of safety and cost-effectiveness. *Energies*, *13*(3). https://doi.org/10.3390/en13030600

Carleo, G., Cirac, I., Cranmer, K., Daudet, L., Schuld, M., Tishby, N., Vogt-Maranto, L. & Zdeborová, L. (2019). Machine learning and the physical sciences. *Rev. Mod. Phys.*, *91*, 045002. https://doi.org/10.1103/RevModPhys.91.045002

Cavanagh, A. J. & Haszeldine, R. S. (2014). The sleipner storage site: Capillary flow modeling of a layered co2 plume requires fractured shale barriers within the utsira formation. *International Journal of Greenhouse Gas Control*, *21*, 101–112. https://doi.org/https://doi.org/10.1016/j.ijggc.2013.11.017

CCP, ( C. P. (2015). *Co2 trapping mechanisms*. https://www.co2captureproject.org/co2_trapping.html

Ceia, M., Missagia, R., Fasolo, R. & Neto, I. (2019). Relationship between porosity, permeability and pore compressibility. *UENF/LENEP*.

Cooper, C. (2009). A technical basis for carbon dioxide storage. *Energy Procedia*, *1*, 1727–1733. https://doi.org/10.1016/j.egypro.2009.01.226

Cutler, J. & Dickenson, M. (2020). Introduction to machine learning with python. *Computational frameworks for political and social research with python* (pp. 129–142). Springer International Publishing. https://doi.org/10.1007/978-3-030-36826-5_10

European Comission, . (n.d.). *Causes of climate change*. Retrieved 4th December 2021, from https://ec.europa.eu/clima/climate-change/causes-climate-change_en

Fawad, M., Rahman, M. J. & Mondol, N. H. (2021). Seismic reservoir characterization of potential co2 storage reservoir sandstones in smeaheia area, northern north sea. *Journal of Petroleum Science and Engineering*, *205*, 108812. https://doi.org/https://doi.org/10.1016/j.petrol.2021.108812

*Final well report 31/3-3*. (1985). https://factpages.npd.no/pbl/wellbore_documents/447_01_31_3_3_Completion_Report_and_Completion_log.pdf

*Final well report 32/4-1*. (1996). https://factpages.npd.no/pbl/wellbore_documents/2918_32_4_1_COMPLETION_REPORT_AND_COMPLETION_LOG.pdf

Global CCS Institute, . (n.d.). *Geological storage of co2: Safe, permanent, and abundant*. Retrieved 5th December 2021, from https://www.globalccsinstitute.com/wp-content/uploads/2018/12/Global-CCS-Institute-Fact-Sheet_Geological-Storage-of-CO2.pdf

Harris, S. N. (2019). The tectono-sedimentary development of smeaheia on the horda platform with a focus on the cretaceous, and implications for co2 storage.

Holgate, N. E., Jackson, C. A.-L., Hampson, G. J. & Dreyer, T. (2013). Sedimentology and sequence stratigraphy of the middle–upper jurassic krossfjord and fensfjord formations, troll field, northern north sea. *Petroleum Geoscience*, *19*(3), 237–258. https://doi.org/10.1144/petgeo2012-039

Iglauer, S. (2011). Dissolution trapping of carbon dioxide in reservoir formation brine – a carbon storage mechanism. https://doi.org/10.5772/20206

Iooss, B. & Lemaıtre, P. (2015). A review on global sensitivity analysis methods. *Uncertainty management in simulation-optimization of complex systems* (pp. 101–122). Springer.

IPCC. (2022). *Climate change 2022: Impacts, adaptation, and vulnerability.* The Intergovernmental Panel on Climate Change.

James, G., Witten, D., Hastie, T. & Tibshirani, R. (2013). *An introduction to statistical learning* (Vol. 112). Springer.

John, B. (2018). Chapter 2 - importance of geological studies in earthquake hazard assessment. In P. Samui, D. Kim & C. Ghosh (Eds.), *Integrating disaster science and management* (pp. 27–40). Elsevier. https://doi.org/https://doi.org/10.1016/B978-0-12-812056-9.00002-6

Karpatne, A., Ebert-Uphoff, I., Ravela, S., Babaie, H. & Kumar, V. (2018). Machine learning for the geosciences: Challenges and opportunities. *IEEE Transactions on Knowledge and Data Engineering*, *31*(8), 1544–1554.

Kassambara, A. (2017). *Practical guide to principal component methods in r: Pca, m (ca), famd, mfa, hcpc, factoextra* (Vol. 2). Sthda.

Kaszuba, J. P., Janecky, D. R. & Snow, M. G. (2003). Carbon dioxide reaction processes in a model brine aquifer at 200 °c and 200 bars: Implications for geologic sequestration of carbon. *Applied Geochemistry*, *18*(7), 1065–1080. https://doi.org/https://doi.org/10.1016/S0883-2927(02)00239-1

Kettermann, M., Smeraglia, L., Morley, C. K., von Hagke, C. & Tanner, D. C. (2020). Chapter 8 - fault sealing. In D. Tanner & C. Brandes (Eds.), *Understanding faults* (pp. 283–350). Elsevier. https://doi.org/https://doi.org/10.1016/B978-0-12-815985-9.00008-4

Krevor, S., Blunt, M. J., Benson, S. M., Pentland, C. H., Reynolds, C., Al-Menhali, A. & Niu, B. (2015). Capillary trapping for geologic carbon dioxide storage – from pore scale physics to field scale implications [Special Issue commemorating the 10th year anniversary of the publication of the Intergovernmental Panel on Climate Change Special Report on CO2 Capture and Storage]. *International Journal of Greenhouse Gas Control*, *40*, 221–237. https://doi.org/https://doi.org/10.1016/j.ijggc.2015.04.006

Ladislav, V., Vaclav, D., Ondrej, B. & Vaclav, N. (2016). Pinch point analysis of heat exchangers for supercritical carbon dioxide with gaseous admixtures in ccs systems [The 8th Trondheim Conference on CO2 Capture, Transport and Storage]. *Energy Procedia*, *86*, 489–499. https://doi.org/https://doi.org/10.1016/j.egypro.2016.01.050

Li, C., Chen, X. & Du, Z. (2004). A new relationship of rock compressibility with porosity. *SPE Asia Pacific oil and gas conference and exhibition.*

Li, Z., Dong, M., Li, S. & Huang, S. (2006). Co2 sequestration in depleted oil and gas reservoirs—caprock characterization and storage capacity. *Energy Conversion and Management*, *47*(11), 1372–1382. https://doi.org/https://doi.org/10.1016/j.enconman.2005.08.023

Lindsay, N., Murphy, F., Walsh, J., Watterson, J., Flint, S. & Bryant, I. (1993). Outcrop studies of shale smears on fault surfaces. *The geological modelling of hydrocarbon reservoirs and outcrop analogues*, *15*, 113–123.

Linstrom, P. & Mallard, W. (2015). *Nist chemistry webbook, nist standard reference database number 69.* https://doi.org/10.18434/T4D303,

Liu, Q. & Maroto-Valer, M. M. (2014). Study of mineral trapping of co2 and seal leakage mitigation [12th International Conference on Greenhouse Gas Control Technologies, GHGT-12]. *Energy Procedia*, *63*, 5490–5494. https://doi.org/https://doi.org/10.1016/j.egypro.2014.11.581

Lothe, A., Bergmo, P. & Grimstad, A.-A. (2019). *Storage resources for future european ccs deployment; a roadmap for a horda c02 storage hub, offshore norway.*

Machine Learning with MATLAB. (n.d.). https://se.mathworks.com/campaigns/offers/machine-learning-with-matlab.html?ef_id=Cj0KCQiA0eOPBhCGARIsAFIwTs6rW0r54sVsY0Z4UuAhbA1CmluABa2Iyg3GUsJHkGWjW8bvhsBIDgwaAnt2EALw_wcB:G:s&s_kwcid=AL!8664!3!281794527512!p!!g!!machine%20learning&s_eid=psn_57384022512&q=machine%20learning&gclid=Cj0KCQiA0eOPBhCGARIsAFIwTs6rW0r54sVsY0Z4UuAhbA1CmluABa2Iyg3GUsJHkGWjW8bvhsBIDgwaAnt2EALw_wcB

Michie, E. A. H., Mulrooney, M. J. & Braathen, A. (2021). Fault interpretation uncertainties using seismic data, and the effects on fault seal analysis: A case study from the horda platform, with implications for $co_2$ storage. *Solid Earth*, *12*(6), 1259–1286. https://doi.org/10.5194/se-12-1259-2021

Mikhaylov, A., Moiseev, N., Aleshin, K. & Burkhardt, T. (2020). Global climate change and greenhouse effect. *Entrepreneurship and Sustainability Issues*, *7*(4), 2897.

Miri, R., Hellevang, H., Kvamme, B., Skurtveit, E. & Wangen, M. (2018). Critical factors for considering co2 injectivity in saline aquifers. *FME SUCCESS Synthesis report Volume 3.*

Mudford, B. & Kuch, S. (2003). *Stochastic Sensitivity Analysis: Or What Happened to my Tornado Plot?* (Vol. All Days) [SPE-84235-MS]. https://doi.org/10.2118/84235-MS

Mulrooney, M. J., Osmond, J. L., Skurtveit, E., Faleide, J. I. & Braathen, A. (2020). Structural analysis of the smeaheia fault block, a potential co2 storage site, northern horda platform, north sea. *Marine and Petroleum Geology*, *121*, 104598. https://doi.org/https://doi.org/10.1016/j.marpetgeo.2020.104598

Paasch, B., Ringrose, P., Furre, A.-K., Zweigel, P., Nazarian, B., Thorsen, R. & Ivar, P. (2017). *Industrial-scale ccs in norway: Experience gained and application to future projects.*

Patruno, S., Hampson, G. J. & Jackson, C. A. (2015). Quantitative characterisation of deltaic and subaqueous clinoforms. *Earth-Science Reviews*, *142*, 79–119.

Pawar, R., Bromhal, G., Carey, B., Foxall, W., Korre, A., Ringrose, P., Tucker, O., Watson, M. & White, J. (2015). Recent advances in risk assessment and risk management of geologic co2 storage. *International Journal of Greenhouse Gas Control*, *40*. https://doi.org/10.1016/j.ijggc.2015.06.014

Pei, Y., Paton, D. A., Knipe, R. J. & Wu, K. (2015). A review of fault sealing behaviour and its evaluation in siliciclastic rocks. *Earth-Science Reviews*, *150*, 121–138. https://doi.org/https://doi.org/10.1016/j.earscirev.2015.07.011

Pyrcz, M. (2019). *07 machine learning: Clustering.* Youtube. https://www.youtube.com/watch?v=oFE10cLl0Fs

Pyrcz, M. (2020). *06b machine learning course: Overfit*. Youtube. https://www.youtube.com/watch?v=oFE10cLl0Fs

Qader, M., Khan, S. & Kamal, M. (2021). Forecasting carbon emissions due to electricity power generation in bahrain. *Environ Sci Pollut Res (2021)*. https://doi.org/10.1007/s11356-021-16960-2

Rahman, M. J., Choi, J. C., Fawad, M. & Mondol, N. H. (2021). Probabilistic analysis of vette fault stability in potential co2 storage site smeaheia, offshore norway. *International Journal of Greenhouse Gas Control*, *108*, 103315. https://doi.org/https://doi.org/10.1016/j.ijggc.2021.103315

Raschka, S. (2015). *Principal component analysis*. https://sebastianraschka.com/Articles/2015_pca_in_3_steps.html

Ravnås, R. & Steel, R. (1997). Contrasting styles of late jurassic syn-rift turbidite sedimentation: A comparative study of the magnus and oseberg areas, northern north sea. *Marine and Petroleum Geology*, *14*(4), 417–449. https://doi.org/https://doi.org/10.1016/S0264-8172(97)00010-X

Ringrose, P. (2020). *How to store co2 underground: Insights from early-mover ccs projects*. Springer.

Ringrose, P. & Meckel, T. (2019). Maturing global co2 storage resources on offshore continental margins to achieve 2ds emissions reductions. *Scientific Reports*, *9*. https://doi.org/10.1038/s41598-019-54363-z

Ringrose, P., Furre, A.-K., Gilfillan, S. M., Krevor, S., Landrø, M., Leslie, R., Meckel, T., Nazarian, B. & Zahid, A. (2021). Storage of carbon dioxide in saline aquifers: Physicochemical processes, key constraints, and scale-up potential [PMID: 33872518]. *Annual Review of Chemical and Biomolecular Engineering*, *12*(1), 471–494. https://doi.org/10.1146/annurev-chembioeng-093020-091447

Saltelli, A., Ratto, M., Andres, T., Campolongo, F., Cariboni, J., Gatelli, D., Saisana, M. & Tarantola, S. (2008). *Global sensitivity analysis: The primer*. John Wiley & Sons.

Saltelli, A., Tarantola, S., Campolongo, F. & Ratto, M. (2004). Sensitivity analysis in practice: A guide to assessing scientific models. https://doi.org/10.1002/0470870958

Satter, A. & Iqbal, G. M. (2016). 3 - reservoir rock properties. In A. Satter & G. M. Iqbal (Eds.), *Reservoir engineering* (pp. 29–79). Gulf Professional Publishing. https://doi.org/https://doi.org/10.1016/B978-0-12-800219-3.00003-6

Sihvonen, M., Järvenpää, E., Hietaniemi, V. & Huopalahti, R. (1999). Advances in supercritical carbon dioxide technologies. *Trends in Food Science  Technology*, *10*(6), 217–222. https://doi.org/https://doi.org/10.1016/S0924-2244(99)00049-7

Silver, D. (2021). *Experimental study addressing fault slip* (Master's thesis). UiO. Oslo.

Smeaheia dataset. (n.d.). https://co2datashare.org/dataset/smeaheia-dataset

Smit, B., Reimer, J. A., Oldenburg, C. M. & Bourg, I. C. (2014). *Introduction to carbon capture and sequestration* (Vol. 1). World Scientific.

Soltanian, M. R., Amooie, M. A., Gershenzon, N., Dai, Z., Ritzi, R., Xiong, F., Cole, D. & Moortgat, J. (2017). Dissolution trapping of carbon dioxide in heterogeneous aquifers. *Environmental Science & Technology*, *51*(13), 7732–7741.

Tian, W. (2013). A review of sensitivity analysis methods in building energy analysis. *Renewable and Sustainable Energy Reviews*, *20*, 411–419. https://doi.org/https://doi.org/10.1016/j.rser.2012.12.014

Wu, L., Thorsen, R., Ottesen, S., Meneguolo, R., Hartvedt, K., Ringrose, P. & Nazarian, B. (2021). Significance of fault seal in assessing co2 storage capacity and containment risks – an example from the horda platform, northern north sea. *27*(3). https://doi.org/10.1144/petgeo2020-102

Yielding, G., Freeman, B. & Needham, D. T. (1997). Quantitative fault seal prediction. *AAPG bulletin*, *81*(6), 897–917.

Zhang, J. J. (2019). *Applied petroleum geomechanics*. Gulf Professional Publishing.

Zhou, Q., Birkholzer, J., Tsang, C.-F. & Rutqvist, J. (2008). A method for quick assessment of co2 storage capacity in closed and semi-closed saline formations. *International Journal of Greenhouse Gas Control*, *2*, 626–639. https://doi.org/10.1016/j.ijggc.2008.02.004

# Appendix

## A Faults

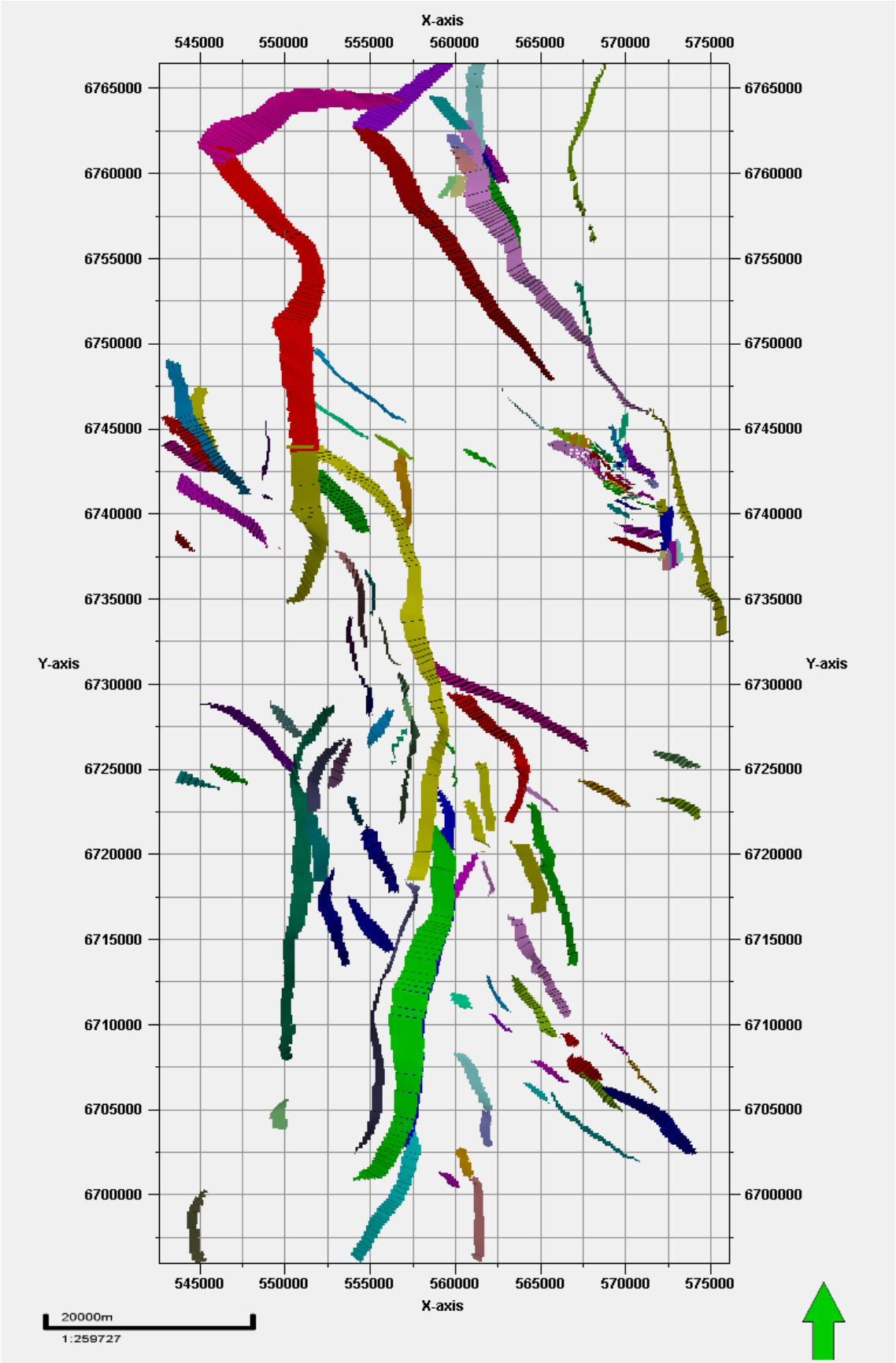

# B Scenario B - Pressure Compartments

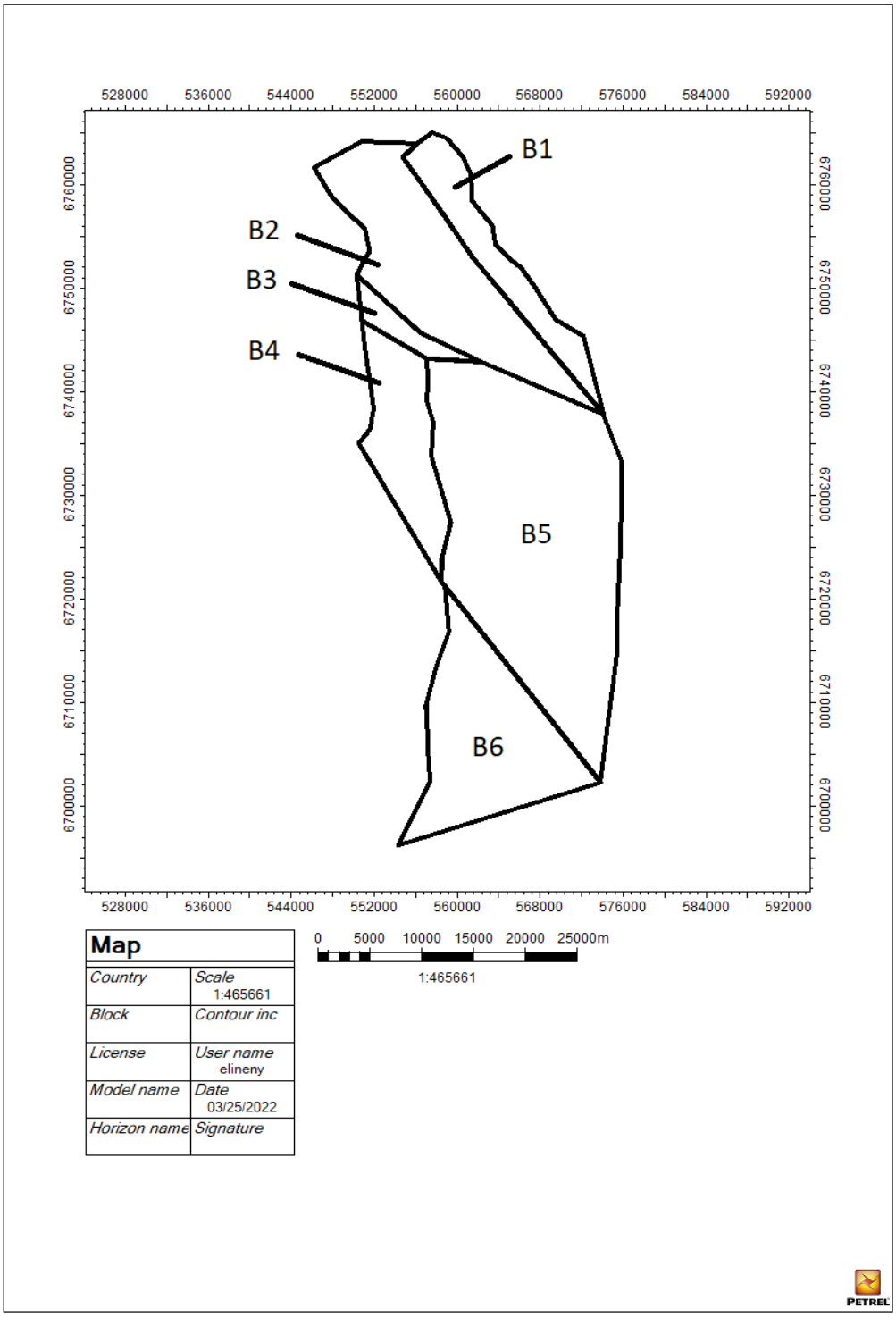

# C Scenario C - Pressure Compartments

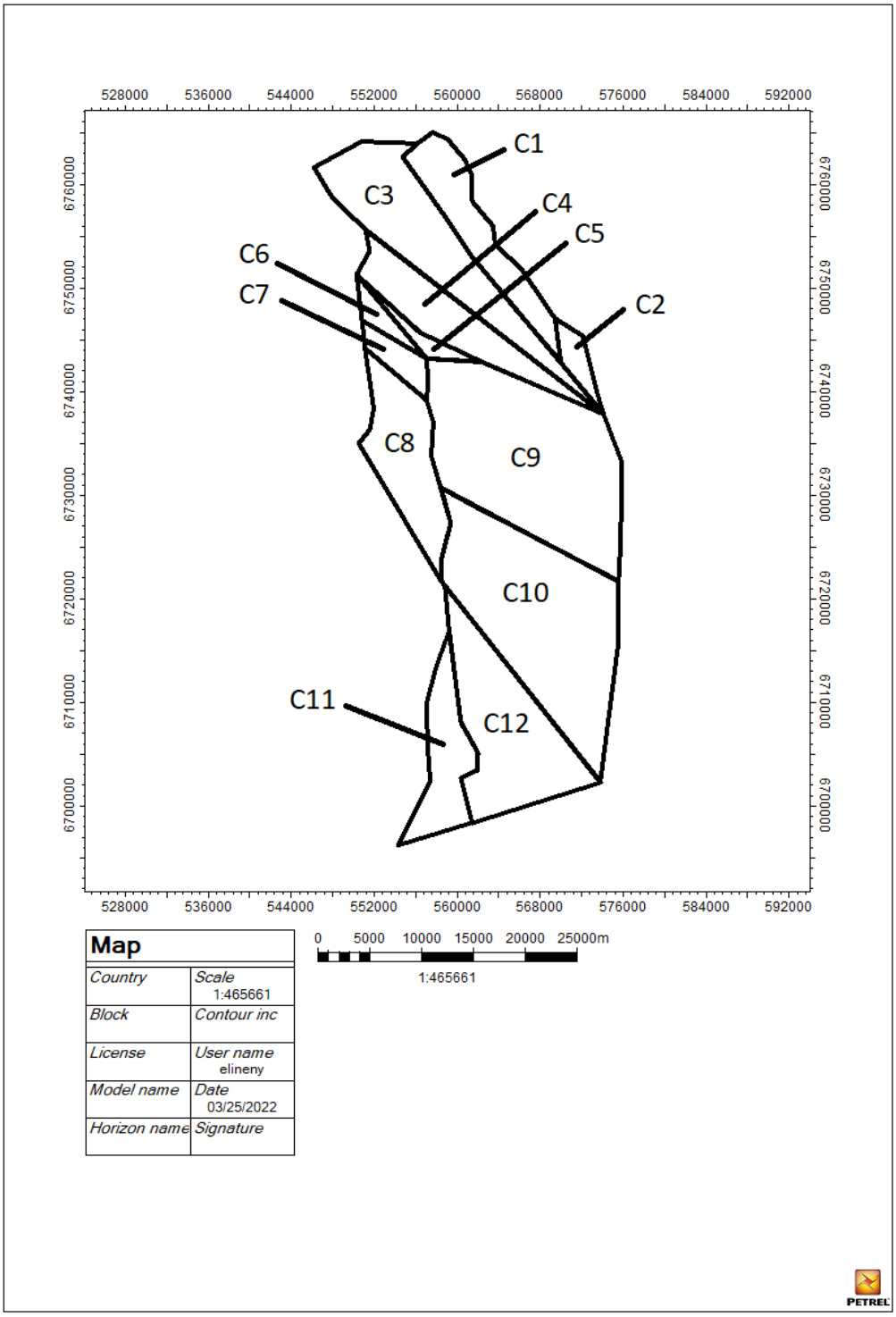

# D Scenario D - Pressure Compartments

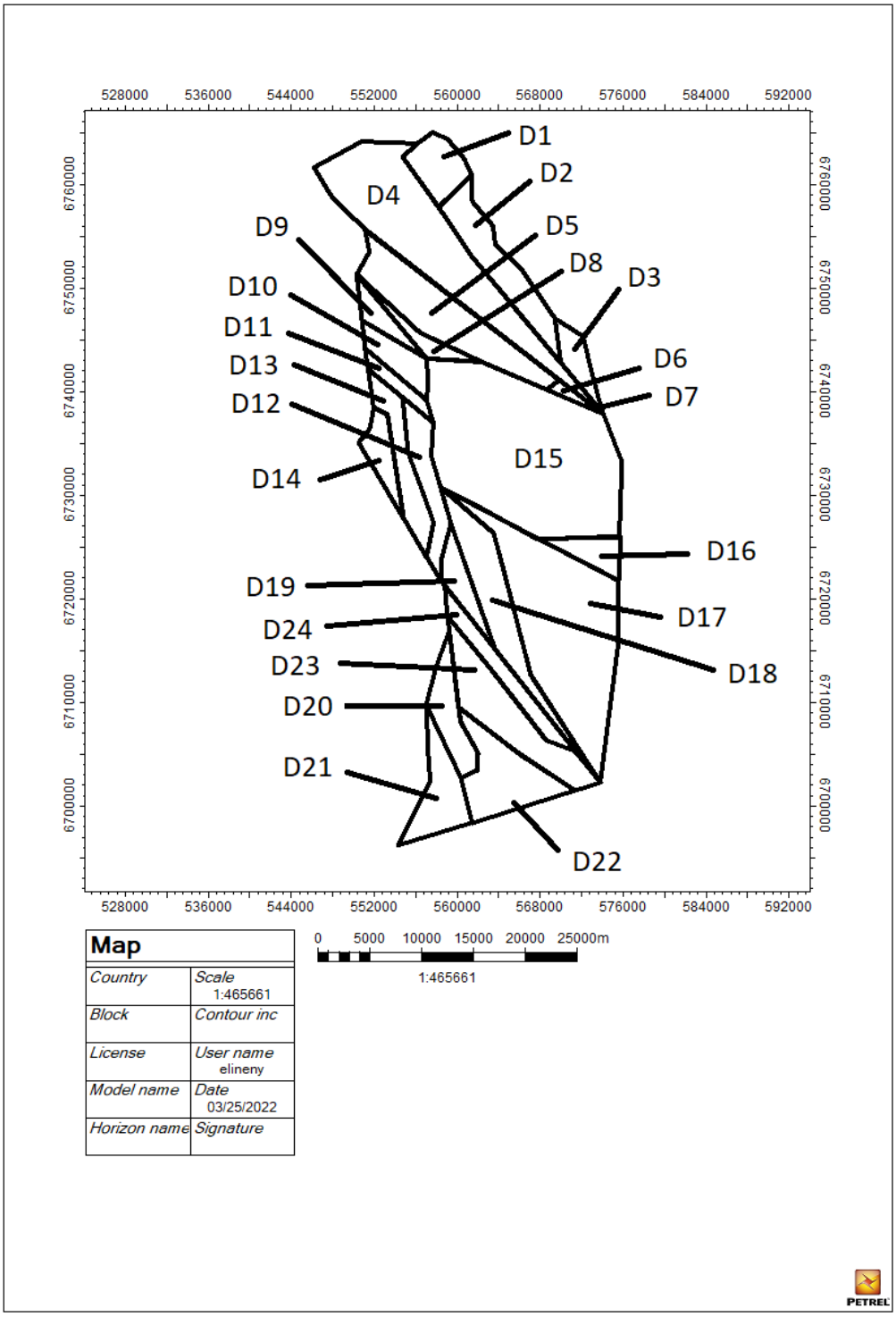

# E Scenario B - Thickness Depth Sognefjord Fm.

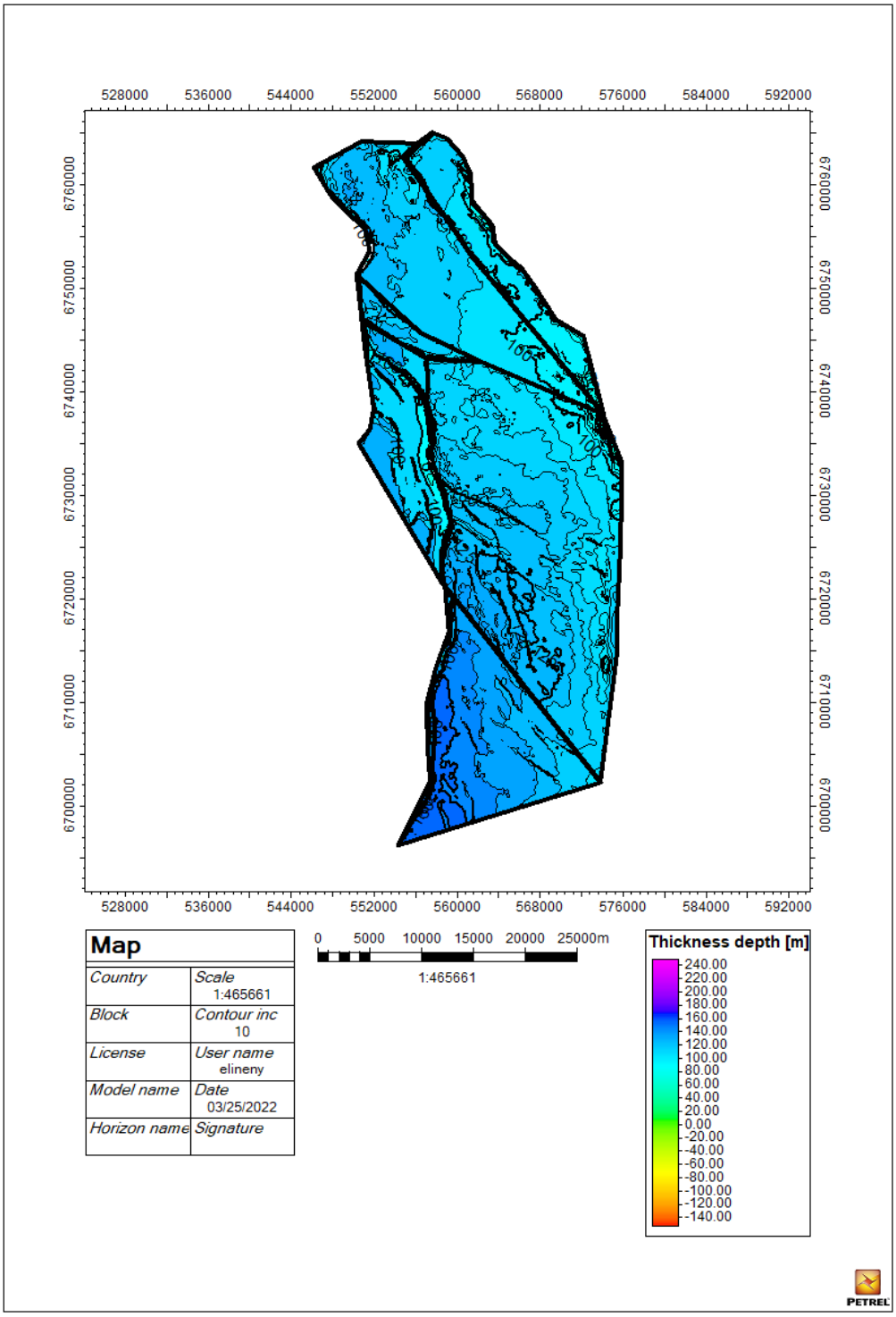

# F Scenario B - Thickness Depth Fensfjord Fm.

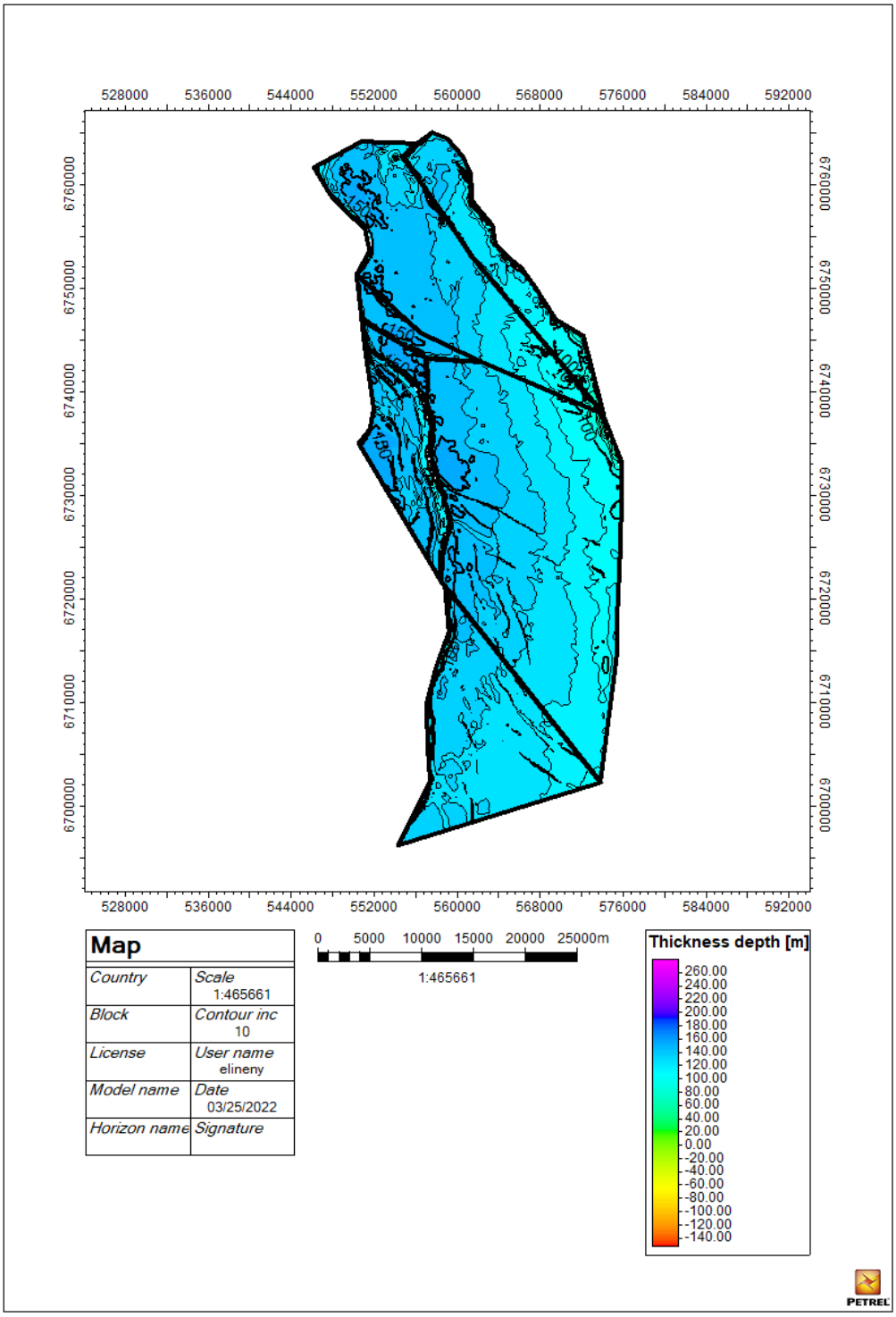

# G Scenario B - Thickness Depth Krossfjord Fm.

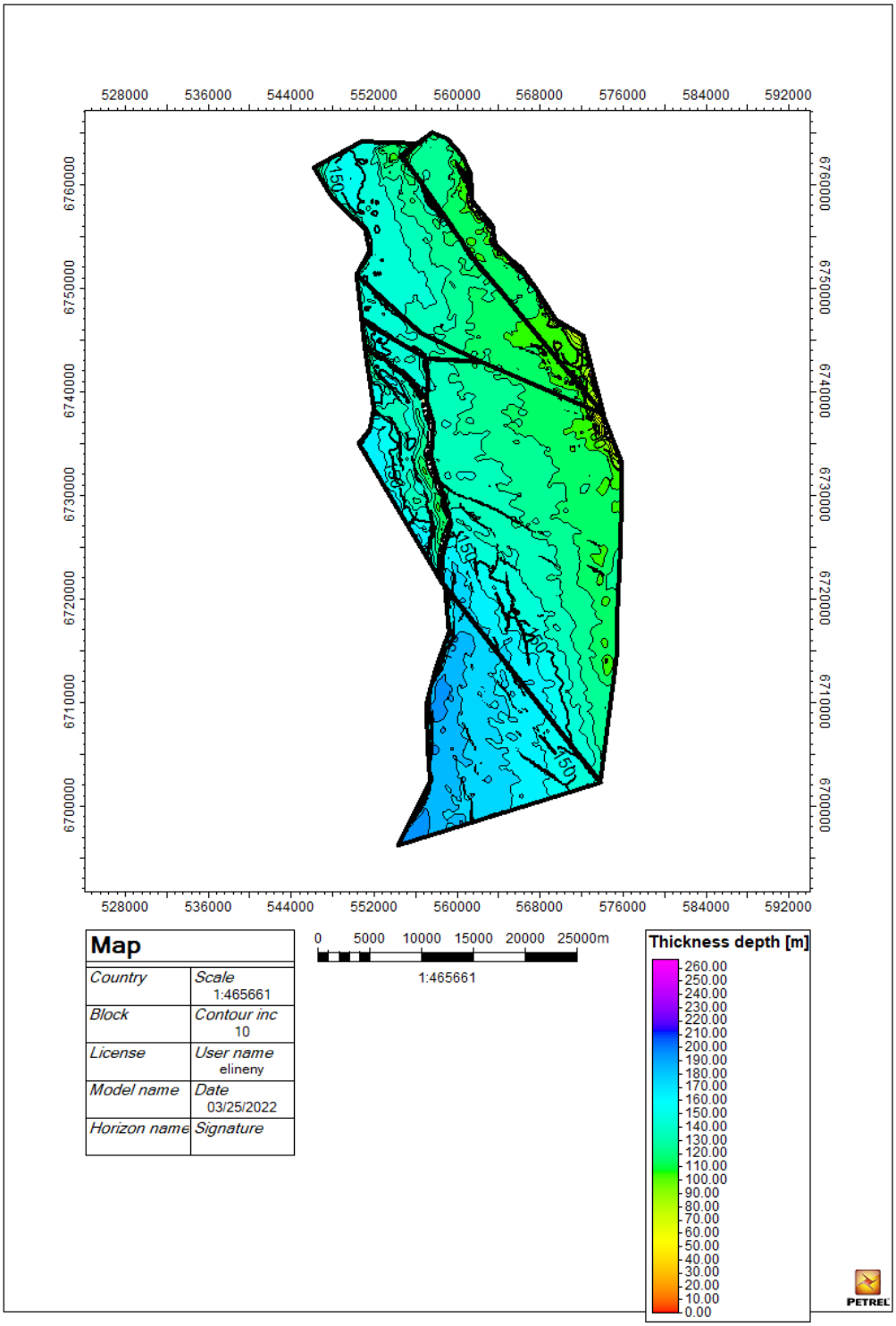

# H Scenario C - Thickness Depth Sognefjord Fm.

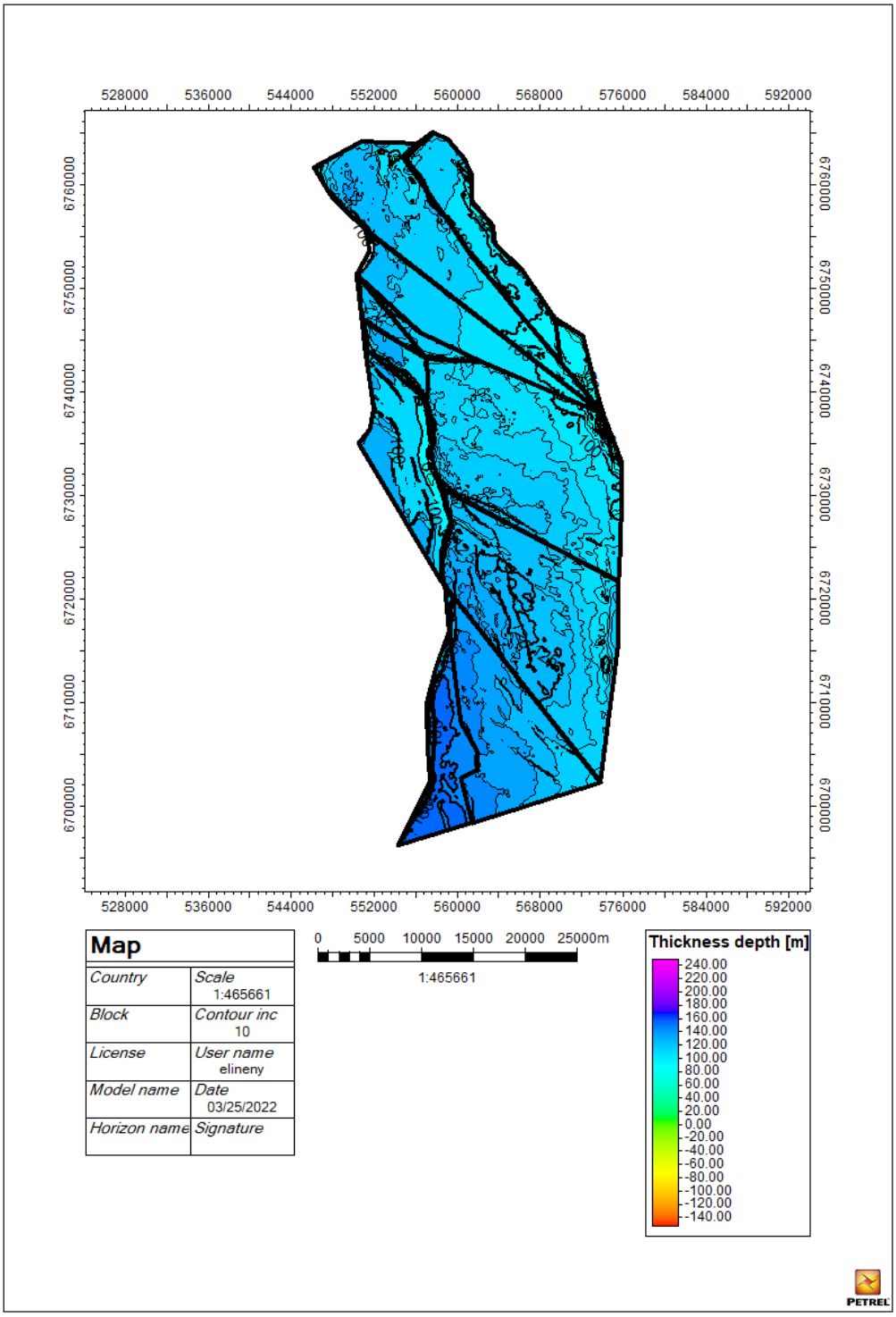

# I Scenario C - Thickness Depth Fensfjord Fm.

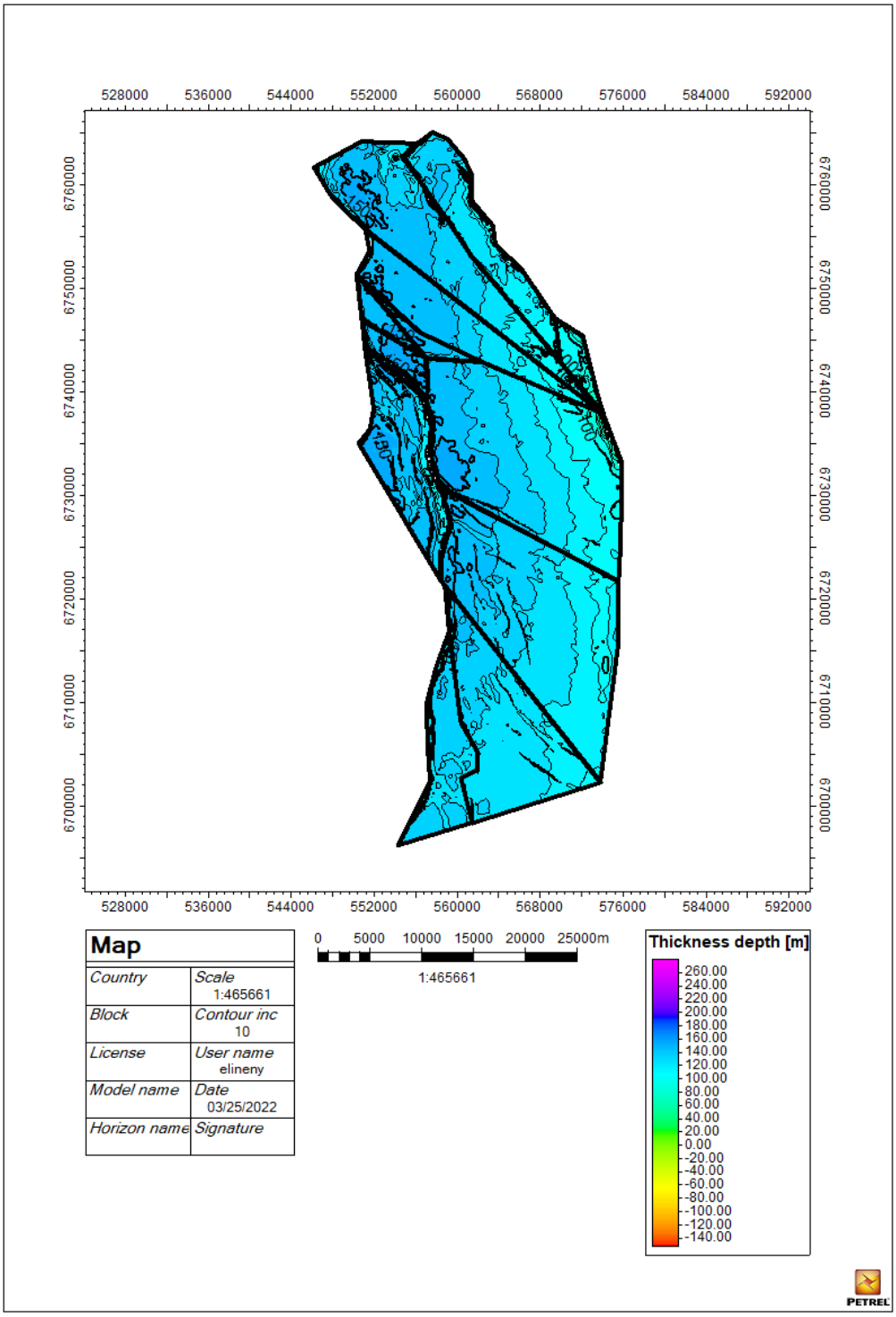

# J Scenario C - Thickness Depth Krossfjord Fm.

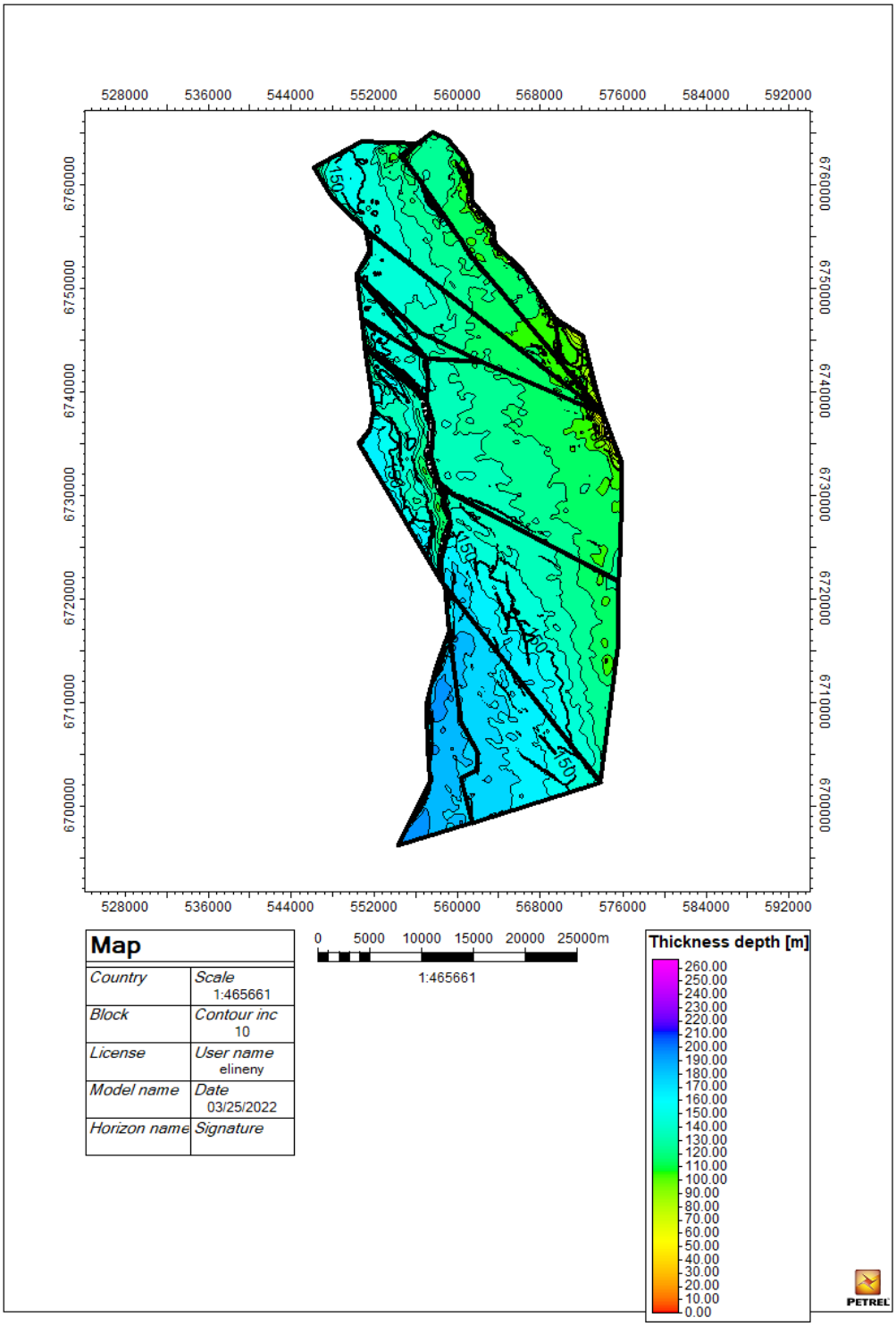

# K Scenario D - Thickness Depth Sognefjord Fm.

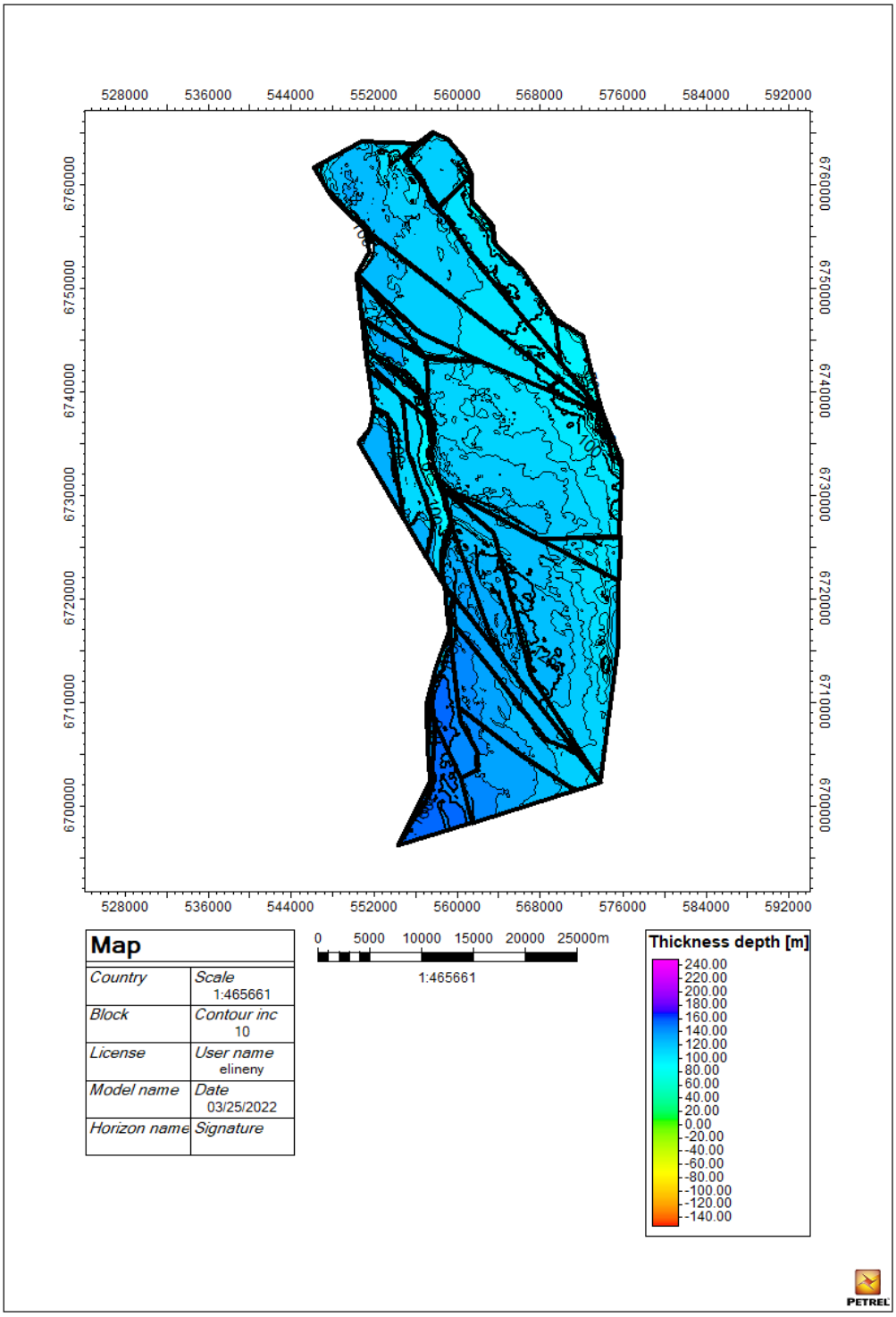

# L Scenario D - Thickness Depth Fensfjord Fm.

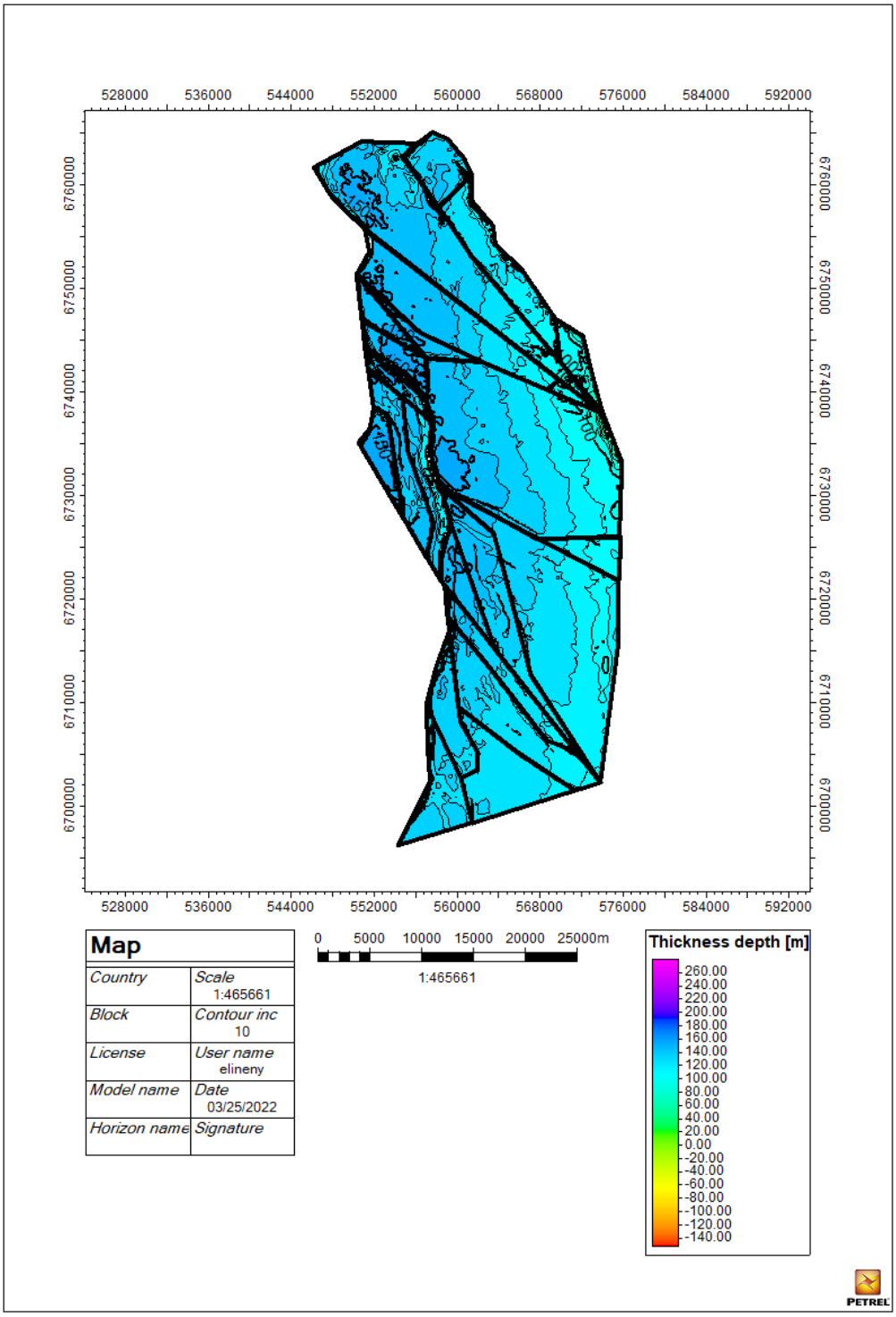

# M Scenario D - Thickness Depth Krossfjord Fm.

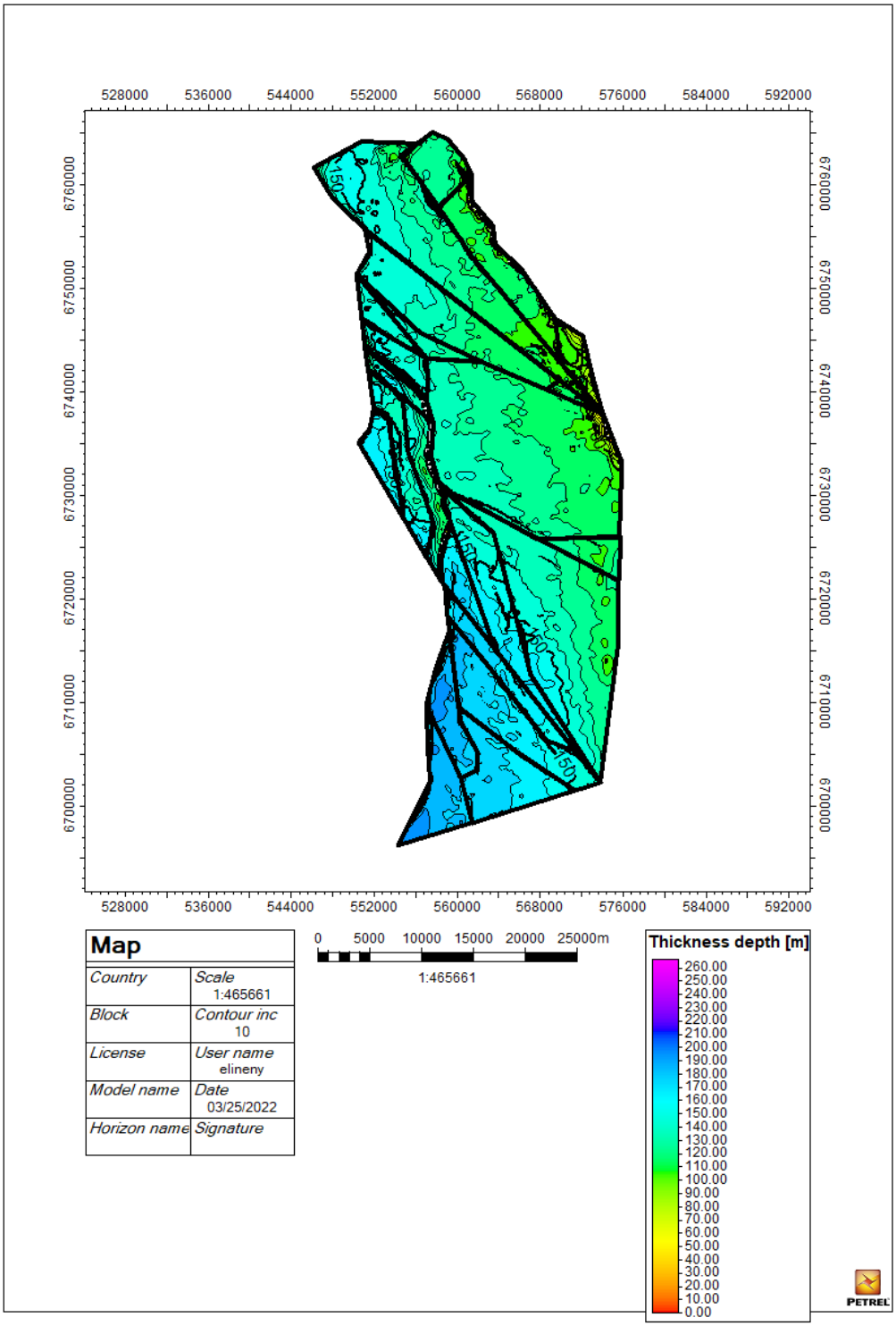

## N Python Code - Example for Inital Calculation

```
"""
Created on Mon Feb 14 11:19:22 2022
Modified May 2022

@author: Eline Nybr ten , in collaboration Tian Guo & Tobias Dyngeland
"""

import matplotlib.pyplot as plt
import math
import xlrd
import pandas as pd


# Reading from file with Petrel data for the compartments:

loc = (r'D:\compartments1.xlsx')

# opening workbook
wb = xlrd.open_workbook(loc)
sheet = wb.sheet_by_index(0)

#------------------------------------------------------------------------

# Defining Euler for pressure function
euler = math.exp(0.5772156649)

r = 0.5 ## regime, for pressure function

#SELECTING COMPARTMENT:
comp = 1

#Selecting injection year start:
injectionyear_start = 0;

print("Compartment name " + str(sheet.cell_value(comp+1,0)))

#Selecting injection period:
years= 50

totVol = 0;

#CALCULATIONS - PRESSURE FUNCTION :

# Data gathered from spreadsheet with Petrel values

# mean depth:
meand= int(sheet.cell_value(comp+1,4))
print("Mean depth: " + str(meand))

# initial pressure, found from initial hydrostatic pressure graph
pinit= float(sheet.cell_value(comp+1,9))*10
print("Pinit: " + str(pinit) + " bar")

# well pressure, pwell=0.9*pfrac where pfrac (fracture pressure) is from graph
pwell= 0.9*float(sheet.cell_value(comp+1,11))*10
print("Pwell: " + str(pwell) + " bar")

# area size:
area = float(sheet.cell_value(comp+1,1))/1000000 #converted to km^2
print("Area: " + str(area) + " km^2")

# Selecting A :
#Upper value: 7*10^-9
#a = - (0.28*area) + 44.6

#Medium value: compressibility: 3*10^-9
a = -(0.1224*area) + 44.69

# Value for tornado plot mean : 5*10^-9
#a = - (0.28*area) + 44.6 + (((-(0.1224*area) + 44.69 )-(- (0.28*area) + 44.6))/4)
```

```
    *2
72
73
74 #Lower value: compressibility: 5*10^-11
75 #a = - (0.012*area) + 44.9
76
77
78 # eliminating negative A's
79 if a < 2 :
80     a = 2
81
82
83
84 print("A: " + str(a))
85
86 # Setting injectivity index
87 Ic= 40
88 # Density
89 dens= 0.79
90 # Viscosity
91 visc= 0.07
92
93 pd = []
94 pres =[]
95 rate = []
96 mass =[]
97 xaxis = range(0,years+1)
98 # Total stored mass:
99 totalstorageMass = 0
100 # Total stored volume:
101 totalVol = 0 ;
102
103 #-------------------------------------------------------------------------
104
105 # COMRESSIBILITY CONSTRAINT ON INJECTION VOLUME :
106
107 #Selecting compressibility
108 #Cb = 0.000000007   #maximum case
109 Cb = 0.000000003     #Medium value
110 #Cb = 0.000000005     # Value for tornado plot
111 #Cb = 0.000000000005   #Minimal case
112
113 #Calculating total porevolume of compartment (m) :
114 Vb = int(sheet.cell_value(comp+1,1))*int(sheet.cell_value(comp+1,2))*0.295
115 print("Total pore volume:" + str(Vb))
116
117 #Selecting pressure change (Pfinal - Pinit) :
118 P = 5000000
119
120 #Calculating "available" pore volume :
121 V_max = (Cb * Vb * P)
122
123 print("Volume constraint from Cb: " + str(V_max/1000000000) + " km^3")
124
125 #-------------------------------------------------------------------------
126
127 decay = 0
128 min_i = 0
129 max_i = 0
130 peaknum= 1
131
132 for i in range(0,years+1) :
133
134
135         time = i
136         if i == 0 :
137             time = 0.25*euler
138
139         pd.append(r*math.log(4*time/euler))
140
141         # compressibility constraint
142         if  totVol > V_max/1000000000:
143             print("Compressibility constraint reached")
```

```
            pres.append(pres[i-1])
            totVol = V_max
            decay = 1

        elif (pinit + a*pd[i - min_i])>=pwell :
            decay = 1

        # pressure rise or decay?
        if decay == 0:
            pres.append(pinit + a*pd[i - min_i])
            max_i = i
            totVol += Ic*(pwell-pres[i])*365/1000000000
            print(totVol)
            rate.append(Ic*(pwell-pres[i]))
            mass.append(365*dens*rate[i]/1000000)
            totalstorageMass += 365*dens*rate[i]/1000000

        elif decay == 1:
            if totVol == V_max :
                print(totVol)
            #When pressure reaches initial pressure
            elif  (pinit + a*pd[max_i]-a*pd[i-max_i+peaknum-1])<=pinit:
                pres.append(pinit)

            else:
                pres.append((pinit + a*pd[max_i]-a*pd[i-max_i+peaknum]))
                totVol += 0
                totalstorageMass += 0
                print(totVol)


print("Total storage mass: " + str(totalstorageMass) + " million tonnes" )
print("Total storage volume: " + str(totVol) + " km^3" )


plt.plot(xaxis,pres, label = 'P_res')
plt.hlines(pwell,0,50,color = 'r', linestyle='-.', label='P_well')
plt.legend(loc='lower right')
plt.ylabel('Pressure')
plt.xlabel('Years')
plt.show()
```

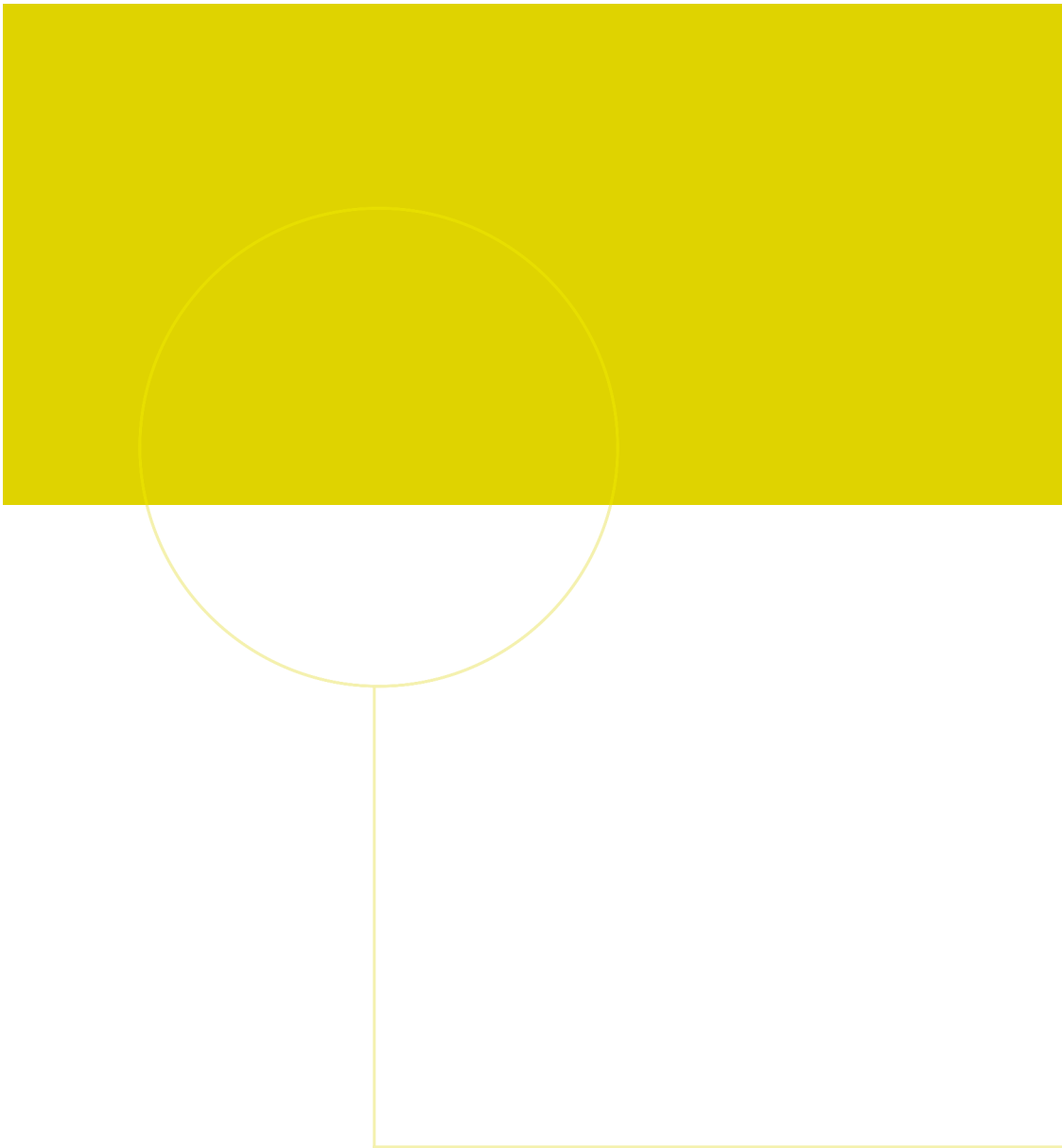

NTNU

Kunnskap for en bedre verden